

The Design and Validation of a Spacecraft Orbit and Attitude Simulation Environment in MATLAB/Simulink

By

Christopher Robert Joseph Robson

A thesis submitted in partial fulfillment of the requirements for the degree of

Master of Science

Department of Mechanical Engineering

University of Alberta

© Christopher Robert Joseph Robson, 2018

Abstract

CubeSats and Aerodynamic Attitude and Orbit Control Systems (AAOCS) orbit in Very Low Earth Orbit (VLEO) where the effect of aerodynamic force and torque is significant. In the mission analysis and design phases of CubeSat missions and satellite missions employing AAOCS, aerodynamic perturbations, along with others, must be modeled accurately. While several software packages from commercial, open-source, and academic sources exist to comprehensively model the orbital and attitude dynamics of satellites, barriers exist to their use by researchers, student groups, and small businesses. To overcome this barrier, OrbSim, an open-source software package, was developed in MATLAB/Simulink to model the orbital and attitude dynamics of spacecraft. This software package models aerodynamic forces and torques using the NRLMSISE-00 atmospheric model and assuming horizontal rotation of the atmosphere. Solar radiation pressure forces and torques are modeled using precise orbit ephemerides for the Sun, and assuming Earth's shadow is cylindrical. Both the solar radiation pressure and aerodynamic models are attitude and geometry dependent. OrbSim models gravitational forces from a non-uniform Earth using the Earth Gravitational Model 2008 (EGM2008), and gravity from the Sun and the Moon. Additionally, gravity-gradient torque and residual magnetic torque are modeled. The magnetic field is modeled using the International Geomagnetic Reference Field 12 (IGRF-12), and the World Geodetic System 84 (WGS84) is used for the reference ellipsoid. OrbSim was validated through comparison to AGI's System Tool Kit, an industry standard software package for simulating satellite orbital dynamics. The comparison was completed by simulating, in both STK and OrbSim, a satellite's orbital trajectory using different permutations of the perturbing forces. A case study predicting the lifetime of The Humanity Star was also completed, demonstrating the potential of OrbSim.

Preface

This thesis is an original work by Chris Robson. No part of this thesis has been previously published.

Dedication

This thesis is dedicated to my parents, Lorraine and Daniel Robson, my brothers, Matthew and David Robson, and my wife, Patricia Robson. Thank you for your love, your support and for patiently sitting through my rants about space.

This thesis is also dedicated to future graduates from the University of Alberta who have their eyes set on a career in outer space. Dream big, work hard, and aim for the stars. You just might hit the moon.

Acknowledgements

First and foremost, I'd like to acknowledge my supervisor Jason Carey and Dean of Engineering Fraser Forbes. Without your funding, your support, your continued guidance, and perhaps most importantly, your steadfast belief in my value, this thesis and my future would not be possible.

Jason, you've mentored me in both engineering and life, you've given your time and attention to an unfamiliar subject, and you very happily jumped onboard my crazy train when I first proposed this thesis topic to you (and you never looked back). You are an inspiration to me, and a standard I hold myself up to. Fraser, you've taken a keen interest in me, in AlbertaSat, and in building aerospace knowledge at the University of Alberta. You've taught me life lessons whenever you had time, and you've given me opportunities, both in education and travel, that I didn't have before. Thank you both—you've given my dreams foundations on which to stand.

Secondly, I'd like to acknowledge my co-supervisors Carlos Lange and Martin Barczyk. Carlos, you've always believed in me and advocated for me from the day I became Project Manager for Ex-Alta 1. Through that support and belief, I've had numerous opportunities, some of which directly fueled this research. For the time you gave to me in the past and for this thesis, thank you. Martin, you've inspired me to appreciate dynamics and controls since I took your MECE 420 controls course; you've always been available to answer questions, and you've shown a very keen interest in some of the crazy ideas I've had. Thank you for your time. I know it's a premium, and I appreciate every second of it.

Third, I would like to acknowledge ISSET and the Government of Alberta. Both supported me through the International Space Mission Mobility Scholarships and the Queen Elizabeth II scholarships respectively. Without the support of both organizations, I would have had a much harder time achieving my goals.

Fourth, I'd like to acknowledge my wife, Patricia Robson. You supported me emotionally when things got tough, you were always there to listen to me and you made my world much brighter simply with your presence. Also, you edited this thesis, which is a big job all on its own. I love you, sweetie.

Lastly, I'd like to acknowledge my parents, who brought me up and supported me financially throughout my university career. Thank you for your hard work, for your sacrifice, and for your support. I would not be who I am if it was not for you. I love you both dearly.

Table of Contents

1	Introduction	1
1.1	Motivation	1
1.2	Thesis Objective	2
1.3	Thesis Scope	2
1.4	Thesis Outline	3
2	Literature Review	4
2.1	CubeSats	4
2.2	Aerodynamic Attitude and Orbit Control Systems	7
2.2.1	Introduction to Aerodynamic Attitude and Orbit Control Systems	7
2.2.2	Passive Aerodynamic Attitude Control Systems	8
2.2.3	Active and Semi-Active Aerodynamic Control Systems	11
2.2.4	Aerodynamic Orbit Control Systems	13
2.2.5	Comparison of Simulations Developed for Previous Research	14
2.3	Existing Orbital Dynamics and Control Simulators	16
2.4	Research Proposal	20
2.4.1	Research Gap	20
2.4.2	Research Proposal and Justification	20
3	Background	21
3.1	Coordinate Systems, Transformations and Time	22
3.1.1	ECI and Keplerian Coordinate Systems and Transformations	22
3.1.2	ECEF and LVLH Coordinate Systems and Transformations	27
3.2	Orbit Propagation Methods	31
3.3	Satellite Dynamics	32
3.3.1	Rigid Body Mechanics	32

3.3.2	Satellite Inertial and Geometric Properties	35
3.4	Other Disturbance Forces and Torques	36
3.4.1	Earth Gravity Force and Gravity Gradient Torque	36
3.4.2	Aerodynamic Disturbance Force and Torque	38
3.4.3	Solar Pressure Force and Torque	43
3.4.4	Residual Magnetic Torque	46
3.4.5	Solar and Lunar Gravity Force.....	47
3.5	Summary	47
4	Simulation Design	48
4.1	Simulation Overview.....	48
4.2	Simulation Architecture	49
4.2.1	The GUI.....	50
4.2.2	InitConfig.mat / Config.mat	52
4.2.3	Simulink	57
4.2.4	SimData.mat.....	61
4.2.5	2D, 3D and Attitude Figures	61
4.3	Summary	65
5	Simulation Validation.....	65
5.1	Purpose	65
5.2	Methodology	65
5.3	Results & Discussion	67
5.4	Simple Case Study	73
5.5	Analysis and Conclusion.....	77
6	Conclusion and Future Work.....	77
6.1	Conclusion.....	77

6.2	Future Work	77
	References.....	79
	Appendix A: Symbols, Notation, Constants, Acronyms, and Definitions.....	84
A.1:	Notation.....	85
A.1.1:	Subscripts and Superscripts.....	85
A.1.2:	Vectors and Unit Vectors	85
A.2:	Constants	86
	Appendix B: Validation Graphs.....	87
B.1:	TLE #1.....	87
B.1.1:	Two Body Gravity.....	87
B.1.2:	Spherical Harmonic Gravity.....	92
B.1.3:	Spherical Harmonic Gravity & Solar gravity.....	97
B.1.4:	Spherical Harmonic Gravity & Lunar Gravity.....	102
B.1.5:	Spherical Harmonic Gravity & Aerodynamic Drag.....	107
B.1.6:	Spherical Harmonic Gravity & Solar Pressure.....	112
B.1.7:	Spherical Harmonic Gravity, Solar Gravity, Lunar Gravity, Aerodynamic Drag and Solar Pressure.....	117
B.2:	TLE #2.....	122
B.2.1:	Two Body Gravity.....	122
B.2.2:	Spherical Harmonic Gravity.....	127
B.2.3:	Spherical Harmonic Gravity & Solar gravity.....	132
B.2.4:	Spherical Harmonic Gravity & Lunar Gravity.....	137
B.2.5:	Spherical Harmonic Gravity & Aerodynamic Drag.....	142
B.2.6:	Spherical Harmonic Gravity & Solar Pressure.....	147

B.2.7: Spherical Harmonic Gravity, Solar Gravity, Lunar Gravity, Aerodynamic Drag and Solar Pressure.....	152
---	-----

List of Tables

Table 1: Dimensions for Various Sizes of CubeSats [44], [48].....	6
Table 2: Comparison of Simulation Characteristics used for Previous AACCS Research..	15
Table 3: Simulation Software Comparison.....	18
Table 4: Keplerian Elements.....	24
Table 5: Features of OrbSim Compared with Other Astrodynamics Softwares.....	49
Table 6: First Level of the InitConfig.mat Structure	54
Table 7: Breakdown of the Spacecraft Branch in the InitConfig.mat Structure.....	54
Table 8: Breakdown of the OrbSimIC Branch in the InitConfig.mat Structure	55
Table 9: Breakdown of the Constants Branch in the InitConfig.mat Structure	56
Table 10: Breakdown of the SimParam Branch in the InitConfig.mat Structure	57
Table 11: SimData.mat Signal File Structure	61
Table 12: Permutations of Orbital Perturbations for Simulation Testing.....	66
Table 13: Simulation Parameters	67
Table 14: TLE's used for Simulation [94].....	67
Table 15: RMS error for TLE#1 Simulation Comparison Between OrbSim and STK	69
Table 16: RMS error for TLE#2 Simulation Comparison Between OrbSim and STK	70
Table 17: Average RMS Error for TLE#1 and TLE#2.....	70
Table 18: Relative RMS Error for Run #7.....	71
Table 19: First TLE for The Humanity Star [94].....	75
Table 20: Re-entry Data for The Humanity Star	76
Table 21: Constants.....	86

Table of Figures

Figure 1: Trend in Nanosat Launches [45]	5
Figure 2: (a) 1U CubeSat (adapted from [47]), (b) 3U CubeSat Drawing (adapted from [44]).....	6

Figure 3: Schematic of PAMS showing its mass distribution design implemented using two cylindrical shells of different densities. (Adapted from [11]).....	9
Figure 4: Passive AACS Geometric Configuration Examples	10
Figure 5: Active AACS Examples	12
Figure 6: Semi-active AACS from Auret and Steyn (Adapted from [9]).....	13
Figure 7: Earth Centered Inertial Coordinate System and Keplerian Elements	23
Figure 8: ECEF, ECI and LVLH Coordinate Systems	28
Figure 9: LVLH Coordinate System and Body Fixed Frame	30
Figure 10: Free body diagram showing the vector sum of the forces and torques acting on a 3U CubeSat in orbit.....	33
Figure 11: Geometric Properties of Simulated Satellite	36
Figure 12: Accommodation/Absorption [42], [68].....	40
Figure 13: Specular Reflection [42], [68].....	41
Figure 14: Diffuse Reflection [42], [68].....	42
Figure 15: Satellite in Eclipse (photocredit: NASA[89])	46
Figure 16: OrbSim High Level Architecture	50
Figure 17: OrbSim GUI (a) Top Portion (b) Bottom Portion	51
Figure 18: Organization of Structure Variable InitConfig.mat.....	53
Figure 19: Simulink Model.....	58
Figure 20: The Spacecraft Block	59
Figure 21: The Environmental Disturbances Block.....	60
Figure 22: Example 3D Output.....	62
Figure 23: Attitude of the Spacecraft's B-frame Relative to the O-frame.....	63
Figure 24: Example 2D Output.....	64
Figure 25: TLE#2 Inertial Position Comparison	69
Figure 26: Lifetime Plot of The Humanity Star Using Actual Tracking Data, and Predictions From OrbSim and STK.....	76
Figure 27: Superscript and subscript notation standard.....	85
Figure 28: Inertial Position Comparison of the Satellite from TLE#1 with Two Body Gravity	87

Figure 29: Inertial Velocity Comparison of the Satellite from TLE#1 with Two Body Gravity	88
Figure 30: Latitude Comparison of the Satellite from TLE#1 with Two Body Gravity ..	89
Figure 31: Longitude Comparison of the Satellite from TLE#1 with Two Body Gravity	90
Figure 32: Altitude Comparison of the Satellite from TLE#1 with Two Body Gravity...	91
Figure 33: Inertial Position Comparison of the Satellite from TLE#1 with Spherical Harmonic Gravity	92
Figure 34: Inertial Velocity Comparison of the Satellite from TLE#1 with Spherical Harmonic Gravity	93
Figure 35: Latitude Comparison of the Satellite from TLE#1 with Spherical Harmonic Gravity	94
Figure 36: Longitude Comparison of the Satellite from TLE#1 with Spherical Harmonic Gravity	95
Figure 37: Altitude Comparison of the Satellite from TLE#1 with Spherical Harmonic Gravity	96
Figure 38: Inertial Position Comparison of the Satellite from TLE#1 with Spherical Harmonic Gravity and Solar Gravity	97
Figure 39: Inertial Velocity Comparison of the Satellite from TLE#1 with Spherical Harmonic Gravity and Solar Gravity	98
Figure 40: Latitude Comparison of the Satellite from TLE#1 with Spherical Harmonic Gravity and Solar Gravity	99
Figure 41: Longitude Comparison of the Satellite from TLE#1 with Spherical Harmonic Gravity and Solar Gravity	100
Figure 42: Altitude Comparison of the Satellite from TLE#1 with Spherical Harmonic Gravity and Solar Gravity	101
Figure 43: Inertial Position Comparison of the Satellite from TLE#1 with Spherical Harmonic Gravity and Lunar Gravity	102
Figure 44: Inertial Velocity Comparison of the Satellite from TLE#1 with Spherical Harmonic Gravity and Lunar Gravity	103
Figure 45: Inertial Latitude Comparison of the Satellite from TLE#1 with Spherical Harmonic Gravity and Lunar Gravity	104

Figure 46: Longitude Comparison of the Satellite from TLE#1 with Spherical Harmonic Gravity and Lunar Gravity.....	105
Figure 47: Altitude Comparison of the Satellite from TLE#1 with Spherical Harmonic Gravity and Lunar Gravity.....	106
Figure 48: Inertial Position Comparison of the Satellite from TLE#1 with Spherical Harmonic Gravity and Aerodynamic Drag.....	107
Figure 49: Inertial Velocity Comparison of the Satellite from TLE#1 with Spherical Harmonic Gravity and Aerodynamic Drag.....	108
Figure 50: Latitude Comparison of the Satellite from TLE#1 with Spherical Harmonic Gravity and Aerodynamic Drag.....	109
Figure 51: Longitude Comparison of the Satellite from TLE#1 with Spherical Harmonic Gravity and Aerodynamic Drag.....	110
Figure 52: Altitude Comparison of the Satellite from TLE#1 with Spherical Harmonic Gravity and Aerodynamic Drag.....	111
Figure 53: Inertial Position Comparison of the Satellite from TLE#1 with Spherical Harmonic Gravity and Solar Radiation Pressure.....	112
Figure 54: Inertial Velocity Comparison of the Satellite from TLE#1 with Spherical Harmonic Gravity and Solar Radiation Pressure.....	113
Figure 55: Latitude Comparison of the Satellite from TLE#1 with Spherical Harmonic Gravity and Solar Radiation Pressure.....	114
Figure 56: Longitude Comparison of the Satellite from TLE#1 with Spherical Harmonic Gravity and Solar Radiation Pressure.....	115
Figure 57: Altitude Comparison of the Satellite from TLE#1 with Spherical Harmonic Gravity and Solar Radiation Pressure.....	116
Figure 58: Inertial Position Comparison of the Satellite from TLE#1 with Spherical Harmonic Gravity, Solar Gravity, Lunar Gravity, Aerodynamic Force and Solar Radiation Pressure.....	117
Figure 59: Inertial Velocity Comparison of the Satellite from TLE#1 with Spherical Harmonic Gravity, Solar Gravity, Lunar Gravity, Aerodynamic Force and Solar Radiation Pressure.....	118

Figure 60: Latitude Comparison of the Satellite from TLE#1 with Spherical Harmonic Gravity, Solar Gravity, Lunar Gravity, Aerodynamic Force and Solar Radiation Pressure..... 119

Figure 61: Longitude Comparison of the Satellite from TLE#1 with Spherical Harmonic Gravity, Solar Gravity, Lunar Gravity, Aerodynamic Force and Solar Radiation Pressure..... 120

Figure 62: Altitude Comparison of the Satellite from TLE#2 with Spherical Harmonic Gravity, Solar Gravity, Lunar Gravity, Aerodynamic Force and Solar Radiation Pressure..... 121

Figure 63: Inertial Position Comparison of the Satellite from TLE#2 with Two Body Gravity 122

Figure 64: Inertial Velocity Comparison of the Satellite from TLE#2 with Two Body Gravity 123

Figure 65: Latitude Comparison of the Satellite from TLE#2 with Two Body Gravity 124

Figure 66: Longitude Comparison of the Satellite from TLE#2 with Two Body Gravity 125

Figure 67: Altitude Comparison of the Satellite from TLE#2 with Two Body Gravity. 126

Figure 68: Inertial Position Comparison of the Satellite from TLE#2 with Spherical Harmonic Gravity 127

Figure 69: Inertial Velocity Comparison of the Satellite from TLE#2 with Spherical Harmonic Gravity 128

Figure 70: Latitude Comparison of the Satellite from TLE#2 with Spherical Harmonic Gravity 129

Figure 71: Longitude Comparison of the Satellite from TLE#2 with Spherical Harmonic Gravity 130

Figure 72: Altitude Comparison of the Satellite from TLE#2 with Spherical Harmonic Gravity 131

Figure 73: Inertial Position Comparison of the Satellite from TLE#2 with Spherical Harmonic Gravity and Solar Gravity 132

Figure 74: Inertial Velocity Comparison of the Satellite from TLE#2 with Spherical Harmonic Gravity and Solar Gravity 133

Figure 75: Latitude Comparison of the Satellite from TLE#2 with Spherical Harmonic Gravity and Solar Gravity 134

Figure 76: Longitude Comparison of the Satellite from TLE#2 with Spherical Harmonic Gravity and Solar Gravity	135
Figure 77: Altitude Comparison of the Satellite from TLE#2 with Spherical Harmonic Gravity and Solar Gravity	136
Figure 78: Inertial Position Comparison of the Satellite from TLE#2 with Spherical Harmonic Gravity and Lunar Gravity	137
Figure 79: Inertial Velocity Comparison of the Satellite from TLE#2 with Spherical Harmonic Gravity and Lunar Gravity	138
Figure 80: Latitude Comparison of the Satellite from TLE#2 with Spherical Harmonic Gravity and Lunar Gravity	139
Figure 81: Longitude Comparison of the Satellite from TLE#2 with Spherical Harmonic Gravity and Lunar Gravity	140
Figure 82: Altitude Comparison of the Satellite from TLE#2 with Spherical Harmonic Gravity and Lunar Gravity	141
Figure 83: Inertial Position Comparison of the Satellite from TLE#2 with Spherical Harmonic Gravity and Aerodynamic Drag	142
Figure 84: Inertial Velocity Comparison of the Satellite from TLE#2 with Spherical Harmonic Gravity and Aerodynamic Drag	143
Figure 85: Latitude Comparison of the Satellite from TLE#2 with Spherical Harmonic Gravity and Aerodynamic Drag	144
Figure 86: Longitude Comparison of the Satellite from TLE#2 with Spherical Harmonic Gravity and Aerodynamic Drag	145
Figure 87: Altitude Comparison of the Satellite from TLE#2 with Spherical Harmonic Gravity and Aerodynamic Drag	146
Figure 88: Inertial Position Comparison of the Satellite from TLE#2 with Spherical Harmonic Gravity and Solar Radiation Pressure	147
Figure 89: Inertial Velocity Comparison of the Satellite from TLE#2 with Spherical Harmonic Gravity and Solar Radiation Pressure	148
Figure 90: Latitude Comparison of the Satellite from TLE#2 with Spherical Harmonic Gravity and Solar Radiation Pressure	149

Figure 91: Longitude Comparison of the Satellite from TLE#2 with Spherical Harmonic Gravity and Solar Radiation Pressure 150

Figure 92: Altitude Comparison of the Satellite from TLE#2 with Spherical Harmonic Gravity and Solar Radiation Pressure 151

Figure 93: Inertial Position Comparison of the Satellite from TLE#2 with Spherical Harmonic Gravity, Solar Gravity, Lunar Gravity, Aerodynamic Force and Solar Radiation Pressure 152

Figure 94: Inertial Velocity Comparison of the Satellite from TLE#2 with Spherical Harmonic Gravity, Solar Gravity, Lunar Gravity, Aerodynamic Force and Solar Radiation Pressure 153

Figure 95: Latitude Comparison of the Satellite from TLE#2 with Spherical Harmonic Gravity, Solar Gravity, Lunar Gravity, Aerodynamic Force and Solar Radiation Pressure..... 154

Figure 96: Longitude Comparison of the Satellite from TLE#2 with Spherical Harmonic Gravity, Solar Gravity, Lunar Gravity, Aerodynamic Force and Solar Radiation Pressure..... 155

Figure 97: Altitude Comparison of the Satellite from TLE#2 with Spherical Harmonic Gravity, Solar Gravity, Lunar Gravity, Aerodynamic Force and Solar Radiation Pressure..... 156

List of Greek Symbols

Symbol	Units	Description
δ	deg	Latitude
ϕ^E	$\frac{\text{J}}{\text{kg}}$	Earth gravitational potential function in the E-frame.
J_B	kgm^2	Inertia tensor in the body frame.
J_M^B	kgm^2	Mass moment of inertia in the body frame.
J_P^B	kgm^2	Product of inertia in the body frame.
I_S		Solar irradiance.
λ	deg	Longitude
ρ	$\frac{\text{kg}}{\text{m}^3}$	Atmospheric density
σ_{Abs}	Unitless	Absorption coefficient
σ_{Spec}	Unitless	Specular reflection coefficient
σ_{Diff}	Unitless	Diffuse reflection coefficient
σ_A	Unitless	Accommodation coefficient.
$\vec{\tau}_{cm}^B$	Nm	The torque vector acting in the body frame at the COM.
$\vec{\tau}^B$	Nm	Torque vector acting in the body frame.
v	deg	True anomaly.
\vec{v}	$\frac{\text{m}}{\text{s}}$	Velocity vector.
\vec{v}_b^B	$\frac{\text{m}}{\text{s}}$	Velocity vector of diffusely reflected particles normal to the surface.
\vec{v}_{cm}^B	$\frac{\text{m}}{\text{s}}$	Velocity vector acting in the body fixed frame at the COM.
$\dot{\vec{v}}_{cm}^B$	$\frac{\text{m}}{\text{s}^2}$	Velocity vector acting in the body fixed frame at the COM
\vec{v}_{IB}^I	$\frac{\text{m}}{\text{s}}$	Velocity of the B-frame with respect to the I-frame in I-frame coordinates.
\vec{v}_f	$\frac{\text{m}}{\text{s}}$	Free stream fluid velocity vector.
\vec{v}_f^B	$\frac{\text{m}}{\text{s}}$	Free stream fluid velocity vector in the B-frame.
ω	deg	Argument of perigee.
ω_E	$\frac{\text{rad}}{\text{s}}$	Angular rotation rate of the Earth.
$\vec{\omega}_{AB}^B$	$\frac{\text{rad}}{\text{s}}$	Angular velocity in the body fixed frame.
$\dot{\vec{\omega}}_{AB}^B$	$\frac{\text{rad}}{\text{s}^2}$	Angular acceleration vector in the body fixed frame.
Ω	deg	RAAN

List of Non-Greek Symbols

Symbol	Units	Description
a	km	Semi-major axis.
\vec{a}_g	$\frac{\text{m}}{\text{s}^2}$	Gravitational acceleration vector
\vec{A}^B	Am ²	The vector representing the residual magnetic dipole moment of the satellite in the B-frame.
A_n	m ²	Surface area normal to free stream velocity.
\vec{B}^I	nT	The vector representing magnetic field strength of Earth's magnetic field in the I-frame.
C_D	Unitless	Drag coefficient.
\vec{C}_{PA}^B	m	Vector representing the center of aerodynamic pressure in the B-frame.
\vec{c}_{SP}^B	m	The vector representing the center of solar pressure in the B-frame.
$C_{n,m}$	N/A	Tesseral harmonic constant.
e	Unitless	Eccentricity.
\vec{e}	Unitless	Eccentricity vector.
\vec{f}_{Acc}^B	N	Force vector representing the contribution to aerodynamic force from accommodation acting in the B-frame.
\vec{f}_{Abs}^B	N	Force vector representing the contribution to solar pressure force due to absorption acting in the B-frame.
\vec{f}_{Diff}^B	N	Force vector representing the contribution to aerodynamic force from diffusion acting in the B-frame.
\vec{f}_{SR}^B	N	Force vector representing the contribution to the solar pressure force due to specular reflection acting in the B-frame.
\vec{f}_{DR}^B	N	Force vector representing the contribution to the solar pressure force due to diffuse reflection acting in the B-frame.
\vec{f}_{SP}^B	N	Force vector representing the solar pressure force acting in the B-frame.
\vec{f}_{EG}^B	N	Force vector representing the terrestrial gravity force acting in the B-frame.
\vec{f}_{SG}^B	N	Force vector representing the solar gravity force acting in the B-frame.
\vec{f}_{Spec}^B	N	Force vector representing the contribution to aerodynamic force from specular reflection acting in the B-frame.
\vec{f}_{LG}^B	N	Force vector representing the lunar gravity force acting in the B-frame.
\vec{f}_{cm}^B	N	Force vector acting in the body frame at the COM
\vec{f}_P	N	Perturbation force vector acting on a satellite.
\vec{f}_A^B	N	Aerodynamic force vector acting in the B-frame.
\vec{F}_g	N	Gravity force vector
\vec{g}_E^E	$\frac{\text{m}}{\text{s}^2}$	Terrestrial gravitational acceleration vector in the E-frame.
\vec{h}	$\frac{\text{m}^2}{\text{s}}$	Orbital momentum vector.
i	deg	Inclination.
JD	days	Julian date.
J_n	N/A	Zonal harmonic constant.
m_s	kg	Satellite mass
\vec{n}	N/A	Normal vector.
P_n	N/A	Legendre function.
$P_{n,m}$	N/A	Associated Legendre function.
P_{SP}	$\frac{\text{N}}{\text{m}^2}$	Solar pressure.

Symbol	Units	Description
\vec{r}	m	Position vector
$\ddot{\vec{r}}$	$\frac{\text{m}}{\text{s}^2}$	Acceleration vector
\vec{r}_{IB}^I	m	Position vector of the B-frame with respect to the I-frame expressed in the I-frame coordinate system.
\vec{r}_{IS}^I	m	Position vector of the center of the sun to the origin of the I-frame expressed in the I-frame coordinate system.
\hat{r}_{BS}^B	m	Unit vector pointing from the B-frame to the center of the sun in B-frame coordinates.
\vec{r}_{BL}^I	m	Position vector of the center of the satellite to the center of the Moon in the I-frame coordinate system.
\vec{r}_{IL}^I	m	Position vector of the center of the Earth to the center of the Moon in the I-frame coordinate system.
\vec{r}_{EB}^E	m	Position vector of the center of the Earth to the satellites COM in the E-frame.
R_{IB}	N/A	The rotation matrix representing the orientation of the B-frame with respect to the I-frame.
R_{EI}	N/A	The rotation matrix representing the orientation of the I-frame with respect to the E-frame.
R_{IE}	N/A	The rotation matrix representing the orientation of the E-frame with respect to the I-frame.
R_{OB}	N/A	The rotation matrix representing the orientation of the B-frame with respect to the O-frame.
S_{WA}	m ²	Wetted surface area.
$S_{n,m}$	N/A	Tesseral harmonic constant.
\vec{T}_A^B	Nm	The aerodynamic torque vector acting on the satellite in the body fixed frame as a result of aerodynamic forces.
\vec{T}_{GG}^B	Nm	The gravity gradient torque vector acting on the satellite in the body fixed frame as a result of Earth's gravity.
\vec{T}_M^B	Nm	The residual magnetic torque vector acting on the satellite in the body fixed frame as a result of Earth's magnetic field.
\vec{T}_{SP}^B	Nm	The solar pressure torque vector acting on the satellite in the body fixed frame.
V	$\frac{\text{m}}{\text{s}}$	Satellite velocity for a circular orbit.

List of Abbreviations

Abbreviation	Definition
AACS	Aerodynamic Orbit Control System
AAOCS	Aerodynamic Attitude and Orbit Control System
ADCS	Attitude Determination and Control System
AOCS	Aerodynamic Orbit Control System
BFF	Body Fixed Frame
CAD	Computer Aided Design
COG	Center Of Gravity
COGEO	Center Of Geometry
COM	Center Of Mass
COP	Center Of Pressure
COTS	Commercial Off The Shelf
DSMC	Direct Simulation Monte Carlo
ECEF	Earth Centered Earth Fixed
ECI	Earth Centered Inertial
EGM2008	Earth Gravitational Model 2008
EO	Earth Observation
EOP	Earth Orientation Parameters
FBD	Free Body Diagram
GNC	Guidance Navigation and Control
GMST	Greenwich Mean Sidereal Time
GNC	Guidance Navigation and Control
GOCE	Gravity Field and Steady State Ocean Circulation Explorer
GUI	Graphical User Interface
ICRS	International Celestial Reference System
IGRF	International Geomagnetic Reference Field
ITRF	Inernational Terrestrial Reference Frame
ISS	International Space Station
LEO	Low Earth Orbit
LLA	Latitude, Longitude and Altitude
LVLH	Local Vertical Local Horizontal
PAMS	Passive Aerodynamically Stabilized Magnetically Damped Satellite
RAAN	Right Ascension of the Ascending Node
RMS	Root Mean Square
SCT	Spacecraft Control Toolbox
SGP4	Simplified General Perturbations 4
SLATS	Super Low Altitude Test Satellite
SOAR	Satellite for Orbital Aerodynamics Research
SRP	Solar Radiation Pressure
STK	Systems Tool Kit
TLE	Two Line Elements
UTC	Coordinated Universal Time
VLEO	Very Low Earth Orbit

1 Introduction

1.1 Motivation

In 1999, California Polytechnic and Stanford University introduced the Cube Satellite (CubeSat) specification, a document which describes a small ($\sim 10 \text{ cm}^3$), modular and standardized spacecraft called a CubeSat [1]. CubeSats are inexpensive ($< \$250,000$), flexible, and quick to build [2]–[5]. However, the nature of the CubeSat also contains its primary disadvantage: size. The small size of a CubeSat limits payload performance because it limits mission scope, power generation capability, and communication capability [2]. Improving the performance of CubeSat payloads by offsetting these disadvantages would offer greater return on CubeSat missions, with benefits to public, private, and academic institutions alike.

One possible method of improving mission performance would be to lower the feasible orbital altitude of CubeSats [6], [7]. Orbiting closer to Earth would result in better optical resolution and radiometric performance for Earth observation (EO) satellites, higher signal quality for communications, lower mass and power requirements for radar payloads, improved accuracy of geospatial positioning for EO payloads, and lower launch costs [6]. Most satellites orbit above about 450 km as lower orbits result in shorter mission life due to aerodynamic drag [6]. Additionally, aerodynamic disturbance torques can exceed the actuator limits of the CubeSat attitude determination and control systems (ADCS) [6]. To orbit closer to Earth, a control system which employs atmospheric effects (torque and drag), such as an aerodynamic attitude and orbit control system (AAOCS), may be used for attitude control and station keeping[7].

The research proposed is the creation of a dynamics simulation capable of modelling environmental disturbances acting on orbiting satellites with focus on the modelling of spacecraft aerodynamics. This simulation package will serve as a foundation for future development of AAOCS for satellites operating in very low earth orbit (VLEO, $< 450 \text{ km}$, [6]), a foundation for analyzing previous research concerning these systems, and as a useful design tool for CubeSat missions typically orbiting lower than traditional satellites. Previous research shows that solutions to aerodynamic attitude control, aerodynamic orbit control, or both together have been investigated. Passive aerodynamic attitude control systems (AACS) have been both investigated and implemented, while only a few active control solutions have been analyzed for feasibility or received some level of design [8]–[14]. Aerodynamic orbit control systems (AOCS) include those

that use aerodynamic forces for orbit control; these systems have been studied extensively and demonstrated in orbit [15]–[22], and those that directly oppose the aerodynamic force to maintain orbit in VLEO [7], [23]–[25]. Additionally, while there exist commercial, open source, and academic simulation software packages for orbital dynamics [26]–[43], these software packages either lack capability, are too expensive, or are no longer supported. As a result, there are barriers to further development of AAOCS.

1.2 Thesis Objective

For this thesis, a simulation environment for satellite orbit and attitude propagation will be created in MATLAB/Simulink. The simulation environment will model gravity from a non-spherical Earth, spacecraft aerodynamics, solar radiation pressure, third bodies, and spacecraft residual magnetic moment. The orbit and attitude propagation capability of the simulation environment will then be validated against an industry-standard software. Finally, a case study will demonstrate the simulation’s performance in comparison to the orbital trajectory and re-entry of the Humanity Star.

1.3 Thesis Scope

The scope of this thesis includes the development and validation of a simulation environment in MATLAB/Simulink of the six degree of freedom dynamics of a spacecraft’s orbit and attitude. This simulation will model the gravitational effects of a non-spherical Earth, an atmospheric density model which includes diurnal, tidal, locational, geomagnetic, and solar induced density variations, the modelling of upper atmospheric winds, the International Geomagnetic Reference Field (IGRF) model, and ephemeris data for astronomical bodies. Disturbance forces and torques considered will include non-uniform Earth gravity, aerodynamic torque and drag, residual magnetic moment, gravity gradient torque, solar radiation pressure torque and drag, solar gravity and lunar gravity.

The accuracy of the new simulation environment in propagating satellite attitude and orbital dynamics affected by the environmental disturbances and environmental models will be validated against industry standard software. The primary outcome of this thesis is a validated satellite attitude and orbital dynamics simulation environment in MATLAB/Simulink that effectively models satellite dynamics in the presence of disturbance torques. Additionally, a case study will be performed that demonstrates the ability of simulation environment to correctly

predict the orbital trajectory and atmospheric re-entry of the Humanity Star. Following this thesis, it is intended that this simulation be released as an open source software package to help student groups, researchers, and small businesses. This simulation package will also be used for the future development of an AAOCS, the examination of previously researched AAOCS, and as a design tool for future satellite missions.

1.4 Thesis Outline

The remainder of this thesis is structured as follows. The second chapter provides a review of currently available astrodynamics simulators and previous research conducted on AAOCS. Additionally, a research gap is identified. The resulting research project is proposed and a justification is provided. In the third chapter, background information is presented that provides necessary context and foundational information for theory. This includes the satellite dynamics model used to propagate the orbit and attitude of the simulated satellite. The fourth chapter describes the design and architecture of the Simulink simulation and MATLAB graphical user interface (GUI). The fifth chapter contains the results of experimental validation against an industry standard software and in an experimental case study. Chapter six concludes the thesis by summarising what was completed, making recommendations for simulation updates and describing future work.

2 Literature Review

This chapter begins with a short introduction to CubeSats, their history, and their advantages and disadvantages. This chapter continues by looking at previous research completed on a possible solution to the disadvantages of CubeSats and AAOCS. AAOCS are sub-divided into passive and active AACS, AACS which counteract aerodynamic forces and AACS that take advantage of them. Then, different astrodynamics software packages from commercial, open source, and academic sources are compared. Finally, a research gap is identified, and a research objective is proposed.

2.1 CubeSats

In 1999, Dr. Jordi Puig-Suari of Cal Poly and Dr. Bob Twiggs of Stanford created the CubeSat specification[2], which describes a small spacecraft with a standardized form, interface, and design [44]. Since its inception, 810 CubeSats have launched, with the number of launches rising every year (see Figure 1 [45]). Originally designed for technology development and education for academic institutions, CubeSats are now being used by businesses, civil space programs, and the military [3]. Research, development, and technology miniaturization has allowed for more potential uses of CubeSats to be discovered. Today's CubeSats are used in missions such as Earth Observation, astronomical research, or asteroid mining. The low hardware cost (< \$250,000 [3].), short design life (1 -2 years [4]), and mission potential of CubeSats have allowed space to be far more accessible than it ever was before, as illustrated by the significant growth in CubeSats launched in the past five years (Figure 1).

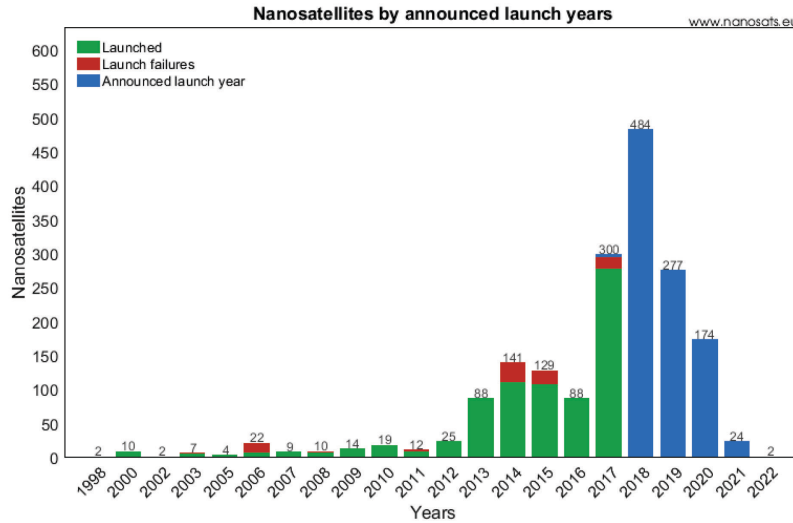
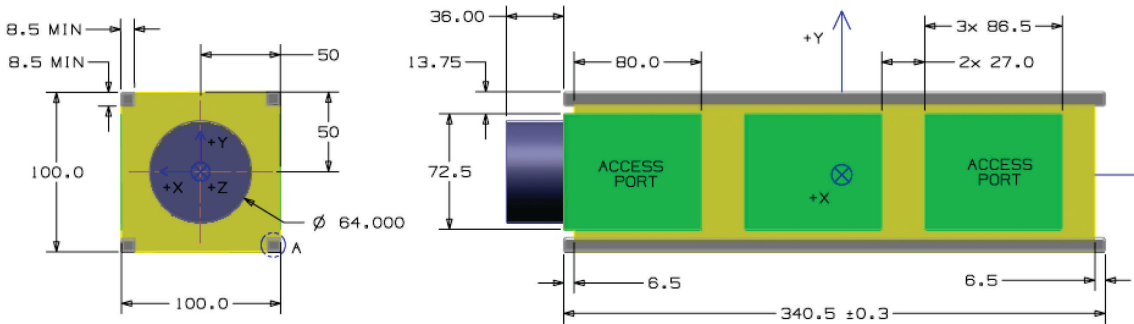
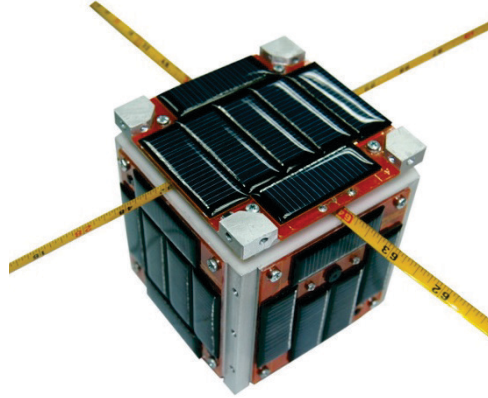


Figure 1: Trend in Nanosat Launches [45]

CubeSats are small, modular, and standardized nanosatellites (1 – 10 kg [46]), with the smallest module, one unit or 1U (Figure 2 (a)), measuring 10 x 10 x 10 cm³ and 1.33 kg [44]. 1U modules can be stacked together to create larger CubeSats (2U, 3U and 6U CubeSats). Note that longitudinal spacing between CubeSat units is standardized. Dimensions and masses for typical CubeSat configurations are shown in Table 1 and with a 3U schematic shown in Figure 2 (b). No limit exists to the number of units a CubeSat can contain. As a result, CubeSats can be stacked to any size; however, the majority of CubeSats have been 6U and below [45]. In any case, the standardization of CubeSats has allowed commercial off-the-shelf (COTS) suppliers to provide CubeSat subsystems that can be used on any size or configuration of CubeSat.



(c)

Figure 2: (a) 1U CubeSat (adapted from [47]), (b) 3U CubeSat Drawing (adapted from [44])

Table 1: Dimensions for Various Sizes of CubeSats [44], [48]

CubeSat Size	Width (mm)	Height (mm)	Length (mm)	Mass (kg)
1U	100 ± 0.1	100 ± 0.1	113.5 ± 0.1	1.33
2U	100 ± 0.1	100 ± 0.1	227 ± 0.2	2.66
3U	100 ± 0.1	100 ± 0.1	340.5 ± 0.3	4.0
6U	100 ± 0.1	226.3 ± 0.1	366 ± 0.1	12.0

The cost, short design life, and flexibility of CubeSats have made space more accessible, and these factors have affected the space industry in a significant way. However, the nature of the CubeSat also holds its primary disadvantage: its size. The size of a CubeSat limits the type and size of the possible payloads which can be flown. For example, a 3U CubeSat limits the possible

aperture size of optical EO payloads to 100 mm which, due to diffraction limitations, sets a hard limit on resolution (~ 9.8 m at 800 km [2]). The limited surface area available for solar cells results in low power generation, ~ 5 W for a 3U assuming no deployable solar panels, which typically prevents active EO payloads (which tend to require a lot of power) from being flown, limiting mission potential. Power limitations also limit communications by limiting the data rate between the spacecraft and ground station while the size limits the type of antennas which can be flown and their bandwidth. Lastly, the size of CubeSats limits momentum-based attitude control methods, which tend to require a far larger mass/volume fraction in order to be effective. This restriction reduces the already small availability for payloads [49]. However, the potential of CubeSats is being expanded every day with technological advancement and miniaturization, allowing for increased mission return and potential mission applications (exemplified by JPL's recent CubeSat design for Mars [50]).

2.2 Aerodynamic Attitude and Orbit Control Systems

Characterizing the effects of aerodynamic disturbances on spacecraft in low earth orbit (LEO) has been a focus of research since the early days of space flight [51]–[53]. Aerodynamic drag causes satellites to de-orbit, setting a limit on mission life, while aerodynamic torque acts against a spacecraft's attitude control system [6], [7]. To avoid mission lives shorter than five years, spacecraft typically fly above 450 km, where aerodynamic disturbances become less significant compared to other disturbances [6], [7]. However, with the advent of CubeSats, more missions are at altitudes where aerodynamic disturbances become significant, and finding solutions to negate or utilize these aerodynamic forces has become important. Additionally, there are many advantages for both CubeSats and other spacecraft to orbit below 450 km in VLEO [6], especially for Earth observation missions [6], [7], such as higher image resolution, lower launch cost, higher radiometric performance, and stronger communication links. One solution to this problem is to use aerodynamic torques to control the attitude of the spacecraft, and to counteract the effect of aerodynamic forces with propulsion and drag minimization. These AAOCS have been the subject of some research and a few in-orbit demonstrations, and they show potential to improve CubeSat performance at altitudes where aerodynamic disturbances are significant.

2.2.1 Introduction to Aerodynamic Attitude and Orbit Control Systems

Spacecraft in VLEO experience non-negligible aerodynamic disturbance forces and torques; these forces respectively degrade mission lifetime and disturb spacecraft attitude. AAOCS

are a solution to either counteracting or employing aerodynamic disturbances in VLEO and can be further sub-divided into AACS or AOCS. AACS employ either geometry, external control surfaces, or mass distribution to place the center of pressure behind the center of mass relative to the incoming free stream velocity, resulting in an aerodynamic torque stabilizing the spacecraft's attitude. A passive AACS stabilizes a spacecraft about one or more axes without any control input, much like the feathers of an arrow. An active AACS is operated by a control loop to stabilize the spacecraft about one or more axes, much like the elevators, ailerons, or rudder of an airplane. A semi-active system combines both passive and active AACS.

AACS have been explored at two separate periods in the history of spaceflight. Gargaz [10] sets the first time period between 1966 and 1972 and the second between 1995 to 2004. In truth, the second period which started in 1995 has not ended, as interest in AACS has continued to the present day, especially for CubeSats. AOCS can also be sub-divided between those which include a propulsion system to counteract aerodynamic forces and those that make use of the aerodynamic force to control orbital position. This section reviews these AOCS categories as well as previous research into passive, active and semi active AACS.

2.2.2 Passive Aerodynamic Attitude Control Systems

A passive aerodynamic control system will include fixed, or more precisely non-controlled, geometric or mass distribution features which place the center of pressure (COP) behind the center of mass (COM) relative to the incoming free stream velocity vector. These features will cause restoring torques to be generated about the COM to stabilize the spacecraft about one or more axis within some pointing tolerance. Geometric features used to design a passive AACS tend to be external surfaces that make use of aerodynamic lift or drag forces to move the center of pressure behind the COM of the satellite. Two terrestrial examples include the feathers of an arrow or a badminton shuttlecock which aerodynamically stabilize the body in the direction of travel. While a passive AACS design using geometric features tends to focus on changing the location of the COP relative to the COM, a design using mass distribution features focuses on changing the location of the COM relative to the COP. This may be accomplished by adding masses in the direction the designer wishes to move the COM. An arrow is a further example of this concept, as a heavy arrow head moves the COM further ahead of the COP.

Research into passive AACS spacecraft has focused almost entirely on implementing geometric features to change the location of the COP relative to the COM. To the author's knowledge, there has been research into at least one passive AACS making use of mass distribution features. This research focused on the design for the Passive Aerodynamically Stabilized Magnetically Damped Satellite (PAMS) [11], [54], shown in Figure 3. PAMS was flown as part of a Space Shuttle hitchhiker mission in May of 1996 to demonstrate the feasibility of passive aerodynamic stabilization [55]. As shown in Figure 3, PAMS was designed to have an outer shell created of two materials of different densities in order to change the location of the center of mass along the x axis (the direction of nominal velocity).

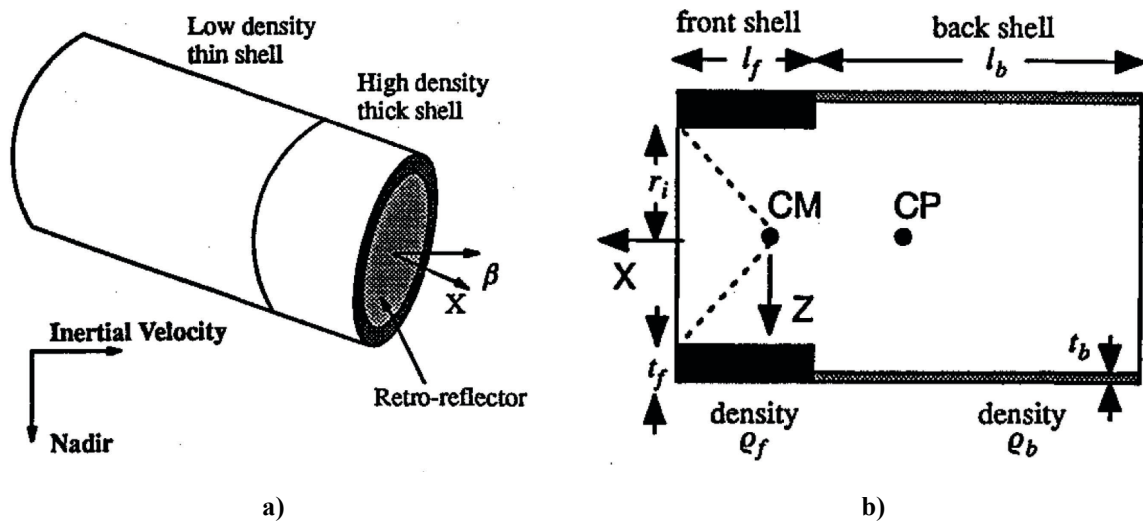
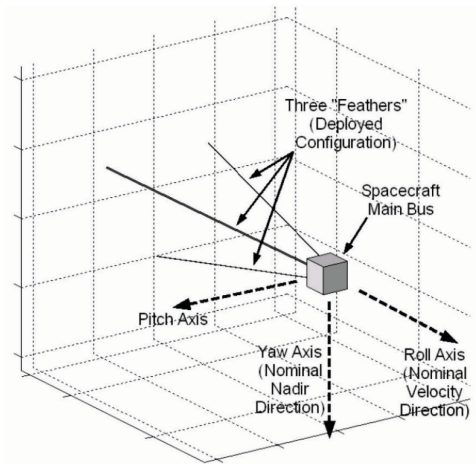


Figure 3: Schematic of PAMS showing its mass distribution design implemented using two cylindrical shells of different densities. (Adapted from [11])

Passive AACS design using mass distribution features has not been explored for CubeSats primarily because of the launch vehicle requirement for the COM to be within 20 mm of the center of geometry of the CubeSat, thus requiring any meaningful changes of COM to be made post deployment [44], [56].

Passive AACS configurations using geometric features have been thoroughly explored and, in some cases, tested in orbit. Configurations that have been explored include using deployed antennas, or feathers, in a badminton shuttlecock configuration [8], [14] using deployable solar panels or control surfaces to achieve a spacedart configuration [13], [13], [56], [57], or using a

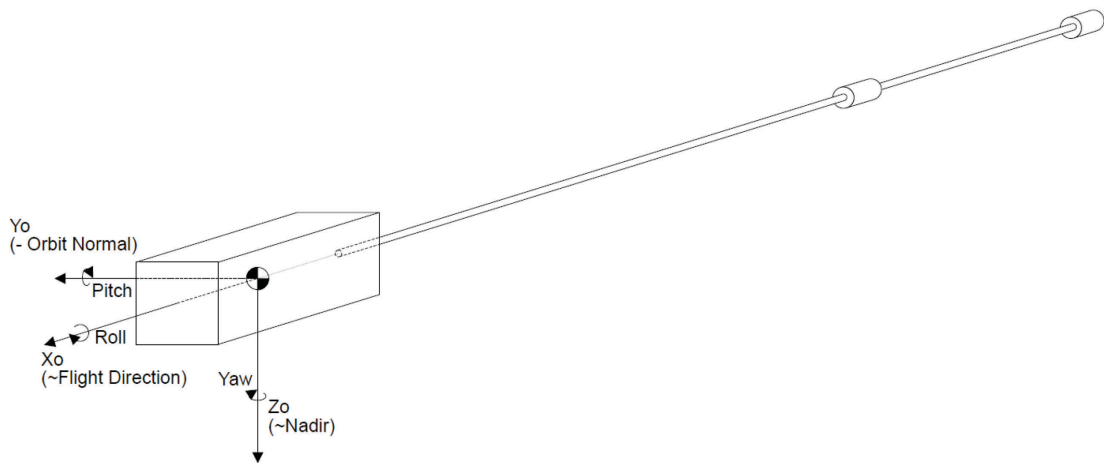
boom deployed directly out the aft face of the CubeSat [58]. Examples of all three of these configurations are shown in Figure 4.



**a) Badminton Shuttlecock Configuration
(Adapted from [8])**



**b) Space Dart Configuration (Reprinted [13], [59],
photo credit Pumpkin Inc.)**



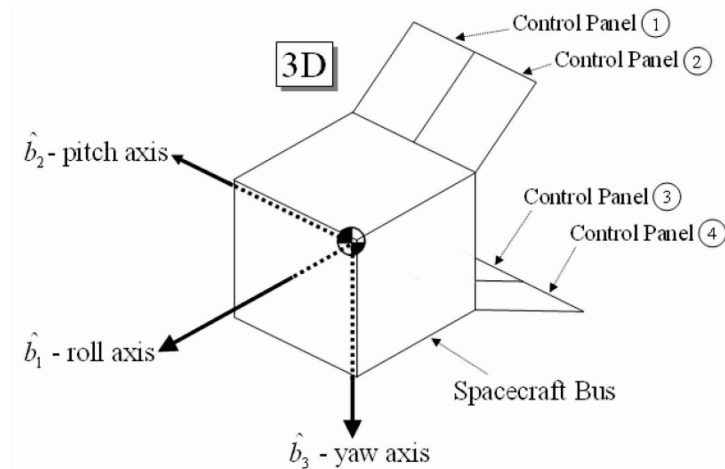
c) Deployed Boom Configuration (Reprinted from [58], 1997)

Figure 4: Passive AACS Geometric Configuration Examples

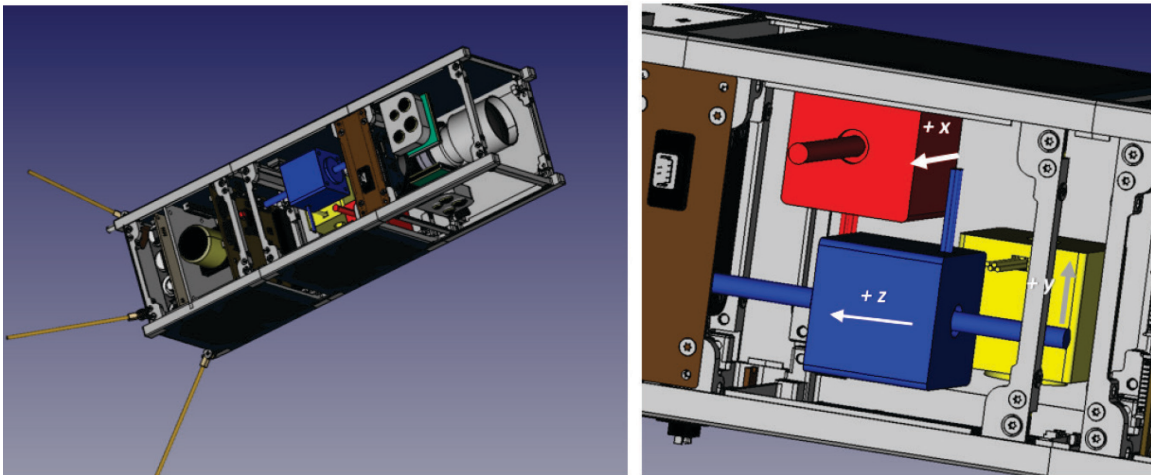
It is important to note that in all these cases, three axis control is not provided by the passive AACS, and a separate control system is typically implemented to provide full attitude control if required. In addition, aerodynamic torques do not provide any damping to the system, and active or passive magnetic control, or momentum control, is implemented in addition to the AACS.

2.2.3 *Active and Semi-Active Aerodynamic Control Systems*

An active AACCS controls geometric or mass distribution features to control the placement of the COP or the COM relative to each other and the incoming flow vector. This enhanced control generates restoring torques to control the satellite's attitude about some axis. Figure 5 shows examples of active AACCS that use both geometric and mass distribution control methods. Active methods differ from passive methods only in that they are actively controlled by some control algorithm.



a) Actively controlled aerodynamic control surfaces for attitude control (adapted from [10])



b) Actively controlled shifting masses for attitude control (adapted from [12])

Figure 5: Active AACS Examples

Active AACS, using both geometric and mass distribution features, have been the focus of much study in the past decade. Active geometric AACS configurations include the use of gimbaled control surfaces (usually deployable solar panels) [7], [10], [16], [60]–[62], internal shifting masses [12], [63] or solar sails [17].

It is worth noting that a combination of both passive and active AACS, the semi-active AACS, is possible and has been explored at least once. This work was completed by Jacoba Auret and Willem H. Steyn, and combined a badminton shuttlecock style passive AACS with active roll paddles to provide three axis stabilization [9], [64]. An example of Auret and Steyn’s design is shown in Figure 6.

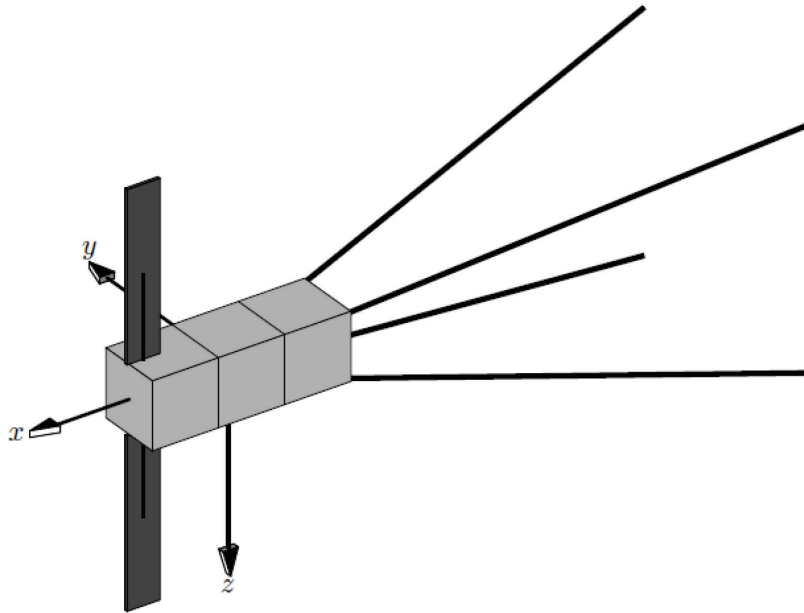


Figure 6: Semi-active AACCS from Auret and Steyn (Adapted from [9])

2.2.4 Aerodynamic Orbit Control Systems

AOCS systems can be subdivided into systems that cancel out the aerodynamic drag force, or those which use the aerodynamic drag force, both for station keeping or orbital maneuvers. Those that oppose the drag force tend to include two things, a propulsion system with very high specific impulse (typically electric) and an attitude control system used to minimize the drag area. There are few examples operating in VLEO, however. Examples of these AOCS include the Super Low Altitude Test Satellite (SLATS) which is currently orbiting in VLEO [23], [24], the yet to be launched Satellite for Orbital Aerodynamics Research (SOAR) [7] (which is in fact the only example of an AAOCS), and the Gravity Field and Steady State Ocean Circulation Explorer (GOCE) satellite [25], [65].

AOCS systems which use the aerodynamic force, use it as a reverse thrust for orbital rendezvous, formation flight, collision avoidance, and controlled re-entry [16]. This can be accomplished using active aerodynamic control surfaces ([7], [15], [16], [19], [21], [60], [61]), solar/drag sails [17], or simply by changing the orientation of the spacecraft relative to the free stream velocity vector. The change in orientation changes its aerodynamic drag area ([18], [20], [22]). This subject has been explored extensively: Varma [15] provides an excellent resource of previous work done in this field.

2.2.5 *Comparison of Simulations Developed for Previous Research*

A better sense of the previous research in AAOCS may be obtained by comparing the simulations used by the respective authors for their research. Table 2 provides a comparison of most of the previously reviewed research on AACS and compares them based on the type of AACS, the type of orbital propagator used, the disturbance forces and torques modeled, the aerodynamic model used for analysis, and the atmospheric model used. Note that while not all the AACS and AACS have been listed, what is shown is fairly representative of the whole. For the most part, each author had developed their own simulation for analysis, and while there are other characteristics that may be compared (magnetic model for example), only the characteristics deemed most relevant to AACS design were chosen for comparison.

The type of AACS compared includes passive (P), active (A), and active/passive (A/P). The propagator comparison includes only Simplified General Perturbations 4 (SGP4) and, custom models classified as “Numerical.” A variety of numerical integrators are available, and their comparison is outside the scope of this thesis. However, the use of SGP4 is within the scope, as SGP4 takes aerodynamic drag into account [66], and its use affects long-term accuracy. The forces and torques compared include two-body point mass gravity, non-uniform gravity, solar radiation pressure (SRP), aerodynamic, residual magnetic, gravity gradient, and gravity forces from third bodies. The aerodynamic models compared include simplified aerodynamics, where the drag force equation without attitude considerations is used, the panel method, the ray tracing / line scanning method, and Direct Simulation Monte Carlo (DSMC) methods ([67] and [68] provides an excellent overview of the last three models).

Table 2: Comparison of Simulation Characteristics used for Previous AACs Research

Reference		[11]	[54]	[8]	[64]	[10]	[61]	[60]	[14]	[57]	[56]	[13]	[69]	[58]	[12]
Control Type		P	P	A/P	A	A	A	P	P	P	P	P	P	P	A
SGP4 Propagator				X				X							
Numerical Propagator		X	X		X	X		X	X	X	X	X	X	X	X
Forces	Gravity - Point Mass		X	X	X	X	X	X	X	X	X	X	X	X	X
	Gravity – Higher Order	X					X								
	Solar Radiation Pressure	X					X								
	Aerodynamic	X					X								X
	Third Body Gravity														
Torques	Gravity-Gradient	X	X	X			X	X	X	X	X	X	X	X	
	Solar Radiation Pressure	X	X				X				X				
	Residual Magnetic										X	X			
	Aerodynamic	X	X	X	X	X	X	X	X	X	X	X	X	X	X
Aerodynamic Modelling	Simplified Aerodynamics														
	Panel Method		X	X	X	X	X	X	X			X	X	X	
	Ray Tracing / Line Scan Method	X													
	Direct Monte Carlo Simulation										X				
Atmospheric Models	Exponential model			X	X				X	X		?			
	NRLMSISE-00						X					?			X
	Jacchia Bowman 2006/2008											?			
	Other	X	X						X			?	X		

Table 2 provides an interesting picture regarding the previous research into aerodynamic AACs. There are several things to note here: first, the choice of orbital propagation between SGP4 and custom models, which is tied in with the second observation, that few simulators considered external forces and their effects on spacecraft orbit. These forces change the orbital profile of the satellite by, for example, changing eccentricity, changing altitude, or causing small oscillations in the satellite’s altitude around its nominal orbit. This connects with modelling an AACs because of how atmospheric density changes depending on altitude, latitude, longitude, seasonal variations, geomagnetic fluctuations, whether the satellite is on the day or night side, solar activity, tidal effects, and other factors [46]. Thus, the choice to model external forces directly contributes to

the magnitude and direction of aerodynamic perturbations, and the dynamic response of the spacecraft in general. For example, [54] describes the resonances induced by the drop in density going from sunlit to eclipse phase of the orbit, as well as by solar torques, which intuitively may affect the feasibility and design of an AACS.

It seems that few researchers considered the modelling of orbital dynamics important to their research into AACS. Alternatively, few had access to a simulation package that modeled satellite dynamics under the effect of both forces and torques, prioritizing the design, and testing of the control system before refining the astrodynamics model. Another alternative may be the short time scale of the analysis involved, but this is unlikely considering that [11], [54] had a similar time frame (and interestingly [20], was the only one with an in-orbit demonstration [56][20]).

The third observation from Table 2 is that few considered SRP torque or spacecraft residual magnetic torque. Fourth, as expected, none considered a simplified aerodynamic model, but the majority chose the panel method as opposed to higher-order methods. Lastly, the choice of atmospheric models has been interesting. While there are only a few choices listed in Table 2, the category “Other” contains a number of different atmospheric models (as a side note, NRLMSIS-00 and JB-06/08 were listed due to the recommendations in [67]). It is also interesting to note that, in general, there is not much uniformity regarding the assumptions made in each of the AACS studies. However, any conclusion drawn from that would require context from the specific research, as each spacecraft configuration, research objective, and orbital regime is different.

2.3 Existing Orbital Dynamics and Control Simulators

Various software packages exist for orbital simulations. They may be commercial, open-source, developed by academic institutions for research, or freeware (freely available, but not open source). Additionally, some of these software packages are holistic in their focus, a good example being Systems Tool Kit (STK) by AGI [27], which has plugins that cover every tool required for space mission design. But many software packages are application specific, such as Orbitron [70], which is used for satellite tracking. For this thesis, while many software packages were found, only software which is intended for modelling spacecraft dynamics (either translational or rotational) is examined.

Table 3 compares commercial (C), open source (O), and academic (A) simulators based on their capabilities in modelling astrodynamics. While there are many other characteristics worth comparing, it was decided to choose only the most important regarding the modelling of astrodynamics and aerodynamics. To that end, we compare everything that was modeled in 2.2.5, except for numerical integration method.

Table 3: Simulation Software Comparison

		Free Flyer [26]	STK [27]	ASTOS [28]	SCT [29]	HPOP [30]	GMAT [71]	JAT [32]	Tudat [33]	Orekit [34]	Unnamed [35]	Unnamed [36]	HPS [37]	SPACSSIM [38]	Unnamed [39]	Open-SESSAME [40]	PROPAT [41]	SAODS [72]
License		C	C	C	C	C	O	O	O	O	A	A	A	A	A	O	A	A
Forces	Gravity - Point Mass	X	X	X	X	X	X	X	X	X	X	X	X	X	X	X	X	X
	Gravity – Higher Order	X	X	X	X	X	X	X	X	X	X		X	?	X			X
	Solar Radiation Pressue	X	X	X	X	X	X	X	X	X	X		X	?	X	X		X
	Aero	X	X	X	X	X	X	X	X	X	X	X	?	?	X	X		X
	Third Body	X	X	X	X	X	X	X	X	X			?	?	X	X		
Torques	GG		X	X	X			X			X	X	X	X	X	X	X	X
	SRP		X	X	X						X		?	X	X	X		
	Residual Magnetic		X	X	X						X		?	X	X	X	X	X
	Aero		X	X	X						X	X	?	X	X	X		X
Aerodynamic Modelling	Simplified		X	X	X		X	X	X	X			?	?		X		X
	Panel Method		X	X		X			X	X	X	X	?	?	X			
	Ray Tracing / Line Scan Method					X							?	?				
	DSMC												?	?				
Atmospheric Models	Exponential	X	X		X				X	X		?		?	X	?		?
	NRLMSISE -00	X	X	X			X		X	X		?	X	?	X	?		?
	Jacchia Bowman 2006/2008			X						X		?	X	?	X	?		?
	Other	X	X	X	X	X	X	X	X	X	X	?	X	?	X	?		?

Examining Table 3 reveals several interesting facts. First, if disturbance torque modelling is a user requirement, only one open source option and three commercial options are available, while the modelling of disturbance forces is ubiquitous. Second, commercial offerings have two further constraints not captured in Table 3, specifically, the software price and its accessibility. For example, STK has the SOLIS add-on module for guidance, navigation, and control (GNC) design. SOLIS models environmental disturbances and allows the user to design the GNC system for the satellite. This module is export-controlled by the US, and it could not be obtained by the author in Canada. Another constraint is price. For example, the Satellite Control Toolbox (SCT) by Princeton Satellite Systems sells for \$1000 for academic users and \$3000 for commercial users, while a module for STK may cost as much as \$10,000 [40]. Also, regarding Open-SESSAME, two barriers exist. The first being that the code has not been updated since 2004, and the project does not seem to be active. This may present some software compatibility issues in the present day. This is further complicated by the second barrier: the software and library is written in C++. However, this coding language is only a barrier if the user is not familiar with C++ or the user does not have a compiler. Finally, regarding simulations created by academics, it seems that whatever capability was not available to them (for whatever reason) from commercial or open-source packages, was obtained through independently made simulations. However, accessing these software packages from the researcher may be difficult, if these packages have not been made open-source.

The second item of note is the aerodynamic model. Specifically, almost all the software packages use either simplified aerodynamics or the panel method to determine the aerodynamic force and torque acting on the spacecraft. Only SCT uses the ray tracing / line scan method. None use DSMC. As a result, only SCT's software would be able to model the effects of a solar panel (or an aerodynamic control surface) shadowing another solar panel or some other part of the spacecraft from aerodynamic perturbations. For aerodynamic attitude control, this may have a significant effect on the fidelity of the simulation model, depending on spacecraft configuration.

The third item of note is the available atmospheric models. Specifically, what is available may vary depending on the software. The "Other" category holds several different atmospheric models in addition to the exponential, NRLMSISE-00, and Jacchia-Bowman. For aerodynamics, the atmospheric model used and the input variables that affect the atmospheric model during simulation may have significant effects on the aerodynamic force experienced by the spacecraft.

It is worth noting that many of the simulators do offer the ability to add an external atmospheric model. An excellent resource on the importance of choosing the right atmospheric model and correctly modelling its inputs is provided by Vallado and Finkleman [67].

2.4 Research Proposal

2.4.1 Research Gap

Reviewing the information presented in this chapter, and shown in Table 2 and Table 3, several things are noted:

1. Size limits a CubeSats performance, but this limitation can be reduced by orbiting in VLEO using an AAOCS.
2. AAOCS not only has the potential to improve the performance of CubeSats, but also to improve the performance of satellite missions in general (especially Earth observations).
3. Previous research into AACS and AOCS has rarely been demonstrated in-orbit (except for AOCS, which use the aerodynamic force for orbital maneuvers), with a full AAOCS having never been demonstrated.
4. Previous research has relied on self-created dynamics simulations that neglect certain perturbations. This research could benefit from a simulation package which holistically considers perturbation forces and torques acting on a spacecraft.
5. There are significant barriers to using commercial and open-source astrodynamics software for AAOCS development, either because of a lack of capability or cost.

From these facts, we conclude that there is no easily accessible simulation software that models spacecraft dynamics and environmental perturbations at the level required for AAOCS design.

2.4.2 Research Proposal and Justification

To solve this problem, which is required to take the next step in AAOCS design, an open-source astrodynamics simulation software (and accompanying library) will be developed in MATLAB/Simulink. The simulation software should allow the user to model six degree of freedom rigid body dynamics of a satellite in orbit around Earth and the accompanying environmental perturbations including:

- Two-body and higher order gravity forces
- Gravity gradient torque
- Third-body gravity
- Solar radiation pressure forces and torques using either a simplified model, the panel method, or ray tracing (this last feature is not a hard requirement, but a good goal to reach for).
- Aerodynamic forces and torques using either a simplified model, the panel method, or ray tracing (same as for solar radiation pressure).
- Residual magnetic torque

The software will be developed using MATLAB/Simulink because of its compatibility with Windows, Mac, and Linux operating systems, as well as the ubiquitous nature of MATLAB/Simulink in the university environment. Additionally, MATLAB/Simulink has extensive existing libraries for modelling dynamics systems and for aerospace applications. Finally, developing this software in Simulink will allow the package to be readily used for control design.

3 Background

Predicting the state of a satellite's attitude and orbital trajectory requires a mathematical model that describes the dynamic response of the satellite to forces and torques from the environment, either as disturbances or controls. The following reviews the background information necessary to understand the theory used to create the satellite simulation environment developed for this thesis. This chapter also describes the mathematical model used by the simulation environment to simulate satellite dynamics. Beginning with a description of coordinate systems, this chapter then reviews orbit propagation methods. After the review of these methods, the defining of the dynamics of a rigid body with six degrees of freedom follows. The geometric and inertial properties of a satellite are then discussed. To conclude, the mathematical description of each disturbance force and torque is defined.

3.1 Coordinate Systems, Transformations and Time

There are several coordinate systems used in this thesis to simulate a satellite's orbital trajectory and attitude response as a result of environmental perturbations. The major coordinate systems and transformations used in this thesis are described in this section. These are the Earth Centered Inertial (ECI), Keplerian, the Earth Centered Earth Fixed (ECEF), Local Vertical Local Horizontal (LVLH), and the Body Fixed Frame (BFF) coordinate systems.

3.1.1 ECI and Keplerian Coordinate Systems and Transformations

Figure 7 shows the ECI coordinate system (referred to as the I-frame) as well as the Keplerian coordinate system. This thesis and the accompanying simulation uses the International Celestial Reference System (ICRS) [73] as a reference for the I-frame. The I-frame is an inertial Cartesian coordinate system with the origin at the center of the Earth. The X_I axis points toward the Vernal Equinox, the Z_I axis points towards the Celestial North Pole along the Earth's rotation axis (It is noted here that the Earth rotates counter clockwise when viewed from above, the positive rotation direction about the Z axis) and the Y_I axis completes the right-handed orthogonal coordinate system. For the purposes of simulation developed in this thesis, the I-frame is assumed to be inertial. The orbit of a satellite in the I-frame is defined by its position and velocity vector. [73] [74]

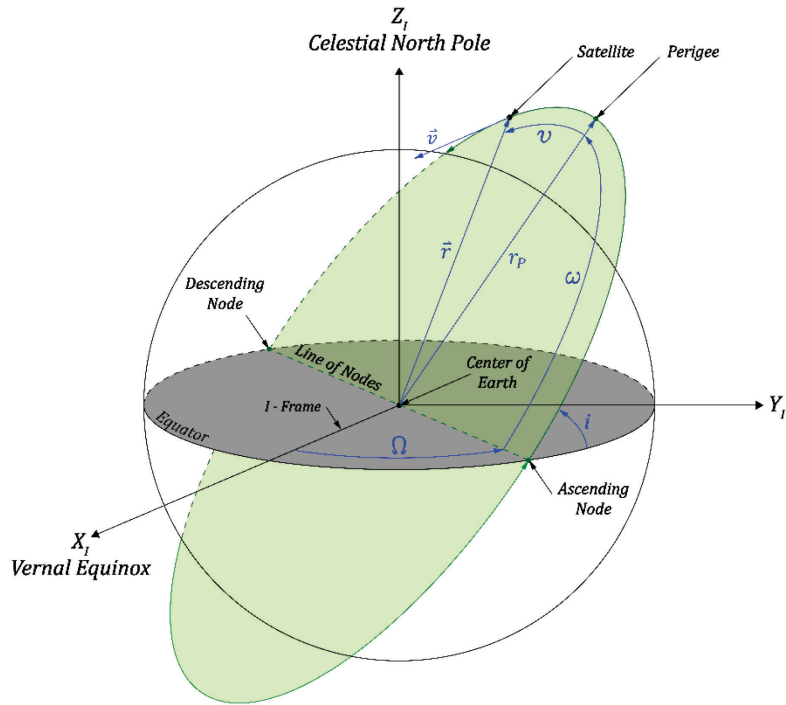


Figure 7: Earth Centered Inertial Coordinate System and Keplerian Elements

The Keplerian coordinate system is also shown in Figure 7 and defines the position of the satellite using six values (only four are shown) called Keplerian Elements. Keplerian Elements are used to describe and visualize the position of the satellite as this visualization is more intuitive and useful, whereas the I-frame coordinate system works well for computer simulations. The Keplerian Elements of currently orbiting satellites are posted by NORAD on www.space-track.org in the Two-Line Element (TLE) format. The Keplerian Elements are measured relative to the Vernal Equinox, the Celestial North Pole, and the Equatorial Plane. The symbols, units, and a description of the Keplerian Elements are provided below in Table 4. [74]

Table 4: Keplerian Elements

Symbol	Keplerian Element	Units	Description
Ω	Right Ascension of the Ascending Node (RAAN)	deg	Angle measured on the equator from the vernal equinox to the ascending node.
i	Inclination	deg	Angle measured between the north side of the equatorial plane and the orbital plane to the right of the ascending node.
ω	Argument of Perigee	deg	The angle between the ascending node and perigee.
ν	True Anomaly	deg	The angle between perigee and the satellites current position.
e	Eccentricity	Unitless	The eccentricity of the satellites orbit.
a	Semi-major Axis	kilometers (km)	The semi-major axis of the ellipse formed by the satellites orbit, or rather, the average distance from the center of the Earth to the satellite during its orbit.

Typically, the Keplerian elements of a satellite are transformed into the state vectors in the I-frame for simulation, while the opposite transformation is used for visualizing how a satellite's orbit changes over time. The transformation from Keplerian elements into state vectors begins with the calculation of the radius of perigee as shown in equation 3-1 [75],

$$r_p = a(1 - e) \quad 3-1$$

where r_p is the radius of perigee of the satellites orbit in m. Then, the radius of apogee is calculated as in equation 3-2 [75],

$$r_a = a(1 + e) \quad 3-2$$

where r_a is the radius of apogee of the satellites orbit in m. These quantities can then be used to calculate the semi-minor axis as in equation 3-3 [75],

$$b = \sqrt{r_p r_a} \quad 3-3$$

where b is the semi-minor axis calculated in m. Equation 3-4 [75] shows the next step, calculating the peri-focal distance,

$$c = e \cdot a \quad 3-4$$

where c is the peri-focal distance in m. Following this, the distance between the satellite and the center of the Earth can be calculated as shown in equation 3-5 [75],

$$r_s = \frac{a(1 - e^2)}{1 + e \cos v} \quad 3-5$$

where r_s is the distance between the center of the Earth and the satellite in m. This can be used to locate the position vector of the satellite if it were in an equatorial orbit as in equation 3-6,

$$\vec{r}_s = \begin{bmatrix} r_s \cos(\omega + v) \\ r_s \sin(\omega + v) \\ 0 \end{bmatrix} \quad 3-6$$

where \vec{r}_s is the position vector of the satellite in the I-frame in m. From here, the angle between the semi-major axis and the satellite's velocity vector can be determined as in equation 3-7,

$$\alpha = \arctan \frac{b^2(r_{sx} + c \cdot \cos \omega)}{a^2(r_{sy} + c \cdot \sin \omega)} \quad 3-7$$

where α is the angle in radians, r_{sx} is the x component of the satellites position in a equatorial orbit as previously calculated, and r_{sy} is the y component. This can be used to determine the satellite's velocity vector in an equatorial orbit as in equation 3-8 [75],

$$\vec{v}_s = \begin{cases} \begin{bmatrix} \cos \alpha \sqrt{\frac{2\mu}{r_s} - \frac{\mu}{a}} \\ -\sin \alpha \sqrt{\frac{2\mu}{r_s} - \frac{\mu}{a}} \\ 0 \end{bmatrix} & \text{for } 2\pi > (\omega + v) > \pi, \text{ wrapped to } 2\pi \\ \begin{bmatrix} -\cos \alpha \sqrt{\frac{2\mu}{r_s} - \frac{\mu}{a}} \\ \sin \alpha \sqrt{\frac{2\mu}{r_s} - \frac{\mu}{a}} \\ 0 \end{bmatrix} & \text{Otherwise} \end{cases} \quad 3-8$$

where \vec{v}_s is the satellite's velocity vector in $\frac{m}{s}$ in the I-frame. Finally, the satellite's position and velocity vector must be rotated into its correct orbit plane as shown in equation 3-9,

$$R = \begin{bmatrix} 1 & 0 & 0 \\ 0 & \cos i & -\sin i \\ 0 & \sin i & \cos i \end{bmatrix} \begin{bmatrix} \cos \Omega & -\sin \Omega & 0 \\ \sin \Omega & \cos \Omega & 0 \\ 0 & 0 & 1 \end{bmatrix} \quad 3-9$$

where R is the rotation matrix representing the orientation of the satellite's true orbital plane relative to equatorial plane. Finally, equations 3-10 and 3-11 show the transformation between the equatorial position and velocity vector of the satellite to its true orbital position and velocity vector,

$$\vec{r}_{IB}^I = R \vec{r}_s \quad 3-10$$

where \vec{r}_{IB}^I is the position vector of the satellite relative to the I-frame in m,

$$\vec{v}_{IB}^I = R \vec{v}_s \quad 3-11$$

where \vec{v}_{IB}^I is the velocity vector of the satellite relative to the I-frame in $\frac{m}{s}$.

To make the transformation from state vectors to Keplerian elements, a different process is used. First, the orbital momentum vector is determined as in equation 3-12 [76],

$$\vec{h} = \vec{r}_{IB}^I \times \vec{v}_{IB}^I \quad 3-12$$

where \vec{h} is the orbital momentum vector in $\frac{m^2}{s}$, \vec{r}_{IB}^I is the satellite's position vector in the I frame in m, and \vec{v}_{IB}^I is the satellites velocity vector in the I frame in $\frac{m}{s}$. Then, the eccentricity vector is calculated as in equation 3-13[76],

$$\vec{e} = \frac{\vec{v}_{IB}^I \times \vec{h}}{\mu} - \frac{\vec{r}_{IB}^I}{\|\vec{r}_{IB}^I\|} \quad 3-13$$

where \vec{e} is the unitless eccentricity vector and μ is Earth's standard gravitational parameter (see Appendix A for constants used in this thesis). Then, the vector pointing towards the ascending node is calculated using equation 3-14 [76],

$$\vec{n} = \begin{bmatrix} 0 \\ 0 \\ 1 \end{bmatrix} \times \vec{h} \quad 3-14$$

where \vec{n} is the vector pointing toward the ascending node of the satellites orbit from the center of the Earth. Using \vec{n} , the true anomaly of the satellite may be calculated as in equation 3-15 [76],

$$v = \begin{cases} \arccos \frac{\vec{n} \cdot \vec{e}}{\|\vec{n}\| \|\vec{e}\|} & \text{for } e_z \geq 0 \\ 2\pi - \arccos \frac{\vec{n} \cdot \vec{e}}{\|\vec{n}\| \|\vec{e}\|} & \text{for } e_z < 0 \end{cases} \quad 3-15$$

where v is the true anomaly of the satellite in radians. The inclination can also be calculated using the orbital momentum vector as in equation 3-16 [76],

$$i = \arccos \frac{h_z}{\|\vec{h}\|} \quad 3-16$$

where i is the inclination of the satellite's orbit in radians. Finally, RAAN, the argument of perigee and semi-major axis be calculated using equations 3-17, 3-18 and 3-19[76],

$$\Omega = \begin{cases} \arccos \frac{n_x}{\|\vec{n}\|} & \text{for } n_y \geq 0 \\ 2\pi - \arccos \frac{n_x}{\|\vec{n}\|} & \text{for } n_y < 0 \end{cases} \quad 3-17$$

where Ω is the Right Ascension of the Ascending Node (RAAN) in radians,

$$\omega = \begin{cases} \arccos \frac{\vec{n} \cdot \vec{e}}{\|\vec{n}\| \|\vec{e}\|} & \text{for } e_z \geq 0 \\ 2\pi - \arccos \frac{\vec{n} \cdot \vec{e}}{\|\vec{n}\| \|\vec{e}\|} & \text{for } e_z < 0 \end{cases} \quad 3-18$$

where ω is the argument of perigee in radians,

$$a = \frac{1}{\frac{2}{\|\vec{r}_{IB}^I\|} - \frac{\|\vec{v}_{IB}^I\|^2}{\mu}} \quad 3-19$$

and where a is the semi-major axis of the satellites orbit in m.

3.1.2 ECEF and LVLH Coordinate Systems and Transformations

Figure 8 shows the ECI coordinate system, the Earth Centered Earth Fixed (ECEF) coordinate system (the E-frame), and the Local Vertical Local Horizontal (LVLH) coordinate system (the O-frame). The ECEF coordinate system is a Cartesian coordinate system with the origin at the center of Earth that rotates with the Earth. The X_E axis intersects the equator at Earth's prime meridian (0° longitude), the Z_E axis points towards the Celestial North Pole and is co-linear with the Z_I axis of the I-frame while the Y_E axis completes the right-handed orthogonal coordinate system. This thesis and accompanying simulation use the International Terrestrial Reference Frame (ITRF) to model the E-frame. [73]

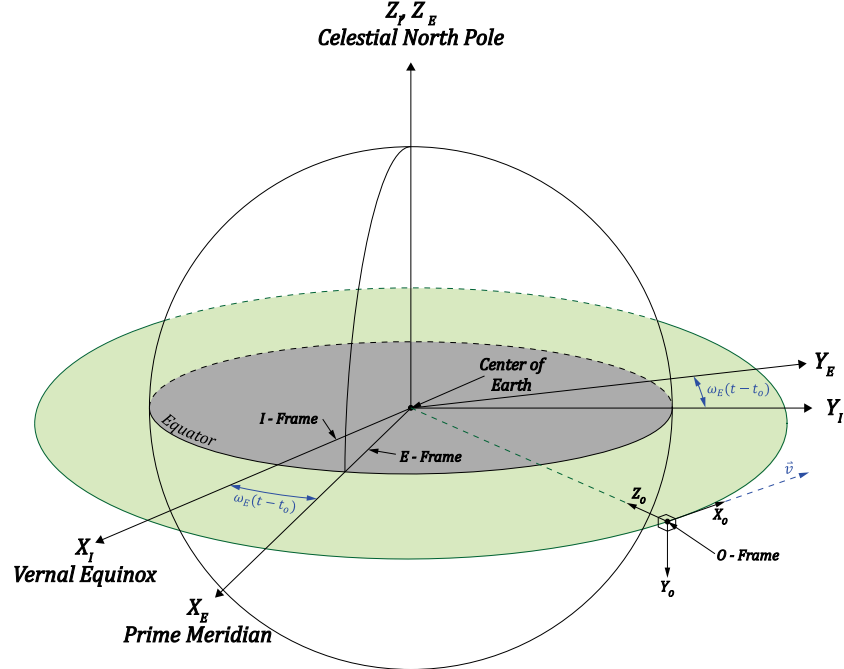


Figure 8: ECEF, ECI and LVLH Coordinate Systems

Figure 8 shows a simplified relationship between the I-frame and the E-frame as the angle the E-frame rotates by with respect to the I-frame being equal to $(GMST + \omega_E t)$. This relationship can be represented by the rotation matrix shown in equation 3-20 [77],

$$R(t) = \begin{bmatrix} \cos(GMST + \omega_E t) & \sin(GMST + \omega_E t) & 0 \\ -\sin(GMST + \omega_E t) & \cos(GMST + \omega_E t) & 0 \\ 0 & 0 & 1 \end{bmatrix} \quad 3-20$$

where $R(t)$ is the rotation matrix representing the orientation of the I-frame with respect to the E-frame, $GMST$ is Greenwich Mean Sidereal Time (GMST) in radians, ω_E is the Earth's angular velocity in $\frac{\text{rad}}{\text{s}}$, t is the time in seconds from some known epoch, and $\omega_E t$ represents the angle around Earth's rotation axis that the E-frame is offset from the I-frame relative to some known epoch. In this thesis, the J2000 epoch is used for a temporal reference for the orientation of the E-frame relative to the I-frame. The rotation angle of the E-frame relative to the I-frame is calculated using equation 3-21 [74] for GMST relative to the J2000 epoch,

$$GMST = 2\pi(0.7790572732640 + 1.00273781191135448 \times (JD - 25451545.0)) \quad 3-21$$

where GMST is the hour angle between the prime meridian and the Vernal Equinox on January 1, 2000 at 12:00:00 [78] Coordinated Universal Time (UTC) measured in radians, and JD is the Julian Date, as in equation 3-22, at the time of calculation,

$$JD = 1,721,013.5 + 367Y - INT\left\{\frac{7}{4}\left[Y + INT\left(\frac{M+9}{12}\right)\right]\right\} + INT\left(\frac{275M}{9}\right) + D + \frac{60h + m + \frac{s}{60}}{1440} \quad 3-22$$

where JD is the Julian Date, Y is the year, M is the month, D is the day, h is the hour, m is the minutes and s is seconds.

However, the Earth's orientation with respect to the I-frame is more complex than what is shown in Figure 8 and equation 3-20. In fact, the Celestial Pole is not fixed in space and changes due to polar precession, nutation, and polar motion [79]. Equation 3-23 [73] more accurately represents the orientation of the I-frame with respect to the E-frame,

$$R_{EI}(t) = Q(t)R(t)W(t) \quad 3-23$$

where $R_{EI}(t)$ is the rotation matrix representing the orientation of the I-frame with respect to the E-frame, considering polar motion and motion of the celestial pole. $Q(t)$ represents the rotation matrix defining the motion of the celestial pole; $R(t)$ is as was defined in 3-20, and $W(t)$ is associated with polar motion [79]. These realizations are described in detail in [79], and will not be repeated here. However, it is noted that Earth Orientation Parameters (EOP) provided by Celestak [80] are used to obtain this realization in the simulation. As $R_{EI}(t)$ is a rotation matrix belonging to $SO(3)$, the inverse is simply $R_{EI}^{-1} = R_{EI}^T = R_{IE}$ which represents the rotation matrix used to transform from the E-frame to the I-frame.

Figure 8 also shows the O-frame and its relationship to the I-frame. The O-frame is a Cartesian coordinate system with the origin rotated at the center of mass of the satellite. In the O-frame, the X_O axis points in the direction of the satellite's nominal velocity. Note that the direction of nominal velocity is tangent to the orbital trajectory only for circular orbits or two locations in an elliptical orbit. The Z_O axis points towards Nadir, or rather, pointing directly towards the center of the Earth, and the Y_O axis completes the right-handed orthogonal coordinate system, and points in the direction opposite the orbital momentum vector. The transformation between the I-frame and the O-frame is shown in equation 3-24 [14],

$$R_{IO} = \begin{bmatrix} \left(\hat{r}_{IB}^I \times (\hat{v}_{IB}^I \times \hat{r}_{IB}^I) \right)^T \\ (\hat{v}_{IB}^I \times \hat{r}_{IB}^I)^T \\ -(\hat{r}_{IB}^I)^T \end{bmatrix} \quad 3-24$$

where R_{IO} is the rotation matrix representing the orientation of the O-frame with respect to the I-frame, \hat{r}_{IB}^I is the satellite's position unit vector in the I-frame and \hat{v}_{IB}^I is the satellite's unit

velocity vector in the I-frame. The rotation matrix representing the orientation of the I-frame with respect to the O-frame is simply $R_{OI} = R_{IO}^T$.

Figure 9 shows the O-frame and the Body Fixed Frame (BFF, also referred to as the B-frame). The B-frame is a Cartesian coordinate system with the origin fixed at the origin of the O-frame and is fixed to the satellite body. The X_B axis, also known as the roll axis, typically points towards the front of the spacecraft. The Z_B axis, also known as the yaw axis, typically points towards the Nadir side of the spacecraft. The Y_B axis, also known as the pitch axis, typically points towards the starboard side of the spacecraft. Figure 9 is also an example of why the O-frame is important. Usually, the attitude of the satellite is measured as the orientation of the B-frame relative to the O-frame.

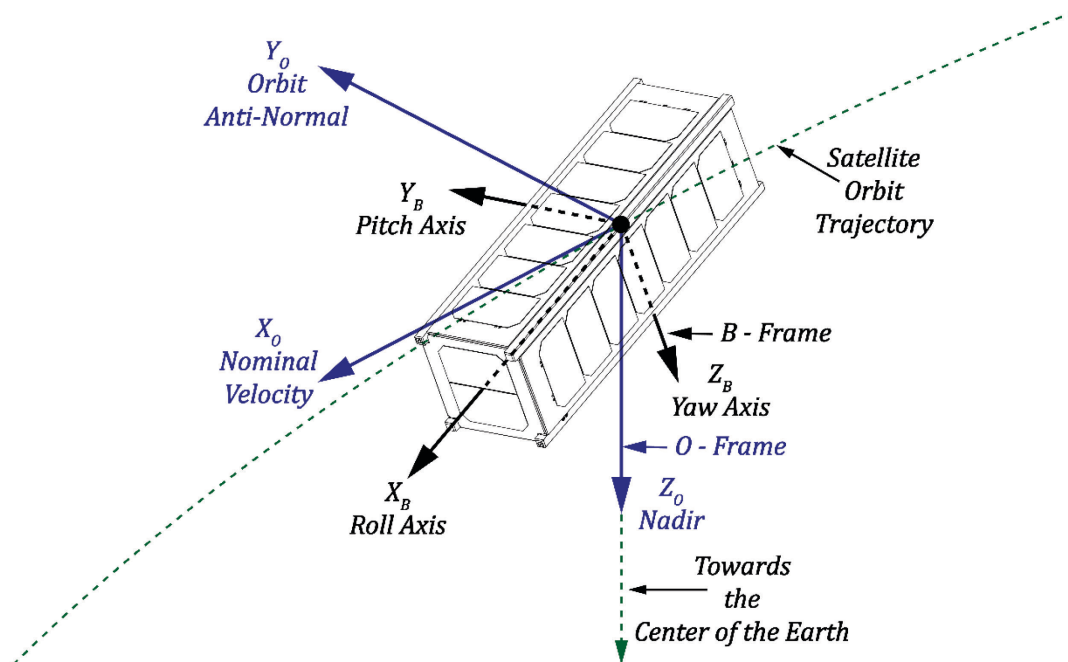


Figure 9: LVLH Coordinate System and Body Fixed Frame

Equation 3-25 shows the transformation matrix between the B-frame and the O-frame,

$$R_{OB} = R_{IO}^T R_{IB} \quad 3-25$$

where R_{OB} is the rotation matrix representing the orientation of the B-frame with respect to the O-frame.

3.2 Orbit Propagation Methods

Orbit propagation is a technique used to predict the future position and velocity of a satellite as a function of some known position and velocity during a past or present time [81]. This is the fundamental problem astrodynamics simulators are created to solve for a variety of applications. For example, determining when a satellite passes over a ground station to setup a communications link for downloading data or uploading commands, determining when a satellite will pass over an area ravaged by a natural disaster to capture images of the scene, designing the launch of a rocket carrying a satellite into orbit, etc. Orbit propagation methods and their advantages and disadvantages will be discussed here.

Several methods have been created to propagate the orbit of satellites. These are divided into special perturbation methods, which use numerical methods to integrate the trajectory dynamics, and general perturbation methods, or analytical methods used to integrate the trajectory dynamics [81], [82]. Special perturbation methods include Cowell's Method, Encke's Method and the Variation of Parameters Method. General perturbation methods include the simplified perturbation models SGP, SGP4, SDP4, SGP8, and SDP8.

Cowell's method is the direct numerical integration of the dynamics (equation 3-26, [42]) and the perturbation forces acting on the satellite,

$$\ddot{\vec{r}} = -\frac{\mu_e}{\|\vec{r}\|^3}\vec{r} + \frac{\vec{f}_p}{m_s} \quad 3-26$$

where $\ddot{\vec{r}}$ is the acceleration vector in $\frac{m}{s^2}$, μ_e is the gravitational parameter of Earth in $\frac{m^3}{s^2}$, and \vec{r} is the position vector from the center of the Earth to the satellite's center of mass in m, \vec{f}_p is the vector representing the perturbation forces acting on the satellite in Newtons, and m_s is the mass of the satellite in kg. All vector quantities are expressed in the ECI frame.

This method's advantage includes the ability to add perturbations to the equations of motion without modification, providing they are in the right reference frame, and to simply implement them. All that is required is writing out the equations of motion for the orbiting satellite, ensuring one has the correct initial conditions and numerically integrating the ODE. However, the disadvantages of this method include being computationally expensive and the rapid accumulation of round-off error. It is worth noting that this method is typically done in a Cartesian reference

frame (ECI), although there are performance enhancements to be found by switching to a spherical or polar reference frame. [42], [81], [83]

Encke's method involves linearizing 3-26 about an ideal reference orbit without perturbations (called the osculating orbit) and integrating the resulting linear time-varying system. The advantages of Encke's method include being about three times faster than Cowell's for Earth orbiting satellites, and about ten times faster for interplanetary satellites [83]. However, Encke's method is more complex in formulation and implementation. The details are found in [1] and [8].

The method of variation of parameters works by linearizing the dynamics of the Keplerian orbital elements and numerically integrating the resulting system. This method has the advantage of being much faster than either Cowell's or Encke's method, as orbital elements change slowly compared to a position vector in Cartesian coordinates. This method is covered in detail in [83].

General perturbation methods attempt to describe the position of a satellite by finding an analytical expression for the dynamics of the Keplerian orbital elements. The variation of parameters method can become a general perturbation method by creating a power series from the equations of motion and integrating the results analytically [42], [83]. The advantages brought by analytical methods include being able to instantaneously determine the state of a satellite at any time without the need for numerical integration. However, the challenges with this method involve finding an analytical expression that accurately describes the equations of motion. This method was used in the creation of the simplified perturbation models [82] which are described in detail in [84].

3.3 Satellite Dynamics

Understanding the state of a satellite's attitude and orbital trajectory in the past, present, and future requires a mathematical model that describes the dynamic response of the satellite to forces and torques produced by the environment or by design. This section describes the mathematical model used by the simulation environment to simulate satellite dynamics and its geometric and inertial properties.

3.3.1 Rigid Body Mechanics

A Keplerian Orbit, which describes an ideal orbit for a satellite, assumes that gravity is the only force acting on the satellite and that both the satellite and Earth can be represented as particles

with a fixed, uniform mass. However, the force of gravity is not the only force acting on the satellite, Earth's mass distribution is non-uniform, and the satellite is not truly a particle. In fact, satellites are typically a non-uniform, non-rigid geometric body with mass, inertia, and other properties (such as a residual magnetic moment). These properties affect how the satellite's environment disturbs the satellite's motion through forces and torques. Additionally, there may be control torques and forces applied to the satellite by some on board system (such as thrusters) to generate some desired motion.

Figure 10 is a free body diagram (FBD) of a 3U CubeSat which shows the resultant forces and torques acting on the satellite; these are composed of individual forces and torques acting on the satellite from the environment or from actuators. Figure 10 also shows the resulting linear and angular acceleration of the satellite produced by resultant forces and torques.

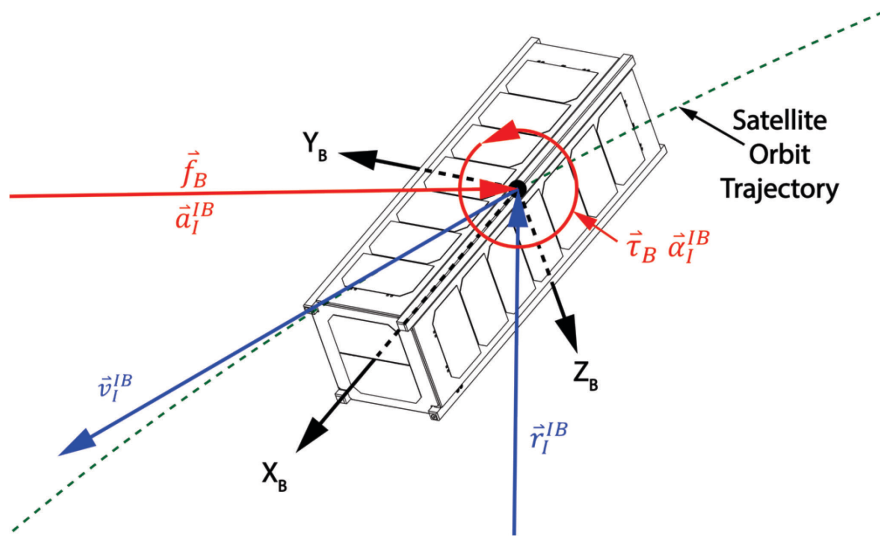


Figure 10: Free body diagram showing the vector sum of the forces and torques acting on a 3U CubeSat in orbit

To model a satellite's motion under the action of forces and torques in this thesis, the satellite will be modeled as a rigid body. Care should be taken when making this assumption as satellites may have non-rigid components that may very well affect the satellite's motion (for proof, look no further than the Explorer-1 satellite [85]). To simulate a satellite's dynamics, the curvilinear and rotational motion of the satellite as a result of the total force and torque acting on the satellite must be modeled; these models are shown in equations 3-27 and 3-28 respectively,

$$\vec{f}_{cm}^B(t) = m_s [\vec{\omega}_{IB}^B(t) \times \vec{v}_{cm}^B(t) + \dot{\vec{v}}_{cm}^B] \quad 3-27$$

where, on the left side of the equation \vec{f}_{cm}^B is the force vector in Newtons acting in the body fixed frame B whose origin is located at the COM of the rigid body. \vec{f}^B includes control and perturbation forces. On the right side of the equation $\vec{\omega}_{IB}^B$ is the angular velocity vector of the body in $\frac{\text{rad}}{\text{s}}$, \vec{v}_{cm}^B is the velocity of the body in m/s, and $\dot{\vec{v}}_{cm}^B$ is the body's acceleration in $\frac{m}{s^2}$. All velocities are with respect to an inertial frame of reference,

$$\vec{\tau}_{cm}^B(t) = \vec{\omega}_{IB}^B(t) \times J_B \vec{\omega}_{IB}^B(t) + J_B \dot{\vec{\omega}}_{IB}^B(t) \quad 3-28$$

where, on the left side of the equation $\vec{\tau}_{cm}^B$ is the torque vector in N-m acting in the B-frame at the COM and includes both control and perturbation torques acting on the satellite. On the right side of equation 3-28, J_B is the mass moment of inertia matrix in kg-m², and $\dot{\vec{\omega}}_{IB}^B$ is the angular acceleration of the body in $\frac{\text{rad}}{s^2}$.

These equations can be combined into the Newton-Euler equation shown in equation 3-29, which will be used as the dynamic model of the satellite for the thesis simulation,

$$\begin{bmatrix} \vec{f}^B \\ \vec{\tau}^B \end{bmatrix} = \begin{bmatrix} J_B & 0 \\ 0 & m_s I \end{bmatrix} \begin{bmatrix} \vec{\omega}_{IB}^B \\ \dot{\vec{v}}_{IB}^B \end{bmatrix} + \begin{bmatrix} S(\vec{\omega}_{IB}^B) & 0 \\ 0 & S(\vec{\omega}_{IB}^B) \end{bmatrix} \begin{bmatrix} J_B & 0 \\ 0 & m_s I \end{bmatrix} \begin{bmatrix} \vec{\omega}_{IB}^B \\ \dot{\vec{v}}_{IB}^B \end{bmatrix} \quad 3-29$$

where $S(\vec{\omega}_{IB}^B)$ represents the skew-symmetric matrix of $\vec{\omega}_{IB}^B$, which is a matrix multiplication representation of the cross product. I represents the 3x3 identity matrix and all other variables are as they were previously defined.

Equation 3-30 shows the external forces that are assumed to act on the satellite in the B-frame.

$$\vec{f}^B = \vec{f}_{EG}^B + \vec{f}_{SG}^B + \vec{f}_{LG}^B + \vec{f}_A^B + \vec{f}_{SP}^B \quad 3-30$$

Where \vec{f}_B is a three-element column vector representing the resultant force acting on the satellite's COM in the B-frame in Newtons. \vec{f}_{EG}^B is the gravitational force of Earth, \vec{f}_{SG}^B is the gravitational force of the sun, \vec{f}_{LG}^B is the lunar gravitational force, \vec{f}_A^B is the aerodynamic force, and \vec{f}_{SP}^B is the solar pressure force.

Equation 3-31 shows the external torques that are assumed to act on the satellite in the B-frame,

$$\vec{\tau}_B = \vec{T}_{GG}^B + \vec{T}_{SP}^B + \vec{T}_A^B + \vec{T}_M^B \quad 3-31$$

where $\vec{\tau}_B$ is a three element column vector representing the resultant torque acting about the satellites COM in the B-frame in N-m. \vec{T}_{GG}^B is the gravity gradient torque acting on the satellite as a result of Earth's gravity, \vec{T}_{SP}^B is the solar pressure torque, \vec{T}_A^B is the aerodynamic torque and \vec{T}_M^B is the residual magnetic torque. All the torques on the right side of equation 3-31 are described in detail later in this chapter.

3.3.2 Satellite Inertial and Geometric Properties

To simulate the dynamics of a satellite, as a result of applied forces and torques, understanding how the geometric and inertial properties are defined is essential. It is important for a user to understand how they are defined to correctly set up the simulation parameters.

The user is required to enter the satellite's mass in kg and the inertia matrix of the satellite with respect to the B-frame (whose origin is at the center of mass). These properties are simple to get using industry standard Computer Aided Design (CAD) software. It is important to note that when retrieving these values from a CAD package, the user should be careful to request the Inertia Tensor aligned to the B-frame coordinate system and located at the center of mass. The Inertia Tensor in the B-frame is given in equation 3-32 for reference.

$$J_B = \begin{bmatrix} J_{xx} & J_{xy} & J_{xz} \\ J_{yx} & J_{yy} & J_{yz} \\ J_{zx} & J_{zy} & J_{zz} \end{bmatrix} \quad 3-32$$

The Inertia Tensor can be further dissected into the Moments of Inertia, shown in equations 3-33, 3-34 and 3-35, and the Products of Inertia, shown in equations 3-36, 3-37 and 3-38,

$$J_{xx}^B = \iiint (y^2 + z^2)\rho(x, y, z)dx dy dz \quad 3-33$$

$$J_{yy}^B = \iiint (x^2 + z^2)\rho(x, y, z)dx dy dz \quad 3-34$$

$$J_{zz}^B = \iiint (x^2 + y^2)\rho(x, y, z)dx dy dz \quad 3-35$$

$$J_{xy}^B = J_{yx}^B = -\iiint xy \rho(x, y, z)dx dy dz \quad 3-36$$

$$J_{xz}^B = J_{zx}^B = -\iiint xz \rho(x, y, z)dx dy dz \quad 3-37$$

$$J_{yz}^B = J_{zy}^B = -\iiint yz \rho(x, y, z)dx dy dz \quad 3-38$$

where ρ is density in $\frac{kg}{m^3}$. The definition of the simulated satellite's geometric properties requires more time and careful attention. Each unique satellite will require the user to define the number of surfaces, the location of the vertices that make up the surfaces relative to the center of geometry (COGEO), the position vectors from the COGEO to the center of each surface, the area of each surface, the normal vector of each surface, and the COM. These values are then input into the initial configuration file along with the inertial properties prior to simulation. Figure 11 shows a schematic of a generic satellite's geometric properties.

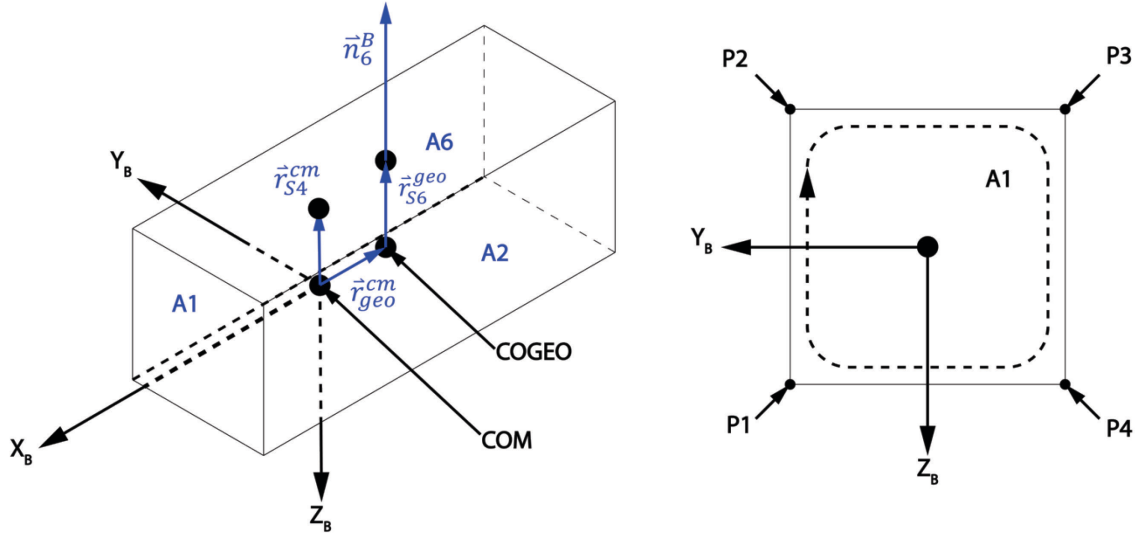


Figure 11: Geometric Properties of Simulated Satellite

3.4 Other Disturbance Forces and Torques

3.4.1 Earth Gravity Force and Gravity Gradient Torque

Gravitational attraction between a primary and a secondary body (e.g. the Earth and an orbiting satellite) is the dominant force behind orbital motion. Other forces (including gravity from third bodies, aerodynamic drag, and solar radiation pressure) and torques (including gravity gradient torque, aerodynamic torque, solar radiation pressure torque, and residual magnetic torque) cause perturbations to a body's orbital trajectory and attitude. The gravitational force of Earth acting on a satellite can be described simply using Newton's law of gravitation, where the Earth is modeled as a point mass, which is expressed in B-frame coordinates in equation 3-39 [42],

$$\vec{f}_{EG}^B = R_{IB}^T \left[-\frac{m_s \mu_e \vec{r}_{IB}^I}{\|\vec{r}_{IB}^I\|^3} \right] \quad 3-39$$

where \vec{f}_{EG}^B is the 3x1 vector representing the gravitational force of Earth in the B-frame in Newtons, R_{IB}^T is a rotation matrix to transform a vector from the I-frame to the B-frame, m_s is the satellite's mass in kg, μ_e is the gravitational parameter of Earth in $\frac{m^3}{s^2}$, and \vec{r}_{IB}^I is the position vector of the B-frame with respect to the I-frame in I-frame coordinates.

However, the Earth is not a perfect homogenous sphere. It is in fact asymmetric: it bulges at the equator; it is flattened at the poles; it has oceans which bulge due to the tidal forces of the sun and moon; and it is heterogenous [81]. As a result, the force of gravity is not uniform around the Earth. This results in the perturbation of an orbiting satellite's trajectory based on the inclination of a satellite's orbit, its altitude, and its eccentricity. These perturbations result in nodal precession (where the satellite's orbital plane rotates around Earth's axis of rotation) and apsidal rotation (the rotation of the argument of perigee about the orbital momentum vector). As a result, these perturbations are critical in the design and simulation of a satellite's dynamics. For example, a sun-synchronous orbit is a result of designing a satellite's orbital plane to precess at the same rate as Earth rotates around the sun [42].

To model the uneven mass distribution of Earth, the gravitational potential function, as shown in equation 3-40 [42], can be used. This is also known as a spherical harmonic model,

$$\begin{aligned} \phi^E(\vec{r}) = \frac{\mu_e}{\|\vec{r}_{EB}^E\|} & \left[\sum_{n=2}^{\infty} J_n \left(\frac{r_e}{\|\vec{r}_{EB}^E\|} \right)^n P_n(\sin(\delta)) \right. \\ & \left. + \sum_{n=2}^{\infty} \sum_{m=1}^n \left(\frac{r_e}{\|\vec{r}_{EB}^E\|} \right)^n P_{n,m}(\sin(\delta)) [C_{n,m} \cos(m\lambda) + S_{n,m} \sin(m\lambda)] \right] \end{aligned} \quad 3-40$$

where $\phi^E(\vec{r})$ is the gravity potential, μ_e is the gravitational parameter of Earth in $\frac{m^3}{s^2}$, \vec{r}_{EB}^E is the 3X1 position vector of the satellite relative to the E-frame in E-frame coordinates in meters, P_n and $P_{n,m}$ are Legendre polynomials, δ is the latitude in degrees and λ is the longitude in degrees. The constant J_n represents the zonal harmonics which characterize the north-south mass distribution independent of longitude while the constants $C_{n,m}$ and $S_{n,m}$ are the tesseral harmonics which are a function of both latitude and longitude. These constants are obtained from satellite measurements, with the latest set coming from the Earth Gravitational Model 2008 (EGM2008) [86].

The gravitational potential function can then be used to determine the gravitational force experienced by an orbiting satellite as a function of its position as per equation 3-41[42],

$$\vec{f}_{EG}^B = R_{IB}^T R_{EI}^T m_s \vec{\nabla} \phi(\vec{r}_{EB}^E) \quad 3-41$$

where R_{IB}^T represents the rotation matrix describing the orientation of the I-frame with respect to the B-frame and R_{EI} represents the rotation matrix describing the orientation of the I-frame with respect to the E-frame.

The gravitational force of Earth may also cause a torque to act on a satellite because of the gravitational force decreasing quadratically with distance from the center of the Earth. As a result, the center of gravity (COG) does not coincide with the COM and causes a torque to act around the COM. The gravity gradient torque causes an orbiting body's minor principal axis of inertia to align itself with the gravity field vector. [42], [46]

Equation 3-42 [42] describes the gravity gradient torque acting on a satellite in the B-frame. The gravity gradient torque is first calculated in the I-frame, and then transformed into the B-frame using R_{IB}^T the transpose of the rotation matrix describing the orientation of the B-frame with respect to the I-frame.

$$\vec{T}_{gg}^B = R_{IB}^T \left[\frac{3\mu_e}{\|\vec{r}_{IB}^I\|^5} \vec{r}_{IB}^I \times \mathbf{J}_B \vec{r}_{IB}^I \right] \quad 3-42$$

3.4.2 Aerodynamic Disturbance Force and Torque

Past the Karmin line (~100 km), the atmosphere becomes rarefied to the point where the continuum assumption for fluid mechanics no longer applies, and instead the aerodynamics of spacecraft must be modeled with free molecular flow [68]. In this environment, atmospheric molecules can travel far before colliding with each other, and have a random thermal motion. When analyzing satellite drag in this environment, the momentum exchange between the molecules and the surface of the spacecraft is considered. Using the derivation found in [42], which assumes that the molecules impacting the spacecraft surface stick to the surface, that the random thermal motion of atmospheric molecules is much smaller than the velocity of the spacecraft, and that the spacecraft is not spinning results in the expression shown in equation 3-43 [42],

$$\vec{f}_A = -\rho \|\vec{v}_f\|^2 \hat{v}_f \int_{S_{WA}} (\vec{n} \cdot \hat{v}_f) dS \quad 3-43$$

where \vec{f}_A is the aerodynamic force vector in Newtons, ρ is the atmospheric density in $\frac{\text{kg}}{\text{m}^3}$, \vec{v}_f is the fluid velocity vector in $\frac{\text{m}}{\text{s}}$, S_{WA} is the wetted surface area in m^2 and \vec{n} is the surface normal vector. The aerodynamic force is a function of the square of the magnitude of the fluid velocity vector, which is due to two factors. First, the momentum exchange between the surface and the atmospheric particles is proportional to the mass of particles impacting the surface and the fluid velocity. Second, the total mass of particles impacting an infinitesimally small surface area on the satellite at any given time is proportional to the atmospheric free stream velocity. [42]

The free stream velocity of the atmosphere relative to the satellite is a function of satellite velocity, the rotation of Earth's atmosphere, upper atmospheric winds, and the random thermal motion of the atmosphere. For this thesis, it is assumed that the upper atmospheric winds are negligible compared to the velocity of the satellite and the rotation of the atmosphere. Also, it is assumed that the flow regime is hyperthermal as opposed to hypothermal because of the much greater velocity of the satellite compared to random thermal motion. [68] has an excellent description of the flow regime for spacecraft altitudes. From these assumptions, the free stream velocity vector can be defined by equation 3-44[10],

$$\vec{v}_f^B = R_{IB}^T \left[-\vec{v}_{IB}^I - R_{IE} \left(\omega_E \times \begin{bmatrix} r_x^E \\ r_y^E \\ 0 \end{bmatrix} \right) \right] \quad 3-44$$

where \vec{v}_f^B is the free stream velocity vector of the rarefied atmosphere in the B-frame in $\frac{\text{m}}{\text{s}}$, R_{IB}^T is the rotation matrix describing the orientation of the I-frame with respect to the B-frame, \vec{v}_{IB}^I is the velocity of the satellite relative to the I-frame in I-frame coordinates in $\frac{\text{m}}{\text{s}}$, R_{IE} is the rotation matrix describing the orientation of the E-frame with respect to the I-frame, ω_E is the rotational velocity of the Earth in $\frac{\text{rad}}{\text{s}}$, and both r_x^E and r_y^E is the x and y components of the satellite's position in E-frame coordinates.

While equation 3-43 does describe the aerodynamic force acting on a satellite, it is simplified. What is missing is a description of how the atmospheric molecules interact with the satellite's surface. For terrestrial applications, this is typically captured in the aerodynamic lift and

drag coefficients, which are also used for first order approximations of satellite drag (typically a C_D of 2.2 is used [46]). To obtain a better description of the aerodynamic force experienced by a satellite, the interactions between the satellite's surfaces and the atmospheric molecules must be captured.

The interaction between the surface of the satellite and the molecules in the atmosphere can be described by three types of interactions. The first type is called accommodation, which is shown in Figure 12. During this interaction, incident gas molecules are completely absorbed by the surface, resulting in the momentum of these molecules being completely transferred to the surface. [10], [42], [68].

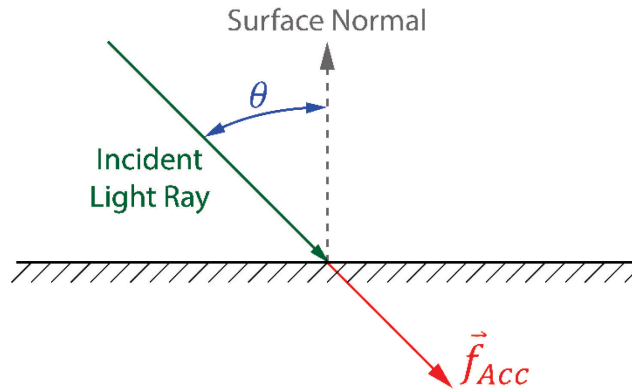


Figure 12: Accommodation/Absorption [42], [68]

The contribution to the aerodynamic force from the absorption of atmospheric molecules is described equation 3-45[10], [42],

$$\vec{f}_{Acc}^B = \sigma_A \rho \|\vec{v}_f^B\|^2 \sum_{n=1}^N H(\vec{n}_n^B \cdot \hat{v}_f^B) A_n \quad 3-45$$

where \vec{f}_{Acc}^B is a 3X1 vector in the B-frame representing the contribution from accommodation in Newtons, and ρ is the atmospheric density. σ_A is the unitless accommodation coefficient, which is typically anywhere between 0.8 and 1.0 for spacecraft [53], and defines how much of the aerodynamic force is due to accommodation versus specular reflection. $H(\vec{n}_n^B \cdot \hat{v}_f^B) A_n$ is the Heaviside function (reversed from the normal definition), described in equation 3-46[42] below, which calculates the surface area normal to the free stream velocity for each surface which is not shadowed,

$$H(\vec{n}_n^B \cdot \hat{v}_f^B)A_n = \begin{cases} (\vec{n}_n^B \cdot \hat{v}_f^B)A_n & (\vec{n}_n^B \cdot \hat{v}_f^B) < 0 \\ 0 & (\vec{n}_n^B \cdot \hat{v}_f^B) \geq 0 \end{cases} \quad 3-46$$

where \vec{n}_n^B is the surface normal vector of a surface n in B-frame coordinates, \hat{v}_f^B is the unit free stream velocity vector in B-frame coordinates, and A_n is the surface area of surface n .

The second type of surface interaction is called specular reflection and is shown in Figure 13 below. During this type of surface interaction, the atmospheric particles incident on a surface with angle θ relative to the surface normal are reflected at the same angle. As a result, twice the momentum is transferred to the surface compared to the first type of surface interaction resulting in the force vector pointing in the direction of the anti-surface normal [42], [68].

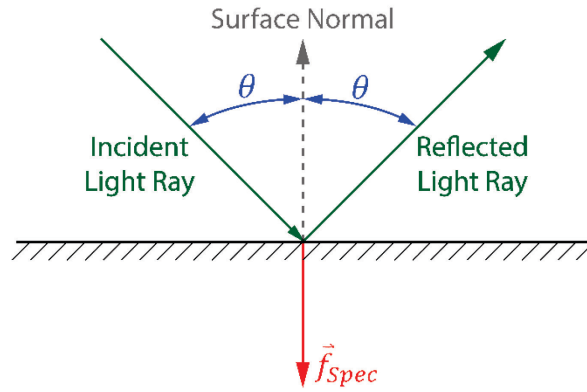


Figure 13: Specular Reflection [42], [68]

The contribution to the aerodynamic force from the specular reflection of atmospheric molecules is described by equation 3-47[10],

$$\vec{f}_{Spec}^B = 2(1 - \sigma_A)\rho \|\vec{v}_f^B\|^2 \sum_{n=1}^N \vec{n}_n^B H(\vec{n}_n^B \cdot \hat{v}_f^B)A_n \quad 3-47$$

where \vec{f}_{Spec}^B is a 3X1 vector in the B-frame representing the contribution from specular reflection in Newtons.

The third type of surface interaction is called diffuse reflection and is shown in Figure 14 below. During this type of surface interaction, the atmospheric particles absorbed by the surface accommodate to the temperature of the surface and are then diffusely emitted following the Knudsen cosine law distribution [68]. The resultant force is in the direction anti-normal to the

surface, however, because of the distribution only a small percentage of momentum is in the direction of the anti-normal. [10], [42], [68]

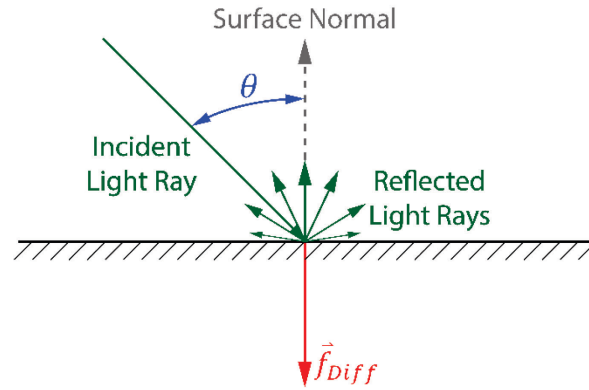


Figure 14: Diffuse Reflection [42], [68]

The contribution to the aerodynamic force from the diffuse reflection of atmospheric molecules is described by equation 3-48,

$$\vec{f}_{Diff}^B = \sigma_A \rho \|\vec{v}_f^B\| \|\vec{v}_b^B\| \sum_{n=1}^N \vec{n}_n^B H(\vec{n}_n^B \cdot \hat{v}_f^B) A_n \quad 3-48$$

where \vec{f}_{Diff}^B is a 3X1 vector in the B-frame representing the contribution from diffuse reflection in Newtons, and \vec{v}_b^B represents the velocity of the diffusely reflected particles normal to the surface (typically 5% of \vec{v}_f^B).

Summing these forces together results in the total aerodynamic disturbance force imparted to the satellite, as shown in equation 3-49.

$$\vec{f}_A^B = \vec{f}_{Acc}^B + \vec{f}_{Spec}^B + \vec{f}_{Diff}^B \quad 3-49$$

The aerodynamic force acts on a satellite at the point known as the center of pressure (COP). Around this point, no aerodynamic torque is generated. However, unless the COP is also located at the COM of the satellite, an aerodynamic torque will be exerted on the satellite. To calculate the aerodynamic torque, the COP in the B-frame must be known. This can be found through equation 3-50[42],

$$\vec{c}_{PA}^B = \frac{\sum_{n=1}^N \vec{r}_{Sn}^{cm} (\vec{n}_n^B \cdot \hat{v}_f^B) A_n}{\sum_{n=1}^N (\vec{n}_n^B \cdot \hat{v}_f^B) A_n} \quad 3-50$$

where \vec{c}_{PA}^B is the 3X1 position between the COM and the COP in the B-frame. Note that the COP is a quantity that varies with attitude.

Finally, equation 3-51 can be used to calculate the aerodynamic torque in the B-frame.

$$\vec{T}_A^B = \vec{c}_{PA}^B \times \vec{f}_A^B \quad 3-51$$

In case the COP is calculated with respect to the COGEO instead of the COM (which is useful for simple geometric satellites such as CubeSats), then equation 3-52 is useful in the calculation of the position vector of the COP of a surface relative to the satellite's COM.

$$\vec{r}_{Sn}^{cm} = \vec{r}_{Sn}^{geo} - \vec{r}_{cm}^{geo} \quad 3-52$$

3.4.3 Solar Pressure Force and Torque

Solar radiation pressure is caused by the transfer of momentum between photons emitted by the sun and satellite surfaces. Generally, forces and torques produced by solar pressure tend to be smaller for satellites in LEO, except for solar torques produced by a long moment arm. Solar pressure begins to dominate at higher altitudes when gravity gradient, residual magnetic, and aerodynamic disturbances become insignificant due to their dependence on distance from Earth. However, solar pressure also depends on the satellite's distance from the sun, which changes depending on the day of the year. This is captured in the solar irradiance calculation in equation 3-53 [87],

$$I_S = \frac{3.823 \times 10^{26} W}{4\pi \|\vec{r}_{IS}^I - \vec{r}_{IB}^I\|^2} \quad 3-53$$

where I_S is the solar irradiance in Watts and \vec{r}_{IS}^I is the 3X1 position vector from the center of the I-frame to the center of the sun in I-frame coordinates. Solar irradiance can then be used to calculate the solar pressure at the satellite's location in space using equation 3-54,

$$P_{SP} = \frac{I_S}{c} \quad 3-54$$

where P_{SP} is the solar pressure in $\frac{N}{m^2}$ and c is the speed of light in a vacuum.

When a spacecraft is subject to solar radiation pressure, the solar pressure force and torque applied to the spacecraft will depend on both the attitude of the satellite and its surface properties. The attitude of the satellite determines which faces are in sunlight and which are not, the total surface area normal to the solar vector, and the location of the center of solar pressure relative to the COM. The surface properties of the satellite determine how much sunlight is absorbed by the surface and reflected by the surface, which affect the exchange of momentum between the spacecraft and the photons. Equation 3-55 describes the contribution to the total solar pressure force from the absorption of photons,

$$\vec{f}_{Abs}^B = (1 - \sigma_{Spec}) P_{SP} \hat{r}_{BS}^B \sum_{n=1}^N H(\vec{n}_n^B \cdot \hat{r}_{BS}^B) A_n \quad 3-55$$

where \vec{f}_{Abs}^B is the 3X1 vector representing the contribution from solar absorption to the solar pressure force in the B-frame in Newtons, σ_{Spec} is the unitless specular reflection coefficient and \hat{r}_{BS}^B is the 3X1 position unit vector pointing from the B-frame to the center of the sun in B-frame coordinates. $H(\vec{n}_n^B \cdot \hat{r}_{BS}^B) A_n$ (reversed from the normal definition) is the Heaviside function which calculates the surface area of a sunlit face normal to the solar vector and is described in equation 3-56 [88],

$$H(\vec{n}_n^B \cdot \hat{r}_{BS}^B) A_n = \begin{cases} (\vec{n}_n^B \cdot \hat{r}_{BS}^B) A_n & (\vec{n}_n^B \cdot \hat{r}_{BS}^B) < 0 \\ 0 & (\vec{n}_n^B \cdot \hat{r}_{BS}^B) \geq 0 \end{cases} \quad 3-56$$

where \vec{n}_n^B is the surface normal vector of a surface n in B-frame coordinates, \hat{r}_{BS}^B is the unit position vector of the sun relative to the satellite in B-frame coordinates, and A_n is the surface area of surface n .

The reflection of photons can be further subdivided into two different effects, specular and diffuse reflection which are defined in equations 3-57 and 3-58 [88] respectively. For solar pressure, the contribution to the total solar pressure force from specular reflection is described by equation 3-57[88],

$$\vec{f}_{SR}^B = 2\sigma_{Spec} P_{SP} \vec{n}_n^B \sum_{n=1}^N H(\vec{n}_n^B \cdot \hat{r}_{BS}^B) A_n \quad 3-57$$

where \vec{f}_{SR}^B is the 3X1 vector representing the contribution from specular reflection of photons to the solar pressure force in the B-frame in Newtons.

Equation 3-58 describes the contribution to total solar pressure force from diffuse reflection,

$$\vec{f}_{DR}^B = \frac{2}{3} \sigma_{Diff} P_{SP} \vec{n}_n^B \sum_{n=1}^N H(\vec{n}_n^B \cdot \hat{r}_{BS}^B) A_n \quad 3-58$$

where \vec{f}_{DR}^B is the 3X1 vector representing the contribution from diffuse reflection of photons to the solar pressure force in the B-frame in Newtons and σ_{Diff} is the diffuse reflection coefficient. Equation 3-59 [88] represents the relationship between the coefficients, which sum to unity,

$$1 = \sigma_{Abs} + \sigma_{Spec} + \sigma_{Diff} \quad 3-59$$

where σ_{Abs} is the absorption coefficient.

The solar pressure force can be described with equation 3-60[88],

$$\vec{f}_{SP}^B = \vec{f}_{Abs}^B + \vec{f}_{SR}^B + \vec{f}_{DR}^B \quad 3-60$$

where \vec{f}_{SP}^B represents the 3X1 solar pressure force vector in the B-frame in Newtons.

Like the aerodynamic force, the solar pressure force acting on a satellite acts at the point known as the center of solar pressure. Around this point, no torque from solar pressure is generated. However, unless the center of solar pressure is also located at the COM of the satellite, a solar pressure torque will be exerted on the satellite. To calculate the solar pressure torque, the center of solar pressure in the B-frame must be known. This can be found through equation 3-61[42],

$$\vec{c}_{SP}^B = \frac{\sum_{n=1}^N \vec{r}_{Sn}^{cm} (\vec{n}_n^B \cdot \hat{r}_{BS}^B) A_n}{\sum_{n=1}^N (\vec{n}_n^B \cdot \hat{r}_{BS}^B) A_n} \quad 3-61$$

where \vec{c}_{SP}^B represents the 3X1 center of solar pressure vector in the B-frame in meters. Note that the center of solar pressure is attitude dependent.

Finally, the solar pressure torque can be found with equation 3-62[42].

$$\vec{T}_{SP}^B = \vec{c}_{SP}^B \times \vec{f}_{SP}^B \quad 3-62$$

where \vec{T}_{SP}^B is the solar pressure torque in the B-frame in Nm.

Solar pressure only acts on a satellite during the sunlit phase of its orbit, and so goes to zero during eclipse. Equation 3-63 shows the eclipse condition that can be applied to the solar pressure force assuming that the shadow of Earth can be modeled by a cylinder as shown in Figure 15. This assumption is based on the near instantaneous transition through penumbra, the twilight condition between full sunlight and Earth's shadow (umbra),

$$\vec{f}_{SP}^B = \begin{cases} 0 & , -(\hat{r}_{IS}^I \cdot \hat{r}_{IB}^I) \geq \cos\left(\frac{\pi}{2} - \cos^{-1}\left(\frac{r_e}{\|\hat{r}_{IB}^I\|}\right)\right) \\ \vec{f}_{Abs}^B + \vec{f}_{SR}^B + \vec{f}_{DR}^B & , -(\hat{r}_{IS}^I \cdot \hat{r}_{IB}^I) \geq \cos\left(\frac{\pi}{2} - \cos^{-1}\left(\frac{r_e}{\|\hat{r}_{IB}^I\|}\right)\right) \end{cases} \quad 3-63$$

where r_e is Earth's equatorial radius in meters.

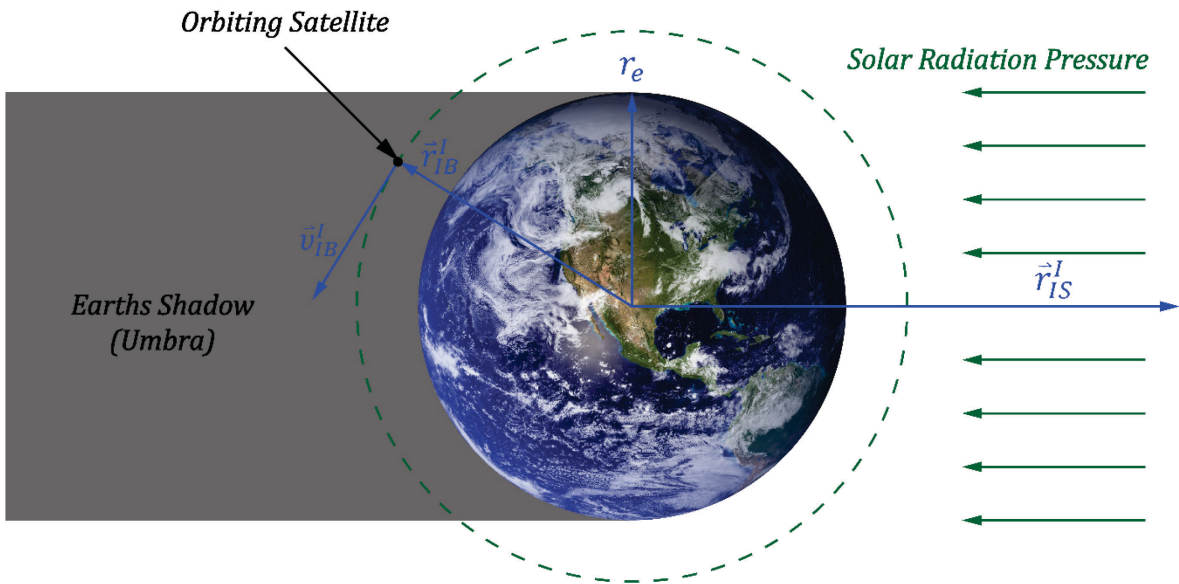


Figure 15: Satellite in Eclipse (photocredit: NASA[89])

3.4.4 Residual Magnetic Torque

Spacecraft orbiting Earth tend to have magnetized components (e.g. electric motors) or have some residual magnetic field which interacts with Earth's magnetic field to create a torque on the spacecraft. This torque, shown in equation 3-64 [42], works on the spacecraft to align its magnetic field with that of the Earth's, much like a compass needle,

$$\vec{T}_M^B = \vec{A}^B \times [R_{IB}^T \vec{B}^I] \quad 3-64$$

where \vec{A}^B is a three-element column vector representing the residual magnetic dipole moment of the satellite in the B-frame in Am^2 and \vec{B}^I is a three-element column vector representing the magnetic field strength in the I-frame in nT.

3.4.5 Solar and Lunar Gravity Force

The force of gravity from the sun and the moon on a satellite orbiting Earth (third body forces) augment the effect of a non-spherical Earth by contributing to nodal precession and apsidal rotation of a satellite's orbit, although the effect due to the non-spherical Earth dominates. Equations 3-65 and 3-66 represent the forces acting on the satellite from the sun and moon respectively. Derivations for third body forces can be found in [42],

$$\vec{f}_{SG}^B = R_{IB}^T \left[\mu_S m_s \left(\frac{\vec{r}_{BS}^I}{\|\vec{r}_{BS}^I\|^3} - \frac{\vec{r}_{IS}^I}{\|\vec{r}_{IS}^I\|^3} \right) \right] \quad 3-65$$

where \vec{f}_{SG}^B represents the 3X1 solar gravity force vector acting on the satellite in the B-frame in Newtons and μ_S is Sol's gravitational parameter,

$$\vec{f}_{LG}^B = R_{IB}^T \left[\mu_L m_s \left(\frac{\vec{r}_{BL}^I}{\|\vec{r}_{BL}^I\|^3} - \frac{\vec{r}_{IL}^I}{\|\vec{r}_{IL}^I\|^3} \right) \right] \quad 3-66$$

where \vec{f}_{LG}^B represents the 3X1 lunar gravity force vector acting on the satellite in the B-frame in Newtons, μ_L is the moon's gravitational parameter, \vec{r}_{BL}^I is the 3X1 position vector from the center of the satellite to the center of the moon in the I-frame in meters, and \vec{r}_{IL}^I is the 3X1 position vector from the center of the Earth to the center of the moon in the I-frame in meters.

3.5 Summary

This chapter defined the coordinate systems and transformations used in this thesis and the simulation and reviewed orbit propagation methods. Then, the dynamics of a rigid satellite in orbit were presented, along with the inertial and geometric properties of the satellite. Finally, the mathematical formulation of the disturbance forces and torques acting on the satellite were defined.

4 Simulation Design

4.1 Simulation Overview

OrbSim is a program created to simulate spacecraft dynamics in six degrees of freedom. It is intended for space mission analysis and design, as well as attitude and orbit determination, and control system design. OrbSim was created in MATLAB/Simulink. Specifically, MATLAB is used for creating the graphical user interface (GUI), where the user inputs simulation parameters, controls the simulation, and analyzes data. Simulink is the tool used as the simulation environment. The GUI was created using GUIDE, while the Simulink model was created using general blocks, blocks from the Aerospace Toolbox, and blocks from Simscape Multi-body. Underlying the simulation is a library of self-created MATLAB functions and Simulink blocks used throughout the Simulink model and the GUI.

Table 5 shows the features of OrbSim, using the same simulation features examined in Chapter 2, in comparison to STK [27], ASTOS [28], and SCT [29]. In addition to these features, OrbSim is modeled using EGM2008 [86] for the gravity field; geodetic coordinates are modeled using WGS84 [90], and IGRF-12 [91] is used to model the Earth's magnetic field. The simulation uses the ICRS, ITRF, and the J2000 epoch [79] for the specification of the I-frame and the E-frame (and includes both observed and predicted EOP obtained from Celestrak [80]). Solar perturbation force and torque are modeled as a function of spacecraft attitude and surface properties (using the same panel method as for aerodynamics), and uses the Jet Propulsion Laboratory Development Ephemeris 432t [92] for the position of the sun and moon (which is also used for third body gravity). The NRLMSISE-00 atmospheric model is used for atmospheric density modeling. Predicted and observed space weather parameters, specifically F10.7 and three hour A_p (non interpolated), is obtained from Celestrak[80]. Finally, the Simulink environment provides a number of fixed and variable step integrators and provides absolute and relative tolerance for integration down to 10^{-12} .

Table 5: Features of OrbSim Compared with Other Astrodynamics Softwares

Software		STK [27]	ASTOS [28]	SCT [29]	OrbSim
License		C	C	C	A
Forces	Gravity - Point Mass	X	X	X	X
	Gravity – Higher Order	X	X	X	X
	Solar Radiation Pressure	X	X	X	X
	Aero	X	X	X	X
	Third Body	X	X	X	X
Torques	GG	X	X	X	X
	SRP	X	X	X	X
	Residual Magnetic	X	X	X	X
	Aero	X	X	X	X
Aerodynamic Modelling	Simplified	X	X	X	X
	Panel Method	X	X		X
	Ray Tracing / Line Scan Method			X	
	DMCS				
Atmospheric Models	Exponential	X		X	
	NRLMSISE-00	X	X		X
	Jacchia Bowman 2006/2008		X		
	Other	X	X	X	

4.2 Simulation Architecture

OrbSim is created using MATLAB/Simulink with the addition of the Aerospace Toolbox and Simscape Multi-Body Toolbox. OrbSim consists of a GUI created in MATLAB using GUIDE, the InitConfig.mat configuration file, the simulation environment in Simulink, the SimData.mat data file created by Simulink, and a library of MATLAB functions and Simulink blocks created for spacecraft. Figure 16 shows the high-level architecture of OrbSim.

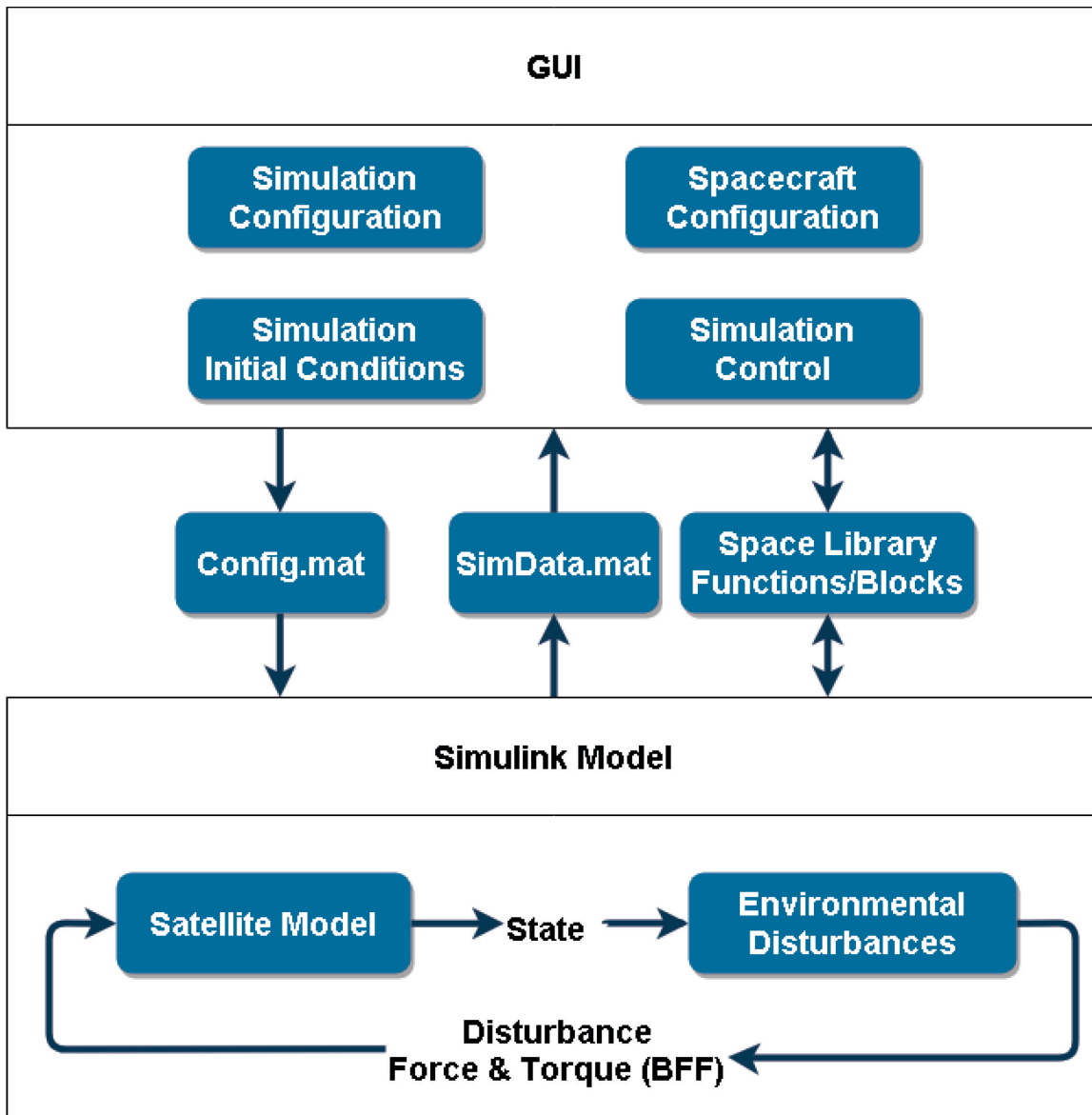


Figure 16: OrbSim High Level Architecture

4.2.1 The GUI

The GUI, shown in Figure 17, is the primary method for which the user creates, edits, and runs simulations. Upon starting OrbSim, the GUI runs an opening script which loads the InitConfig.mat file, opens the Simulink model, downloads space weather data (1957/10/01 – present), and EOP date (1962/01/01 – present) from Celestrack [80], updates and saves the InitConfig file, renames InitConfig to Config, creates and positions the GUI and output figures, and finally, passes the Config variable into the GUI handle structure. Following this, the user can begin defining the simulation. Using the GUI, the user can specify initial conditions for the

satellite, decide which perturbations to use for astrodynamics modelling, define the properties of the spacecraft and control the simulation.

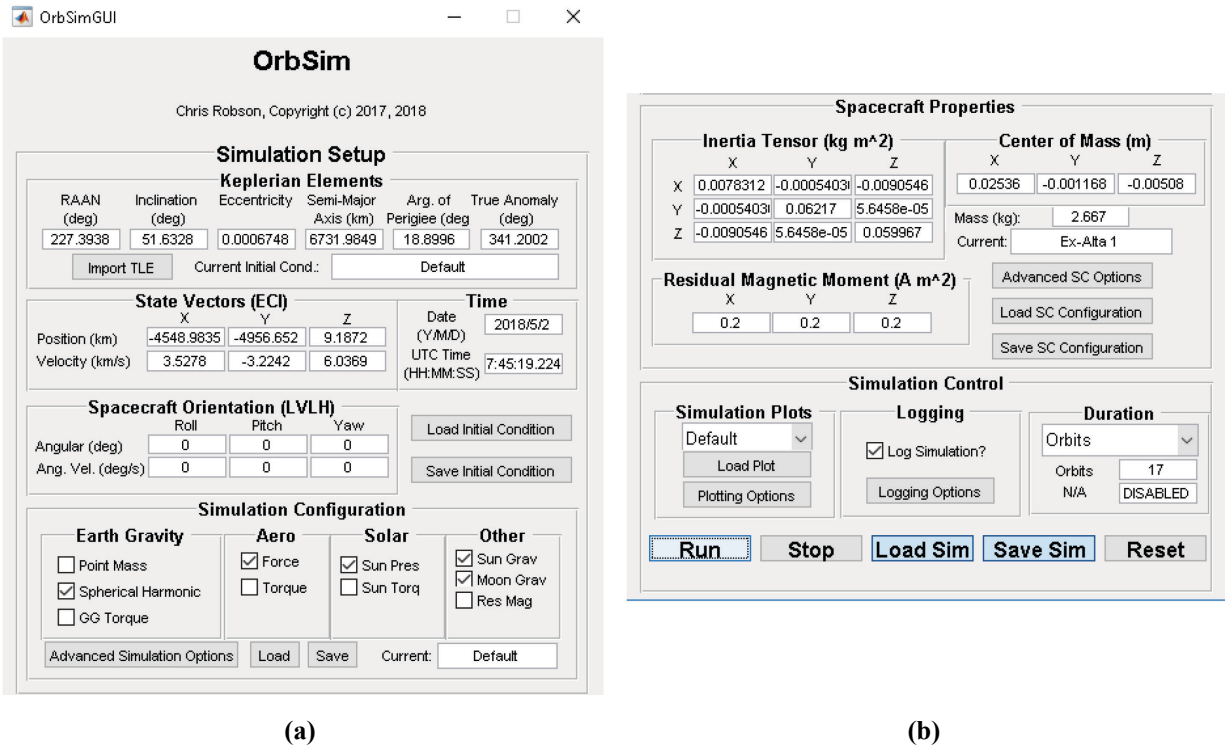


Figure 17: OrbSim GUI (a) Top Portion (b) Bottom Portion

Initial Conditions, the first subset of the Simulation Setup section, can be specified either as Keplerian Elements, state vectors (in the I-frame), or by loading a TLE (which updates the Keplerian Elements). Upon updating the Keplerian Elements, the state vectors are automatically updated (and vice versa). Additionally, spacecraft attitude and angular velocity relative to the O-frame can be specified, and the date and time (in UTC) can be specified (automatically calculated when importing a TLE as the orbit epoch). Finally, the user can save initial conditions from the current simulation, load initial conditions from a previous simulation and name the current initial condition configuration.

Simulation Configuration, the second subset of the Simulation Setup section, is used to define which perturbation forces and torques act on the satellite. These include point mass or spherical harmonic gravity (you cannot have both at the same time), gravity gradient torque, aerodynamic force and torque, solar radiation pressure force and torque, solar gravity, lunar gravity, and residual magnetic torque. In addition, the user may load, save, and name a simulation

configuration. The Advanced Simulation Options is currently a placeholder for future development. The Advanced Simulation Options section is intended to allow the user to choose aerodynamic and solar radiation pressure models, define the details of environmental model, and define the satellite control configuration. Currently, these parameters (except for control configuration) must be set in Simulink.

The Spacecraft Properties section allows the user to define the spacecrafts mass, inertia tensor, center of mass, and residual magnetic moment. Additionally, like with the other sections, the user may also load, save or name a spacecraft configuration. The Advanced SC Options button is currently a placeholder for future development. The intention is to allow users to import STL files, run a program to define the STL file's geometric properties or to build a custom spacecraft by defining geometric properties.

The Simulation Control section allows the user to run the simulation, stop the simulation, save and load previous simulation configurations (which include the configurations of the initial conditions configuration, spacecraft configuration and spacecraft configuration), and reset the simulation to the default configuration. Additionally, the user can define the duration of the simulation (currently only by defining the number of orbits). Options that are reserved for future development include plotting and data logging. Currently, these functionalities are manual.

4.2.2 *InitConfig.mat / Config.mat*

The InitConfig.mat file is the default configuration structure loaded by OrbSim, and Config.mat is the configuration structure which handles and passes data while OrbSim is running. Upon starting, InitConfig.mat passes its data on to Config.mat. Figure 18 shows how the InitConfig.mat file is structured. Table 6, Table 7, Table 8, Table 9, and Table 10 provide a description, the class, the size, the value, and the units of each variable stored in the InitConfig structure, the Spacecraft structure, the OrbSimIC structure, the Constants structure, and the SimParam structure, respectively.

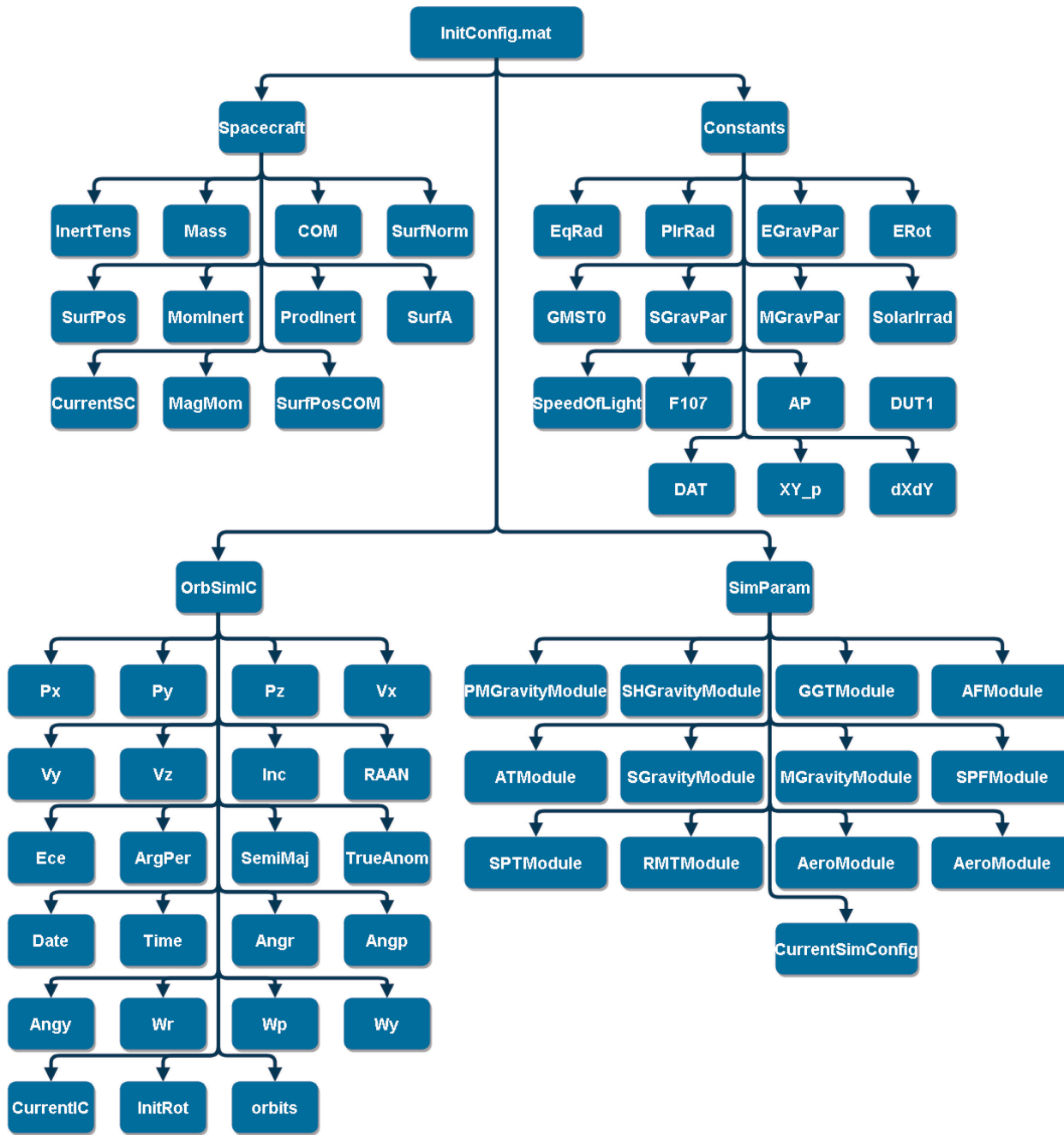


Figure 18: Organization of Structure Variable InitConfig.mat

Table 6: First Level of the InitConfig.mat Structure

Name	Description	Class	Size	Value	Units
Spacecraft	Structure which defines the configuration of the simulated spacecraft.	struct	1X1	N/A	N/A
OrbSimIC	Structure which defines the initial conditions for the simulation.	struct	1X1	N/A	N/A
Constants	Structure which defines the constants used in the simulation.	struct	1X1	N/A	N/A
SimParam	Structure which defines the perturbation modules to use for propagation.	struct	1X1	N/A	N/A

Table 7: Breakdown of the Spacecraft Branch in the InitConfig.mat Structure

Name	Description	Class	Size	Value	Units
InertTens	Satellite inertia tensor located at the center of mass in the BFF	double	3X3	User Defined	kg-m ²
Mass	Satellite mass.	double	1X1	User Defined	kg
COM	Satellite center of mass (COM) vector with respect to the geometric center in the BFF.	double	1X3	User Defined	m
SurfNorm	Unit vectors defining the normal direction to each spacecraft external surface in the BFF.	double	NX3	User Defined	Unitless
SurfPos	Position vector of each spacecraft external surface with respect to the geometric center in the BFF.	double	3XN	User Defined	m
MomInert	Satellite moment of inertia tensor located at the COM in the BFF.	double	1X3	User Defined	kg-m ²
ProdInert	Satellite product of inertia tensor located at the COM in the BFF.	double	1X3	User Defined	kg-m ²
SurfA	Surface area of satellite external surfaces.	double	1XN	User Defined	m ²
CurrentSC	Name of the current spacecraft being modeled.	Char	N/A	User Defined	N/A
MagMom	Residual magnetic moment vector of the satellite in the BFF.	double	1X3	User Defined	A-m ²
SurfPosCOM	Position vector of each spacecraft external surface with respect to the COM in the BFF.	double	3XN	User Defined	m

Table 8: Breakdown of the OrbSimIC Branch in the InitConfig.mat Structure

Name	Description	Class	Size	Value	Units
Px	X-component of the satellite position in ECI.	double	1X1	User Defined	m
Py	Y-component of the satellite position in ECI.	double	1X1	User Defined	m
Pz	Z-component of the satellite position in ECI.	double	1X1	User Defined	m
Vx	X-component of the satellite velocity in ECI.	double	1X1	User Defined	m/s
Vy	Y-component of the satellite velocity in ECI.	double	1X1	User Defined	m/s
Vz	Z-component of the satellite velocity in ECI.	double	1X1	User Defined	m/s
Inc	Inclination of the satellites orbit.	double	1X1	User Defined	deg
RAAN	Right ascension of ascending node of the satellites orbit.	double	1X1	User Defined	deg
Ece	Orbit eccentricity of the satellites orbit.	double	1X1	User Defined	Unitless
ArgPer	Argument of perigee of the satellites orbit.	double	1X1	User Defined	deg
SemiMaj	Semi-major axis of the satellites orbit.	double	1X1	User Defined	m
TrueAnom	True anomaly of the satellites orbit.	double	1X1	User Defined	deg
Date	Epoch date.	double	1X3	User Defined	YY/MM/DD
Time	Epoch time in UTC.	double	1X3	User Defined	HH:DD:SS
Angr	Roll angle of the BFF with respect to the LVLH frame.	double	1X1	User Defined	deg
Angp	Pitch angle of the BFF with respect to the LVLH frame.	double	1X1	User Defined	deg
Angy	Yaw angle of the BFF with respect to the LVLH frame.	double	1X1	User Defined	deg
Wr	Roll angular velocity of the BFF with respect to the LVLH frame.	double	1X1	User Defined	deg/s
Wp	Pitch angular velocity of the BFF with respect to the LVLH frame.	double	1X1	User Defined	deg/s
Wy	Yaw angular velocity of the BFF with respect to the LVLH frame.	double	1X1	User Defined	deg/s
CurrentIC	Name of the current spacecraft initial conditions being modeled.	char	N/A	User Defined	deg/s
InitRot	Initial rotation matrix of the satellite.	double	3X3	User Defined	Unitless
orbits	Number of orbits to simulate.	double	1X1	User Defined	Unitless

Table 9: Breakdown of the Constants Branch in the InitConfig.mat Structure

Name	Description	Class	Size	Value	Units
EqRad	Earth's equatorial radius.	double	1X1	6.378E+06	m
PlrRad	Earth's polar radius.	double	1X1	6.357E+06	m
EGravPar	Gravitational parameter of Earth.	double	1X1	3.986E+14	m ³ /s ²
Erot	Earth's rotation rate.	double	1X1	7.292E-05	rad/s
GMST0	Greenwich mean sidereal time at J2000 epoch.	double	1X1	4.895E+00	rad
SGravPar	Gravitational parameter of Sol.	double	1X1	1.327E+20	m ³ /s ²
MgravPar	Gravitational parameter of the Moon.	double	1X1	4.903E+12	m ³ /s ²
SolarIrrad	Total solar output.	double	1X1	3.823E+26	W
SpeedOfLight	Speed of light in a vacuum	double	1X1	2.998E+08	m/s
	Matrix defining daily F10.7 index information since 1957/10/01 with dates in Modified Julian Date (MJD):				
F107	[MJD, daily F10.7 index, 81-day centered F10.7 index, last 81-day F10.7 index]	double	MX4	N/A	N/A
	Updated from Celestrak.com during simulation opening sequence. Matrix defining the A _p geomagnetic index information every three hours since 1957/10/01 00:00:00 with dates/time in MJD.				
AP	[MJD, Daily AP, current 3 hour AP, AP from 3 hours previous, AP from 6 hours previous, AP from 9 hours previous, AP from 12 hours previous, AP from 12 - 33 hours previous, AP from 36 - 57 hours previous]	double	MX8	N/A	N/A
	Updated from Celestrak.com during simulation opening sequence. [MJD, DUT1]				
DUT1	Difference between Universal Coordinated Time and Universal Time.	double	MX2	N/A	s
	[MJD, DAT]				
DAT	Difference between International Atomic Time and Universal Coordinated Time.	double	MX2	N/A	s
XY_p	Polar displacement of the Earth.	double	MX3	N/A	rad
dXdY	Adjustment to the location of the Celestial Intermediate Pole (CIP)	double	MX3	N/A	rad

Table 10: Breakdown of the SimParam Branch in the InitConfig.mat Structure

Name	Description	Class	Size	Value	Units
PMGravityModule	Turn on (1) or off (0) point mass gravity perturbation.	double	1X1	1 or 0	N/A
SHGravityModule	Turn on (1) or off (0) spherical harmonic gravity perturbation.	double	1X1	1 or 0	N/A
GGTModule	Turn on (1) or off (0) gravity gradient torque perturbation.	double	1X1	1 or 0	N/A
AFModule	Turn on (1) or off (0) aerodynamic force perturbation.	double	1X1	1 or 0	N/A
ATModule	Turn on (1) or off (0) aerodynamic torque perturbation.	double	1X1	1 or 0	N/A
SGravityModule	Turn on (1) or off (0) solar gravity perturbation.	double	1X1	1 or 0	N/A
MGravityModule	Turn on (1) or off (0) lunar gravity perturbation.	double	1X1	1 or 0	N/A
SPFModule	Turn on (1) or off (0) solar pressure force perturbation.	double	1X1	1 or 0	N/A
SPTModule	Turn on (1) or off (0) solar pressure torque perturbation.	double	1X1	1 or 0	N/A
RMTModule	Turn on (1) or off (0) residual magnetic torque perturbation.	double	1X1	1 or 0	N/A
CurrentSimConfig	Name of the current simulation configuration being modeled.	double	1X1	1 or 0	N/A
AeroModule	Turn on (1) or off (0) aerodynamic perturbation module.	double	1X1	1 or 0	N/A
SPModule	Turn on (1) or off (0) solar radiation pressure perturbation module.	double	1X1	1 or 0	N/A

4.2.3 Simulink

The Simulink model is shown in Figure 19, and is broken down into two major components. The first component is the Spacecraft Block, shown in Figure 20. Inputs to the spacecraft block are the force and torque vectors acting in the body fixed frame. These forces and torques are applied to the spacecraft body fixed frame which has six degrees of freedom relative to the I-frame (the world frame in Figure 20). The dynamic response of the spacecraft is transformed into its position, orientation, and velocity in space relative to the I-frame. This information is then either output from the block or used to define the position, orientation, and velocity of the spacecraft in other reference frames, such as the E-frame and the O-frame.

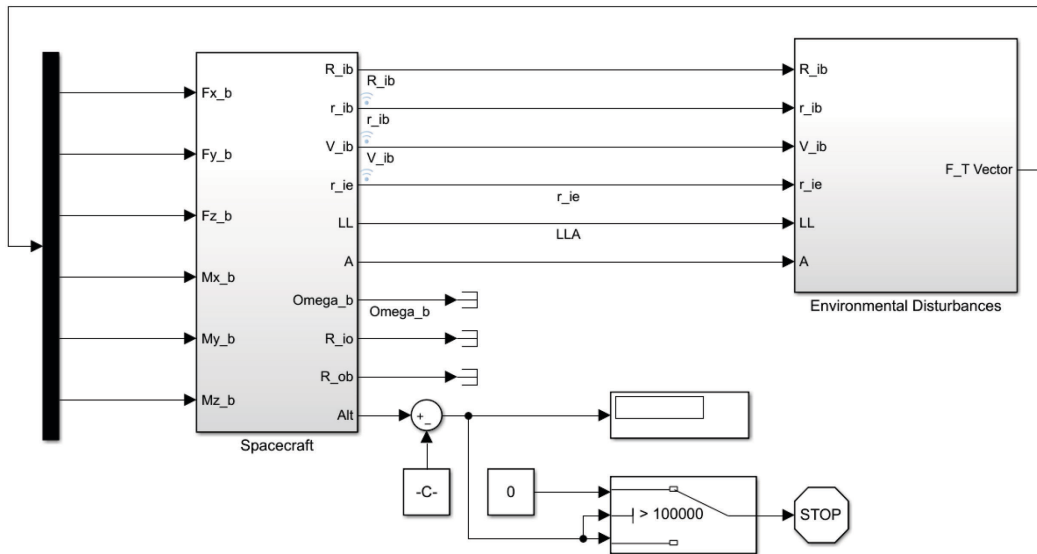


Figure 19: Simulink Model

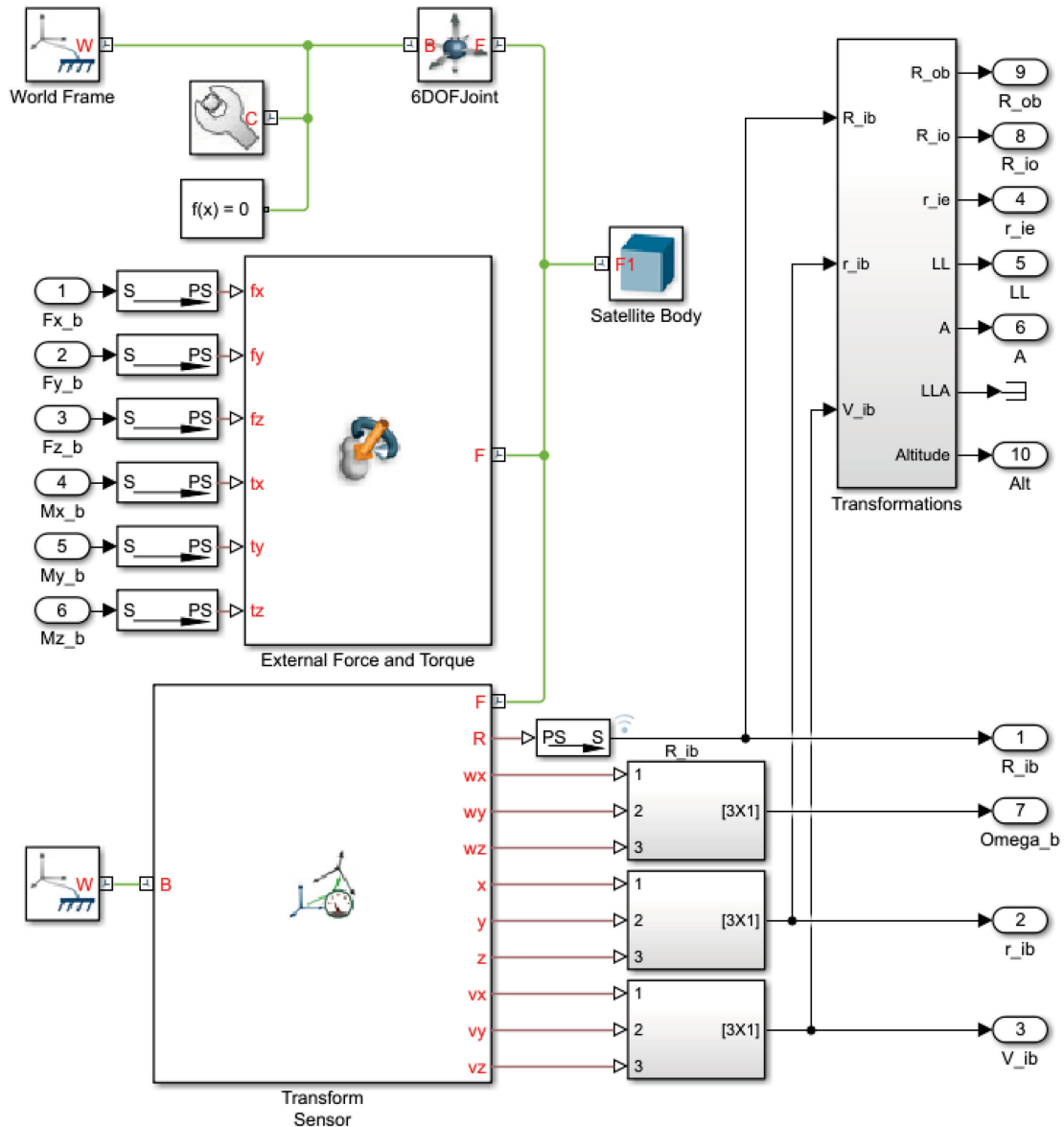


Figure 20: The Spacecraft Block

The second component of the Simulink model is the Environmental Disturbances block, shown in Figure 21. Input to the Environmental Disturbances block is the spacecraft's state relative to different reference frames (as required by different environmental models). Within the Environmental Disturbance block, are the blocks which calculate the gravity gradient torque, the lunar gravity force, the solar gravity force, the Earth gravity force, the aerodynamic force and torque, the residual magnetic torque, and the solar radiation pressure force and torque. These are calculated in the reference frame appropriate to each force and torque (often depending on the

environmental model) and transformed into the B-frame. They are then summed to determine the resulting force and torque vector and output from the Environmental Disturbances block.

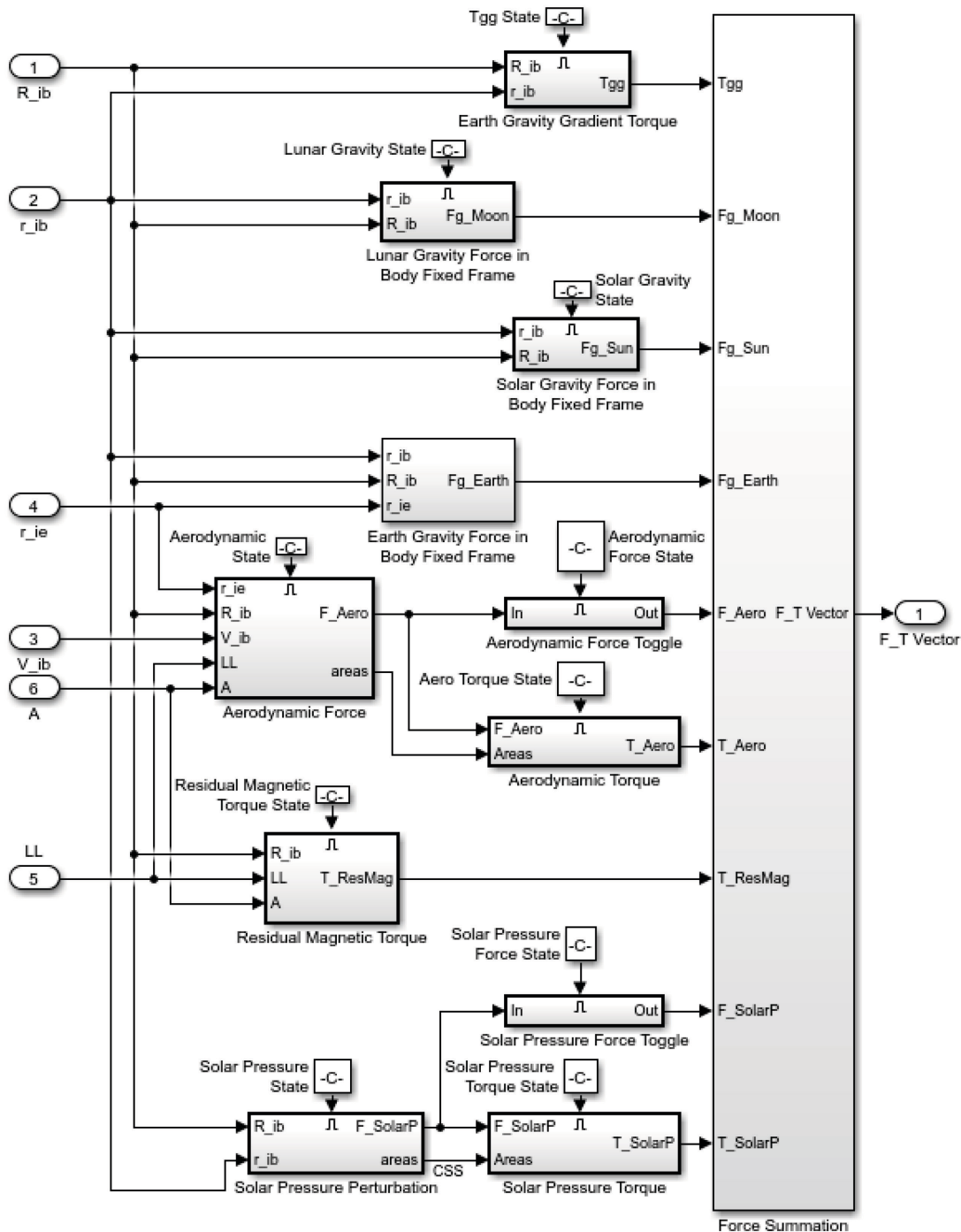


Figure 21: The Environmental Disturbances Block

4.2.4 SimData.mat

When Simulink completes the simulation, data is logged to the SimData.mat file as shown in Table 11, which is a signals file. Signals files contain the sampled signals of a logged variable at time steps defined in the Simulink environment or at the default simulation timestep. Signals obtained from SimData.mat are used to plot the trajectory of the satellite in the 2D and 3D satellite plots, and are also used to show the attitude response of the satellite while the trajectory is being plotted in the 3D plot.

Table 11: SimData.mat Signal File Structure

Name	Description	Class	Size	Units
V_ib	Spacecraft velocity vector in the ECI frame.	Signal	1X1	m/s
r_ib	Spacecraft position vector in the ECI frame.	Signal	1X1	m
r_ie	Spacecraft position vector in the ECEF frame.	Signal	1X1	m
R_io	Spacecraft rotation matrix defining the orientation of the O-frame with respect to the I frame.	Signal	1X1	Unitless
R_ob	Spacecraft rotation matrix defining the orientation of the B-frame with respect to the O-frame.	Signal	1X1	Unitless
LLA	Latitude, longitude and altitude of the spacecraft.	Signal	1X1	deg, deg, m
R_ib	Spacecraft rotation matrix defining the orientation of the O-frame with respect to the I frame.	Signal	1X1	Unitless
Altitude	Spacecraft altitude with respect to the equatorial radius.	Signal	1X1	m
CSS	Solar illumination of spacecraft surfaces from 0 - 1. Represents the output of course sun sensors.	Signal	1X1	Unitless

4.2.5 2D, 3D and Attitude Figures

After the SimData.mat file has been exported from Simulink into the MATLAB workspace, the GUI begins plotting the trajectory of the satellite in a 3D animation while at the same time animating the satellite's attitude trajectory with respect to the O-frame. Following this, the 2D ground track plot and an orbital altitude plot (with respect to WGS84) are produced. Examples are shown in Figure 22, Figure 23 and Figure 24, respectively.

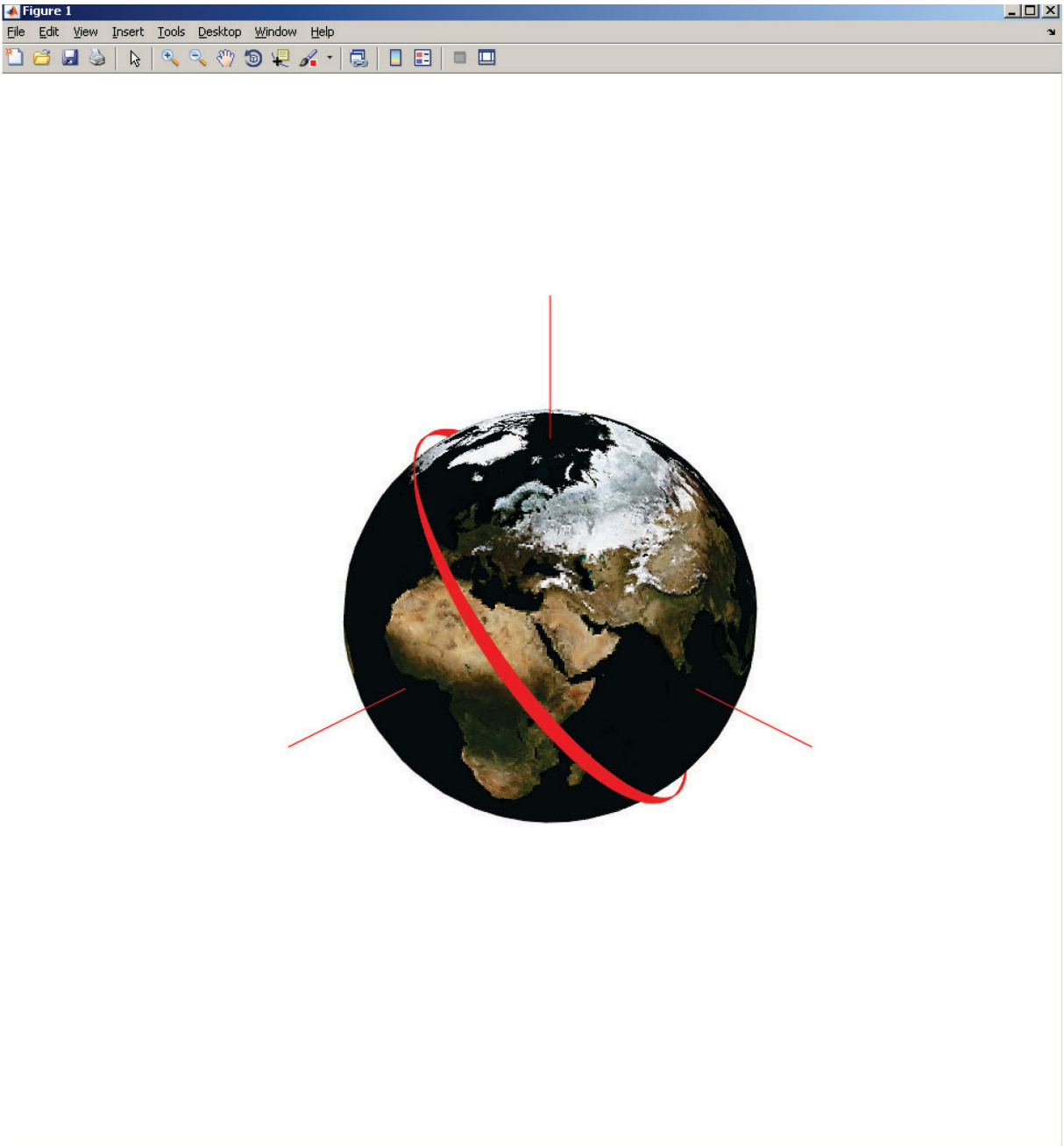


Figure 22: Example 3D Output



Figure 23: Attitude of the Spacecraft's B-frame Relative to the O-frame

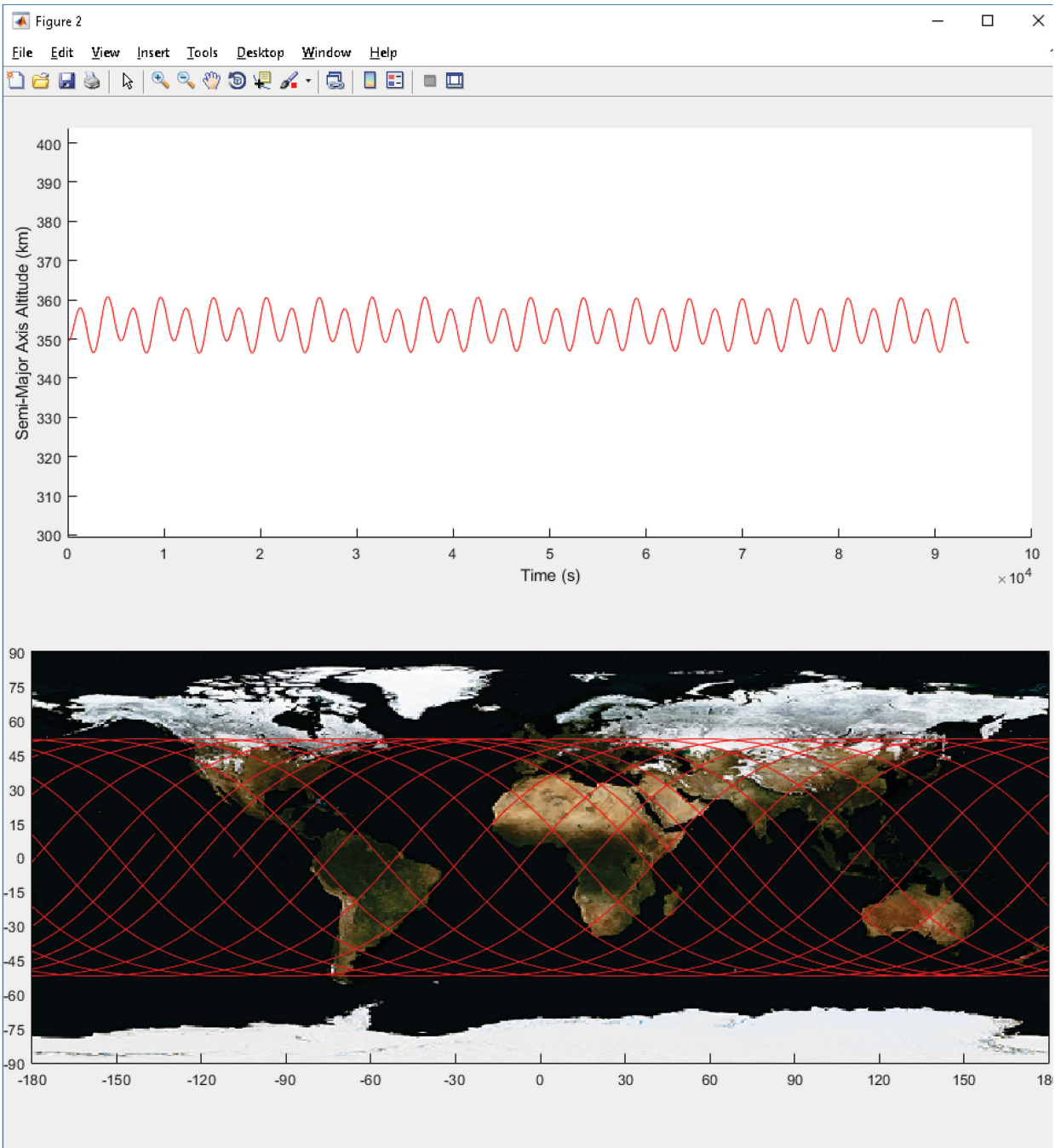


Figure 24: Example 2D Output

4.3 Summary

In this chapter, the design of OrbSim is presented. First, a general overview of OrbSim's functionalities and features is presented. OrbSim is then compared to three commercial simulation packages using the same metrics as is done in Chapter 2. Afterwards, the architecture is discussed starting at the top level, describing the interaction between the GUI, the Simulink model, and the Config.mat file. The Config.mat file is discussed, and the information stored within it presented. The high-level breakdown and features of Simulink is then presented, as well as the SimData.mat file which is used to log signals. Finally, example output, plots which use SimData.mat to display information logged during the simulation, are shown.

5 Simulation Validation

5.1 Purpose

Validation of OrbSim is necessary prior to further development. Errors in the fundamental dynamics or reference frame transformations of OrbSim would directly affect any further planned development, such as attitude and orbit determination and control modules, or other spacecraft subsystem modules. Validation against an industry standard software, or experimental data from an orbiting satellite, is thus a necessary step. For this thesis, validation of the orbital dynamics is done against an industry standard software, AGI's Systems Toolkit (STK) [27]. STK is widely used in industry and academia for space missions and has a long space heritage, and thus was chosen for validation. In fact, STK has been validated by NASA software on at least one occasion [93]. Unfortunately, attitude dynamics cannot be verified against STK's SOLIS add on because of export restrictions. Therefore, only environmental disturbance forces will be used and the orbital trajectory computed by both simulation packages compared. Following this, a simple experimental case study using a recently orbited satellite is performed.

5.2 Methodology

To test the orbital dynamics of OrbSim against STK, a simulation of a satellite in VLEO is run using different combinations of orbital perturbations to compare the performance of the environmental disturbance models created in OrbSim. The orbital trajectories output from OrbSim and STK are plotted against each other and their root mean square (RMS) error are compared. The orbital trajectories output from both simulation software packages will be in the I-frame, using

position and velocity state vectors, and the E-frame, using latitude, longitude, and altitude (LLA). These two methods of measuring the trajectory of the satellite’s orbit are tested to ensure that the transformations between the I-frame and the E-frame have been correctly implemented. Several environmental models are calculated in the E-frame, and so the transformations between E and I directly affect the calculation of the orbital trajectory because of environmental perturbations.

Seven simulations will be run in both STK, using the High-Precision Orbit Propagator (HPOP), and OrbSim. The first six simulations will be run using at least one gravity model and at most one environmental model to validate the implementation of each environmental model. The last simulation will run with all the environmental models implemented at once along with a spherical harmonic gravity model. Table 12 shows the different permutations of each of the seven simulations that are run in both STK and OrbSim. Each simulations environmental models have the same properties. The NRLMSISE-00 atmospheric model with measured space weather inputs (daily $F_{10.7}$ indices and non-interpolated 3 hourly A_p indices) obtained from Celestrak [80] will be used to model density. A spherical harmonic gravity model of fourth order using coefficients obtained from EGM2008 will be used for gravity. WGS84 will be used for the geodetic system, and the orientation of the E-frame with respect to the I-frame will be modeled as per the International Terrestrial Reference Frame (ITRF) taking into account the variations in the position of the celestial pole using Earth Orientation Parameters (EOP) obtained from Celestrak [80].

Table 12: Permutations of Orbital Perturbations for Simulation Testing

Perturbations	Simulations						
	#1	#2	#3	#4	#5	#6	#7
Two Body Gravity	X						
Spherical Harmonic Gravity, 4th Order		X	X	X	X	X	X
Solar Gravity			X				X
Lunar Gravity				X			X
Aerodynamic Drag					X		X
Solar Radiation Pressure						X	X

Both simulations model a spherical satellite with a cross sectional area of 0.0281 m^2 , a mass of 2.667 kg , assumed drag coefficient of 2.2, and assume that the spherical satellite absorbs all photons. The simulations will run for 86400 s , and use numerical solvers as per Table 13. For realism, TLE's from the orbit of the Experimental Albetan #1 (Ex-Alta 1) satellite will be used to define initial conditions, although it is worth noting that the simulation is not intended to represent Ex-Alta 1's actual trajectory. Also, it is worth noting that the TLEs should not be used in orbital propagators aside from SGP4 [66]. They are used here (and implemented in the simulation) as a handy way of generating an orbital ephemeris, but this does not constitute experimental data. Table 14 shows the Keplerian Elements and epoch for the two TLE's used.

Table 13: Simulation Parameters

Simulation	Simulation Time (s)	Solver	Relative Tolerance	Absolute Tolerance
OrbSim	86,400	RKDP 4(5)	1E-12	1E-12
STK	86,400	RKF 7(8)	1E-13	Unknown

Table 14: TLE's used for Simulation [94]

	TLE 1	TLE 2
Semi-Major Axis (km)	6781.2815	6731.9849
Eccentricity	0.0009	0.0007
Inclination (deg)	51.6366	51.6328
Argument of Perigee (deg)	199.9661	18.8996
RAAN (deg)	143.4509	227.3938
True Anomaly (deg)	284.9511	341.2002
Date (YYYY-MM-DD)	2017-05-27	2018-05-02
Time (UTC, HH:MM:SS)	2:14:29	7:45:19
Second Fractions	0.8576	0.2243

5.3 Results & Discussion

All seven simulation permutations were run for both TLE's, graphs created and the RMS error values recorded. An example plot comparing the orbital trajectory of a satellite simulated in

OrbSim and STK of simulation configuration #7 with TLE#2 is shown in Figure 25. Appendix B contains all 70 plots created; however, Table 15 and Table 16 summarize the RMS error for all 70 plots. RMS error is calculated as per equation 5-1. Shown in Table 17 is the average of the RMS error for run #1 between TLE#1 and TLE #2, and the average of all the runs from #2 to #7 for TLE#1 and TLE#2. Finally, Table 18 shows the relative RMS error, which is calculated as per 5-2.

$$RMSE = \sqrt{\frac{1}{N} \sum_{n=1}^N (OrbSim_n - STK_n)^2} \quad 5-1$$

Where $RMSE$ is the RMS error, $OrbSim_n$ and STK_n are signals produced by both simulation containing either the position, velocity, or LLA.

$$Relative\ RMSE = \sqrt{\frac{1}{N} \sum_{n=1}^N \left(\frac{OrbSim_n - STK_n}{STK_n} \right)^2} \quad 5-2$$

Where $Relative\ RMSE$ is the relative RMS error.

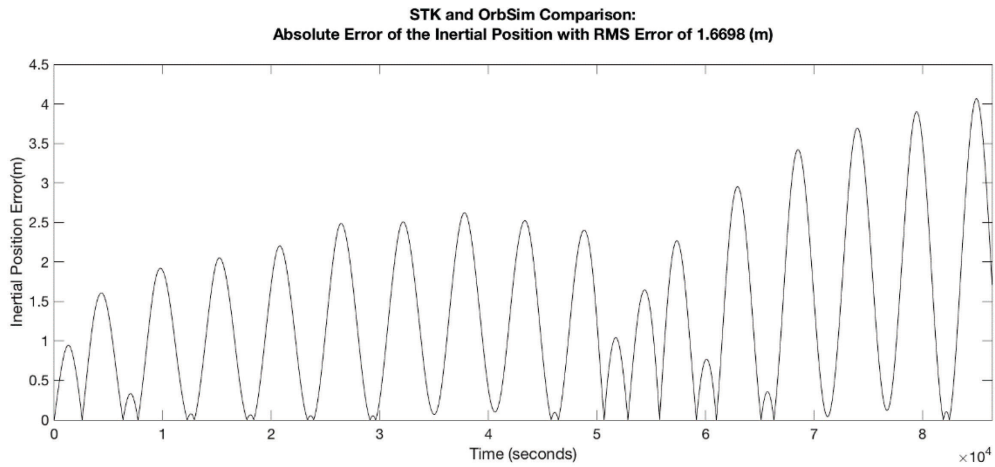
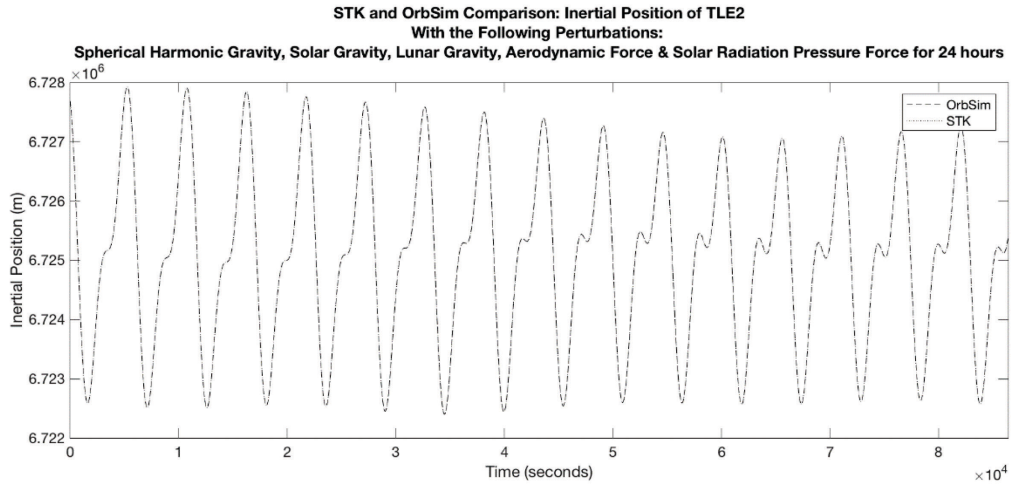


Figure 25:TLE#2 Inertial Position Comparison

Table 15: RMS error for TLE#1 Simulation Comparison Between OrbSim and STK

	#1	#2	#3	#4	#5	#6	#7
Position (m)	8.01E-01	1.18E+00	1.18E+00	1.18E+00	9.65E+00	3.23E+00	9.85E+00
Velocity (m/s)	9.09E-04	1.23E-03	1.23E-03	1.23E-03	5.58E-03	3.62E-03	6.26E-03
Lat. (deg)	2.92E-04	3.47E-04	3.42E-04	3.43E-04	3.28E-03	3.33E-04	3.26E-03
Long. (deg)	2.97E-04	4.55E-04	4.41E-04	4.40E-04	5.68E-03	4.21E-04	5.64E-03
Altitude (m)	8.00E-01	1.18E+00	1.18E+00	1.18E+00	9.68E+00	3.23E+00	9.88E+00

Table 16: RMS error for TLE#2 Simulation Comparison Between OrbSim and STK

	#1	#2	#3	#4	#5	#6	#7
Position (m)	6.65E-01	7.40E-01	7.40E-01	7.40E-01	1.84E+00	1.19E+00	1.67E+00
Velocity (m/s)	7.61E-04	7.88E-04	7.88E-04	7.88E-04	1.22E-03	1.22E-03	1.41E-03
Lat. (deg)	3.04E-04	3.11E-04	3.11E-04	3.11E-04	3.33E-04	3.60E-04	4.16E-04
Long (deg)	5.20E-04	4.18E-04	4.18E-04	4.17E-04	6.57E-04	6.85E-04	9.03E-04
Altitude (m)	6.67E-01	7.43E-01	7.43E-01	7.42E-01	1.83E+00	1.19E+00	1.67E+00

Table 17: Average RMS Error for TLE#1 and TLE#2

	Run #1	Runs #2 - #7
Position (m)	7.3302E-01	2.7645E+00
Velocity (m/s)	8.3515E-04	2.1133E-03
Latitude (deg)	2.9798E-04	8.2932E-04
Longitude (deg)	4.0885E-04	1.3817E-03
Altitude (m)	7.3359E-01	2.7699E+00

Table 18: Relative RMS Error for Run #7

	Final Values TLE#1 STK	Final Values TLE#2 STK	Final Average RMS Error	Final Relative RMS Error TLE#1	Final Relative RMS Error TLE#2	Final Average Relative RMS Error
Position (m)	6.79E+06	6.73E+06	5.7596E+00	0.00014516%	0.00002483%	0.00008499%
Velocity (m/s)	7.66E+03	7.70E+03	3.8364E-03	0.00008173%	0.00001832%	0.00005003%
Latitude (deg)	-27.715	-51.84	1.8391E-03	0.93393559%	0.18485530%	0.55939545%
Longitude (deg)	-1.65E+02	1.56E+02	3.2734E-03	2.02315905%	0.26916937%	1.14616421%
Altitude (m)	4.13E+05	3.60E+05	5.7757E+00	0.00239196%	0.00047236%	0.00143216%

Looking at the results, we find that OrbSim performs favorably on par with STK. First, it is worth noting that OrbSim very accurately tracks a reference Keplerian orbit (an ideal orbit) in both the I-frame and the E-frame as we see in Table 17 and for run #1. This result shows that the transformations between the E-frame and the I-frame are being executed correctly. In fact, the altitude above the reference ellipsoid (WGS84) is tracked almost on par with the position in the I-frame. It is also worth noting that this result is similar in magnitude to the comparison to STK using a Keplerian orbit performed in [40].

Looking at the average RMS error from environmental perturbations makes it clear that OrbSim is on par with STK, and that while there is more error because of environmental models than in #1, there is no significant error that would indicate a major error or omission. Also, the same conclusion concerning the transformations between the E-frame and the I-frame may be reached as there is very little difference between position and altitude RMS errors. Looking more closely at the individual results of the environmental perturbation simulation runs from Table 15, Table 16 and Appendix B, some more interesting things may be found. For example, for TLE#1 the RMS error from the aerodynamic drag run, while still small, appears anomalous compared to the other runs. However, looking at the same information for TLE#2, the RMS error is lower, but the graph of absolute error tells an interesting tale. The error takes a sudden jump after halfway

through the simulation. When looking at aerodynamic drag, it is important to remember that predicting this force is difficult, and subject to many large uncertainties in atmospheric density, drag coefficient, and the relative velocity vector between the satellite and the free-stream velocity [68]. Atmospheric density models, as noted in [68], have an average uncertainty between 10-15%; however, this can jump to 100% uncertainty in the short term. Additionally, the inputs into an atmospheric model are as important as the model itself, as noted in [67]. While both simulations use the NRLMSISE-00 atmospheric model, there is a limit to how much a user may control or verify the model in STK, while the Simulink block for NRLMSISE-00 is much easier to control and verify. As a result, it is perhaps not surprising that of all the environmental perturbations, aerodynamic drag is the largest. Still, the average RMS error for position and altitude for run #5 is still quite low (~5.76 m) compared to the average semi-major axis simulated (~6750 km). It is also worth noting that there is no wind model defined in STK for upper atmospheric winds, which may itself account for the error trend.

Table 18 presents an idea about the relative error in each metric tracked. Interestingly, it is noted that the error in the latitude and longitude between OrbSim and STK is many orders of magnitude larger than the errors in position and velocity. Altitude is only a couple orders of magnitude larger than position and velocity. It is also interesting to note the relative RMS error in longitude for TLE#1, as there was also a noticeable RMS error in altitude during run #5, the aerodynamic run. This may be due to atmospheric modelling error. In fact, this may be due to the wind model used in OrbSim vs STK. Specifically, there does not seem to be a wind model for satellites in STK, while for OrbSim, it is assumed that the atmosphere rotates in the longitudinal direction.

The figures for latitude and longitude absolute error (Appendix B) for each perturbation, except for two body gravity, for both TLE's have interesting trends that differ from the ideal two body scenario. For example, compare latitude and longitude error plots shown in Figure 45 and Figure 46, with Figure 50 and Figure 51. Figure 45 and Figure 46, which were plotted using spherical harmonic gravity and lunar gravity, show the same trends as Figure 50 and Figure 51, which were plotted using spherical harmonic gravity and aerodynamic drag, but the trends in the latter plots are more pronounced (this is likely a result of aerodynamic modelling differences as previously discussed). These trends are independent of other trends observed in inertial position, inertial velocity and altitude figures. Errors due to machine precision or truncation error can be

discounted as the primary source for the divergent trend, as these would also be present in other plots. Deconstructing these trends may help identify the source of the error. For latitude, we see the error getting larger with time, while still fluctuating about the mean. For longitude, the amplitude of absolute error oscillations are growing while the mean error is also diverging from zero. This suggests that rotation rate of the Earth used in STK and OrbSim for the transformation between the I-frame and the E-frame may be different. This is because the mean of the longitude is drifting from zero over time, which suggests that one simulation's Earth is rotating faster than the other. The growing absolute error in longitude corroborates this. Imagine measuring the latitude of two satellites in the same orbital profile, but offset by some small degree of longitude, which is growing with time. Plotting the difference between the latitudes would result in the same plot. Overall, these trends are worth exploring. It may be difficult to do this however, as a program like STK cannot be explored thoroughly due to its proprietary nature, and so any difference in values between rotation rates, for example, may not be easily identified.

Finally, it is worth talking about the general trend in the error and different sources of error. There is clearly some numerical error that increases the overall error of the simulation as time goes on. These are subtle in many of the graphs in Appendix B. Also, there will be differences in error between STK and OrbSim purely because of simulation error tolerances and the selected solvers. For example, STK has a relative tolerance setting of $1E-13$, while Simulink is limited to $1E-12$. Additionally, the solvers used by STK and by Simulink have their own error handling processes (and at different levels of tolerance) and numerical solution methods. These may be a source of the difference in error between the two simulations.

5.4 Simple Case Study

On January 21, 2018, The Humanity Star was launched into LEO by Rocket Lab to be a shining inspiration to look up at the night sky. The Humanity Star was a geodesic sphere with 76 reflecting surface. It was 1 *m* tall, and had a mass of 10.34 *kg*. It was predicted to stay in orbit for nine months from its launch date before burning up in the Earth's atmosphere. However, The Humanity Star entered orbit much earlier than planned, burning up on March 22, 2018 at about 10:00 UTC. Little more than two months from orbit insertion. [95], [96]

The Humanity Star, being a roughly spherical shape, with smooth reflective surfaces, a known trajectory, and an object that was very recently in orbit, is a perfect candidate for a simple

test of OrbSim. Unfortunately, without the inertial properties, precise orbit ephemerides, initial spin rate or an idea of what the surface materials are, a more complex analysis involving environmental torques cannot be completed. Instead, the orbital trajectory will be predicted using several simplifying assumptions. It will be assumed that The Humanity Star is a perfect sphere 1 *m* in diameter for the purposes of calculating aerodynamic drag and solar radiation pressure. It will also be assumed that its COM is located at its COGEO. Environmental perturbations will include non-uniform gravity, solar gravity, lunar gravity, aerodynamic drag, and solar radiation pressure. The simulation will begin from the first TLE generated by NORAD for The Humanity Star (Table 19). The objective of the test will be to predict the re-entry date and to estimate the drag coefficient. A secondary objective will involve running the simulation in STK using the same parameters to compare OrbSim's long term performance. Once again, it is worth noting that TLEs of orbiting satellites should only be used with SGP4 for any sort of accuracy. As TLEs represent mean values, it is expected that the orbital trajectory should roughly match the tracking data from NORAD.

Table 19: First TLE for The Humanity Star [94]

	TLE
Semi-Major Axis (km)	6791.0091
Eccentricity	0.0173
Inclination (deg)	82.9177
Argument of Perigee (deg)	221.5801
RAAN (deg)	139.4148
True Anomaly (deg)	213.9762
Date (YYYY-MM-DD)	2018-01-21
Time (UTC, HH:MM:SS)	02:44:23
Second Fractions	0.7852

The results of this test are shown in Figure 26 and Table 20. Figure 26 compares the actual and estimated semi-major altitude (semi-major axis minus the Earth’s equatorial radius) of The Humanity Star. Table 20 shows actual and predicted re-entry estimates. Based on this test, the drag coefficient of The Humanity Star is approximately 2.55. Additionally, there are some interesting things to note concerning the performance of OrbSim versus STK. First, we note that the starting altitude for OrbSim and STK match each other, and as expected, do not match the tracking data. This was expected given that a TLE was used with a numerical propagator. Another interesting thing to note, is that while STK’s prediction of re-entry was much closer than OrbSim’s, the shape of OrbSim’s predicted trajectory closely matched the actual trajectory of The Humanity Star. On the other hand, STK’s predicted trajectory diverged from OrbSim’s, and from the shape of The Humanity Star’s trajectory. Lastly, it is worth noting that the predicted drag coefficient does not match the typical drag coefficient of 2.2. There are likely many possible reasons for this, for example, the surface of The Humanity Star may be more specular than diffuse, the surface is not a perfect sphere, and the drag coefficient of space objects tends to change with altitude, especially in LEO [68].

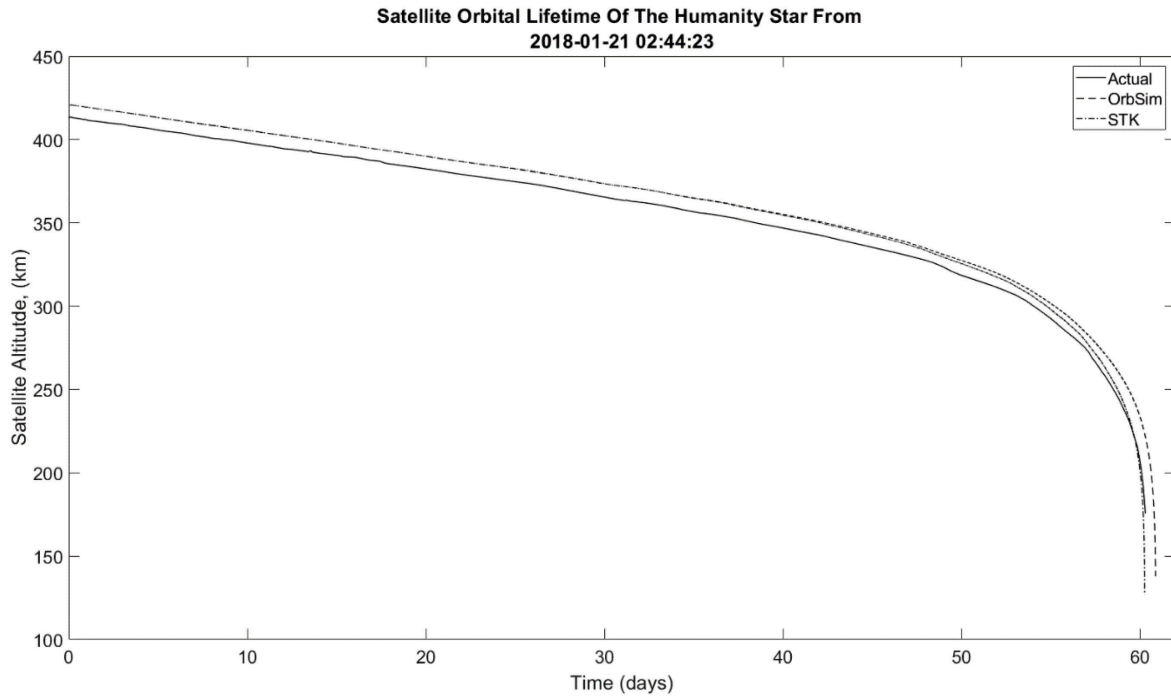


Figure 26: Lifetime Plot of The Humanity Star Using Actual Tracking Data, and Predictions From OrbSim and STK

Table 20: Re-entry Data for The Humanity Star

	Actual	Predicted by OrbSim	Predicted by STK
Days From Beginning of Life to Re-Entry	60.312	60.875	60.271
Date of Re-Entry	2018-03-22 10:13:29	2018-03-22 23:44:29	2018-03-22 09:14:02

5.5 Analysis and Conclusion

The position, velocity, latitude, longitude, and altitude have been obtained from simulations of a spherical satellite completed in OrbSim and STK for each of the seven permutations for TLE #1 and TLE #2, and their RMS error calculated. Additionally, the average RMS error of run #7, and the relative RMS error have been presented. Through this exercise it was found that OrbSim performed very well relative to STK; as a result, OrbSim was validated. Additionally, a simple case study using The Humanity Star was performed to compare OrbSim's prediction capability to a real-world experiment. During this test, OrbSim and STK simulated the orbital trajectory of The Humanity Star from its first TLE. The simulated trajectories were then compared to actual tracking data. It was concluded that OrbSim did well tracking the actual trajectory of The Humanity Star, despite using TLEs as initial conditions for numerical propagation.

6 Conclusion and Future Work

6.1 Conclusion

This thesis has identified and addressed the need for an open source satellite dynamics simulation environment in MATLAB/Simulink for future research on AAOCS. The foundational math required to model the satellite dynamics under the effect of perturbation forces and torques was presented along with the different reference frames used. A designed and usable simulation environment, called OrbSim, created in MATLAB/Simulink was described through the presentation of the architecture of the Simulation, the functionalities of both the GUI and the Simulink environment, and the data handling structure. OrbSim's environmental disturbance forces have been validated against an industry standard software, STK, and shown to perform comparably. Finally, OrbSim was the subject of a simple case study using the orbital decay of The Humanity Star.

6.2 Future Work

OrbSim is currently in a state where it could be used by a satellite mission designer to model the orbital and attitude dynamics of a satellite. Furthermore, based on an outside user's experience as observed by the author, additional analyses can be performed which are incredibly useful to space mission design. For example, power generation cases of a satellite in different attitude and orbital configurations can be calculated, satellite ground station access can be

predicted, sun-synchronous orbits can be modeled, and passive aerodynamic attitude control may be modeled. However, before this can be completed, some future work is necessary.

The first goal to reach towards in future development of OrbSim is full validation of the astrodynamics environment with both software and experimental data. This will involve validation of both the coupled orbital and attitude dynamics. Additionally, this will require experimental validation from an orbiting satellite. As a secondary goal to reach for, it will be useful to complete a sensitivity analysis on Simulinks numerical integrators, their absolute error and their relative error. The second goal to reach towards in the future development of OrbSim is its release as an open source software package. This will involve determining which license to release under, creating useful documentation, choosing an online software repository, and organizing the space library created with this simulation. A secondary goal to reach for at the same time is to improve the usability and general user experience of the package in order to encourage more general use.

Longer term goals to reach towards in the future development of OrbSim is the development of additional modules. For example, a power generation module, a ground track visibility module, an Earth observation satellite analysis module, the advanced spacecraft configuration module, the advanced simulation configuration module, the addition of the DTM-09 and JB-2008 atmospheric models, the addition of an attitude and orbit determination, and control module and the addition of a satellite communications module.

In addition to the software related goals previously defined, there are now research goals that may be performed with OrbSim in the realm of AAOCS design, analysis, and optimization. These include:

1. Simulating previously researched AAOCS concepts to inspect the validity of the assumptions made in the simulation of their orbital and attitude dynamics.
2. Completing a performance analysis on different AAOCS concepts and performing a trade study to identify which concept is useful for what application.
3. Designing and optimizing an AAOCS configuration and control system using OrbSim can now be completed.
4. Completing a performance analysis on different aerodynamic models (panel method, ray tracing and DSMC) to determine when they should be used.

References

- [1] “CubeSat.org,” *CubeSat*. [Online]. Available: <http://www.cubesat.org/about/>. [Accessed: 04-Mar-2017].
- [2] D. Selva and D. Krejci, “A survey and assessment of the capabilities of Cubesats for Earth observation,” *Acta Astronaut.*, vol. 74, pp. 50–68, May 2012.
- [3] J. Straub, “Cubesats: A low-cost, very high-return space technology,” in *Proceedings of the 2012 Reinventing Space Conference*, 2012.
- [4] A. Chin, R. Coelho, R. Nugent, R. Munakata, and J. Puig-Suari, “CubeSat: The Pico-Satellite Standard for Research and Education,” presented at the AIAA Space 2008 Conference & Exposition, 2008, p. 7734.
- [5] A. Chin, R. Coelho, L. Brooks, R. Nugent, and J. Puig-Suari, “Standardization promotes flexibility: A review of CubeSats’ success,” *Aerosp. Eng.*, vol. 805, pp. 756–5087, 2008.
- [6] J. V. Llop, P. C. Roberts, Z. Hao, L. R. Tomas, and V. Beauplet, “Very Low Earth Orbit mission concepts for Earth Observation. Benefits and challenges.,” in *12th Reinventing Space Conference, London, United Kingdom*, 2014, vol. 520.
- [7] P. C. E. Roberts *et al.*, “DISCOVERER - Radical Redesign of Earth Observation Satellites for Sustained Operation at Significantly Lower Altitudes,” presented at the 68th International Astronautical Congress (IAC), Adelaide, Australia, 2017, pp. 1–9.
- [8] M. L. Psiaki, “Nanosatellite Attitude Stabilization Using Passive Aerodynamics and Active Magnetic Torquing,” *J. Guid. Control Dyn.*, vol. 27, no. 3, pp. 347–355, Jun. 2004.
- [9] J. Auret, “Design of an aerodynamic attitude control system for a CubeSat,” University of Stellenbosch, 2012.
- [10] Mi. L. Gargasz, “Optimal Spacecraft Attitude Control Using Aerodynamic Torques,” Air Force Institute of Technology, Wright-Patterson Air Force Base, Ohio, 2007.
- [11] R. R. Kumar, D. D. Mazanek, and M. L. Heck, “Simulation and Shuttle Hitchhiker validation of passive satellite aerostabilization,” *J. Spacecr. Rockets*, vol. 32, no. 5, pp. 806–811, Sep. 1995.
- [12] J. Virgili-Llop, H. C. Polat, and M. Romano, “Using Shifting Masses to Reject Aerodynamic Perturbations and to Maintain a Stable Attitude in Very Low Earth Orbit,” presented at the 26th AAS/AIAA Space Flight Mechanics meeting, Napa, California, 2016.
- [13] S. A. Rawashdeh and J. E. Lumpp Jr, “Aerodynamic Stability for CubeSats at ISS Orbit,” *J. Small Satell.*, vol. 2, no. 1, pp. 85–104, 2013.
- [14] W. H. Steyn and M.-A. Kearney, “An Attitude Control System for ZA-AeroSat subject to significant Aerodynamic Disturbances .pdf,” presented at the The International Federation of Automatic Control, Cape Town, South Africa, 2014, vol. 47, pp. 7929–7934.
- [15] S. Varma, “Control of satellites using environmental forces : aerodynamic drag / solar radiation pressure,” *Theses Diss.*, p. 219, 2011.
- [16] J. V. Llop, “Spacecraft Flight in the Atmosphere,” PhD Thesis, School of Engineering, Cranfield University, 2014.
- [17] M. Pastorelli, R. Bevilacqua, and S. Pastorelli, “Differential-drag-based roto-translational control for propellant-less spacecraft,” *Acta Astronaut.*, vol. 114, pp. 6–21, Sep. 2015.
- [18] C. Foster, H. Hallam, and J. Mason, “Orbit determination and differential-drag control of planet labs cubesat constellations,” *ArXiv Prepr. ArXiv150903270*, 2015.

- [19] D. Pérez and R. Bevilacqua, “Differential drag spacecraft rendezvous using an adaptive Lyapunov control strategy,” *Acta Astronaut.*, vol. 83, pp. 196–207, 2013.
- [20] S. M. Shuford, “Feasibility of CubeSat Formation Flight Using Rotation to Achieve Differential Drag,” 2013.
- [21] J. Gangestad, B. Hardy, and D. Hinkley, “Operations, orbit determination, and formation control of the AeroCube-4 CubeSats,” presented at the AIAA/USU Conference on Small Satellites, 2013.
- [22] D. du-Toit, J. Du Plessis, and W. Steyn, “Using atmospheric drag for constellation control of Low Earth Orbit micro-satellites,” *Dept Electr. Electron. Eng. Univ. Stellenbosch 7600 Repub. South Afr.*, 1996.
- [23] H. Nagno, Y. Hayakawa, H. Osuga, T. Ozaki, and K. Shuto, “A New Orbit Control Algorithm for the 20 mN Class Ion Engine System,” presented at the 33rd International Electric Propulsion Conference, The George Washington University, Washington, DC, USA, 2013.
- [24] “JAXA | Super Low Altitude Test Satellite ‘TSUBAME’ (SLATS),” *JAXA | Japan Aerospace Exploration Agency*. [Online]. Available: <http://global.jaxa.jp/projects/sat/slats/>. [Accessed: 19-Aug-2018].
- [25] C. E. Ghisi, C. Steiger, M. Romanazzo, and P. P. Emanuelli, “Drag-Free Attitude and Orbit Control System Performance of ESA’s GOCE Mission during Low Orbit Operations and De-orbiting,” in *SpaceOps 2014 Conference*, Pasadena, CA, 2014.
- [26] “FreeFlyer® Software,” *ai-solutions.com*. [Online]. Available: <https://ai-solutions.com/freelyer/>. [Accessed: 12-Aug-2018].
- [27] “AGI,” *Agi*. [Online]. Available: <http://www.agi.com/home>. [Accessed: 12-Aug-2018].
- [28] “Astos Solutions.” [Online]. Available: <https://www.astos.de/>. [Accessed: 14-Aug-2018].
- [29] “Spacecraft Control Toolbox | Princeton Satellite Systems.” [Online]. Available: <http://www.psatellite.com/products/sct/>. [Accessed: 16-Aug-2018].
- [30] “Software | Microcosm.”
- [31] “GMAT.” [Online]. Available: <https://software.nasa.gov/software/GSC-17177-1>. [Accessed: 14-Aug-2018].
- [32] “jat.sourceforge.net.” [Online]. Available: <http://jat.sourceforge.net/>. [Accessed: 14-Aug-2018].
- [33] “Tudat,” *GitHub*. [Online]. Available: <https://github.com/Tudat>. [Accessed: 14-Aug-2018].
- [34] “About.” [Online]. Available: <http://orekit.org/>. [Accessed: 14-Aug-2018].
- [35] D. Lee, J. Springmann, S. Spangelo, and J. Cutler, “Satellite Dynamics Simulator Development Using Lie Group Variational Integrator,” in *AIAA Modeling and Simulation Technologies Conference*, Portland, Oregon, 2011.
- [36] P. Riihimäki and J.- Ylén, “Simulation of Spacecraft Attitude and Orbit Dynamics,” in *Proceedings 19th European Conference on Modelling and Simulation*, 2005, pp. 1–4.
- [37] I. Pelivan, A. Heidecker, and S. Theil, “High performance satellite dynamics and control simulation for multi-purpose application,” *J. Aerosp. Eng. Sci. Appl.*, vol. 4, no. 3, pp. 119–130, Jul. 2012.
- [38] S. Habibkhan, J. Arasi, and H. Bolandi, “SPACSSIM: Simulation and Analysis Software for Mathematical Modeling of Satellite Position and Attitude Control Systems,” *Comput. Sci. Eng.*, vol. 19, no. 5, pp. 38–48, 2017.

- [39] T. Pulecchi, F. Casella, and M. Lovera, “Object-oriented modelling for spacecraft dynamics: Tools and applications,” *Simul. Model. Pract. Theory*, vol. 18, no. 1, pp. 63–86, Jan. 2010.
- [40] A. J. Turner, “An Open-Source, Extensible Spacecraft Simulation And Modeling Environment Framework,” Master of Science in Aerospace Engineering, Blacksburg, Virginia, 2003.
- [41] V. Carrara, “An Open Source Satellite Attitude and Orbit Simulator Toolbox for Matlab,” presented at the 17th International Symposium on Dynamic Problems of Mechanics, 2015, p. 13.
- [42] A. H. De Ruiter, C. Damaren, and J. R. Forbes, *Spacecraft Dynamics and Control: An Introduction*. John Wiley & Sons, 2012.
- [43] “Smart Nanosatellite Attitude Propagator (SNAP) | Space Systems Laboratory.” .
- [44] “CubeSat Design Specification, Rev 13.” California Polytechnic State University, 20-Feb-2014.
- [45] E. Kulu, “Nanosatellite & CubeSat Database,” *Nanosatellite & CubeSat Database*. [Online]. Available: <http://www.nanosats.eu/index.html>. [Accessed: 14-Dec-2017].
- [46] J. R. Wertz, D. F. Everett, and J. J. Puschell, *Space Mission Engineering: The New SMAD*, 1st ed. Hawthorne, CA: Microcosm Press, 2011.
- [47] Thuvt, *English: F-1 CubeSat Flight Model*. 2011.
- [48] “6U Cubesat Design Specification.pdf.” California Polytechnic State University, 20-Apr-2016.
- [49] B. Streetman, J. Shoer, and L. Singh, “Limitations of scaling momentum control strategies to small spacecraft,” in *Aerospace Conference, 2017 IEEE*, 2017, pp. 1–7.
- [50] N. E. Chahat, “New Antennas Will Take CubeSats to Mars and Beyond,” *IEEE Spectrum: Technology, Engineering, and Science News*, 25-Jan-2018. [Online]. Available: <https://spectrum.ieee.org/aerospace/satellites/new-antennas-will-take-cubesats-to-mars-and-beyond>. [Accessed: 22-Aug-2018].
- [51] D. G. King-Hele and R. R. Allan, “The Rotational Speed of the Upper Atmosphere.pdf,” *Space Sci. Rev.*, vol. 6, Jun. 1966.
- [52] K. Cranford, “An improved analytical drag theory for the artificial satellite problem,” 1969, p. 925.
- [53] “NASA Space Vehicle Design Criteria: Aerodynamic Torques for Spacecraft.pdf.” NASA, Jan-1971.
- [54] R. R. Kumar, D. D. Mazanek, and M. L. Heck, “Parametric and classical resonance in passive satellite aerostabilization,” *J. Spacecr. Rockets*, vol. 33, no. 2, pp. 228–234, Mar. 1996.
- [55] “STS-77 Space Shuttle Mission Report.pdf,” NASA, Jun. 1996.
- [56] “Aerodynamic Attitude Stabilization for Ram Facing Cubesats.pdf,” *Adv. Astronaut. Sci.*, vol. 133, pp. 583–595, 2009.
- [57] J. Armstrong, C. Casey, G. Creamer, and G. Dutchover, “Pointing Control for Low Altitude Triple Cubesat Space Darts.pdf,” in *Elements of New Space Systems*, 2009.
- [58] T. Bak and R. Wisniewski, “Passive Aerodynamic Stabilisation of Low Earth Orbit Satellite,” *Spacecr. Guid. Navig. Control Syst.*, vol. 381, p. 469, 1997.
- [59] “Colony-1 Cubesats - Satellite Missions - eoPortal Directory.” [Online]. Available: <https://directory.eoportal.org/web/eoportal/satellite-missions/content/-/article/colony1>. [Accessed: 20-Feb-2018].

- [60] J. Virgili and P. C. E. Roberts, “ Δ Sat, a QB50 CubeSat mission to study rarefied-gas drag modelling,” *Acta Astronaut.*, vol. 89, pp. 130–138, Aug. 2013.
- [61] J. V. Llop, P. C. Roberts, and Z. Hao, “Aerodynamic Attitude and Orbit Control Capabilities of The Δ Dsat CubeSat,” in *January 31 - February 5, 2014*, Breckenridge, Colorado.
- [62] D. B. Guettler, “Satellite attitude control using atmospheric drag,” AIR FORCE INST OF TECH WRIGHT-PATTERSON AFB OH GRADUATE SCHOOL OF ENGINEERING AND MANAGEMENT, 2007.
- [63] S. Chesi, “Attitude control of nanosatellites using shifting masses,” PhD Thesis, University of California, Santa Cruz, 2015.
- [64] J. Auret and W. H. Steyn, “Design of an Aerodynamic Attitude Control System for a CubeSat,” presented at the International Astronomical Conference 11, vol. E2.2.3.
- [65] esa, “GOCE,” *European Space Agency*. [Online]. Available: http://www.esa.int/Our_Activities/Observing_the_Earth/GOCE. [Accessed: 19-Aug-2018].
- [66] D. Vallado, P. Crawford, R. Hujsak, and T. Kelso, “Revisiting spacetrack report# 3,” in *AIAA/AAS Astrodynamics Specialist Conference and Exhibit*, 2006, p. 6753.
- [67] D. A. Vallado and D. Finkleman, “A critical assessment of satellite drag and atmospheric density modeling,” *Acta Astronaut.*, vol. 95, pp. 141–165, Feb. 2014.
- [68] D. Mostaza Prieto, B. P. Graziano, and P. C. E. Roberts, “Spacecraft drag modelling,” *Prog. Aerosp. Sci.*, vol. 64, pp. 56–65, Jan. 2014.
- [69] S. A. Rawashdeh and J. E. Lumpp, “CubeSat Aerodynamic Stability at ISS Altitude and Inclination,” p. 12.
- [70] “Satellite Tracking System: Orbitron by Sebastian Stoff / Satellite tracking easiest ever!” [Online]. Available: <http://www.stoff.pl/>. [Accessed: 16-Aug-2018].
- [71] “GMAT Wiki Home - GMAT Wiki - GMAT.” [Online]. Available: <http://gmatcentral.org/>. [Accessed: 12-Aug-2018].
- [72] M. J. Sidi, *Spacecraft dynamics and control: a practical engineering approach*. Cambridge: Cambridge Univ. Press, 1997.
- [73] G. Petit and B. Luzum, “(IERS Technical Note; No. 36),” no. 36, p. 179.
- [74] F. L. Markley and J. L. Crassidis, *Fundamentals of spacecraft attitude determination and control*. New York: Springer, 2014.
- [75] L. Reeves, “Introduction to Orbital Mechanics.”
- [76] R. Schwarz, “Memorandum No. 2: Cartesian State Vectors to Keplerian Orbit Elements,” Oct. 2017.
- [77] A. Noureldin, T. B. Karamat, and J. Georgy, “Basic Navigational Mathematics, Reference Frames and the Earth’s Geometry,” in *Fundamentals of Inertial Navigation, Satellite-based Positioning and their Integration*, Berlin, Heidelberg: Springer Berlin Heidelberg, 2013, pp. 21–63.
- [78] “STK - Technical Overview of Central Body Reference Frames (Coordinate Systems).” [Online]. Available: <http://help.agi.com/stk/index.htm#stk/referenceFramesCentralBodies.htm>. [Accessed: 19-Aug-2018].
- [79] “IERS.” [Online]. Available: https://www.iers.org/IERS/EN/Home/home_node.html. [Accessed: 21-Aug-2018].
- [80] “CesTrak.” [Online]. Available: <https://celestrak.com/>. [Accessed: 18-Aug-2018].

- [81] J. J. Pocha, "Orbit Propagation," in *An Introduction to Mission Design for Geostationary Satellites*, Springer, 1987, pp. 138–163.
- [82] S. P. Shuster, "A Survey and Performance Analysis of Orbit Propagators for LEO, GEO, and Highly Elliptical Orbits," 2017.
- [83] R. R. Bate, D. D. Mueller, and J. E. White, *Fundamentals of astrodynamics*. New York: Dover Publications, 1971.
- [84] F. R. Hoots and R. Roehrich, "Models for Propagation of NORAD Element Sets. Spacetrack Report no. 3.," U.S. Air Force: Aerospace Defense Command, 1980.
- [85] "First-Hand:Lessons Learned from Six Decades of Spacecraft Guidance and Control Experiences - Engineering and Technology History Wiki." [Online]. Available: https://ethw.org/First-Hand:Lessons_Learned_from_Six_Decades_of_Spacecraft_Guidance_and_Control_Experiences. [Accessed: 19-Aug-2018].
- [86] N. K. Pavlis, S. A. Holmes, S. C. Kenyon, and J. K. Factor, "The development and evaluation of the Earth Gravitational Model 2008 (EGM2008)," *J. Geophys. Res. Solid Earth*, vol. 117, no. B4, p. n/a-n/a, Apr. 2012.
- [87] J. S. Parker, "ASEN 5050 Spaceflight Dynamics: Solar Radiation Pressure," University of Colorado, Boulder.
- [88] F. L. Markley and J. L. Crassidis, *Fundamentals of spacecraft attitude determination and control*. New York: Springer, 2014.
- [89] N. V. Earth, "Browse by Collection: Blue Marble," 11-Aug-2009. [Online]. Available: https://visibleearth.nasa.gov/view_cat.php?categoryID=1484. [Accessed: 19-Aug-2018].
- [90] R. W. Smith, *Department of Defense World Geodetic System 1984: its definition and relationships with local geodetic systems*. Defense Mapping Agency, 1987.
- [91] E. Thébault *et al.*, "International Geomagnetic Reference Field: the 12th generation," *Earth Planets Space*, vol. 67, no. 1, p. 79, May 2015.
- [92] "JPL Planetary and Lunar Ephemerides." [Online]. Available: https://ssd.jpl.nasa.gov/?planet_eph_export. [Accessed: 22-Aug-2018].
- [93] A. F. Heaton, A. Braafladt, and A. B. Artusio-Glimpse, "Validation of Solar Sail Simulations for the NASA Solar Sail Demonstration Project," in *AIAA SPACE 2014 Conference and Exposition*, 2014, p. 4207.
- [94] "Space-Track.Org." [Online]. Available: <https://www.space-track.org/auth/login>. [Accessed: 23-Aug-2018].
- [95] "Home." [Online]. Available: <https://www.thehumanitystar.com/>. [Accessed: 23-Aug-2018].
- [96] A. K. | P. Friday, March 23, and 2018, "The demise of (the) Humanity (Star)," *Astronomy.com*. [Online]. Available: <http://www.astronomy.com/news/2018/03/the-demise-of-the-humanity-star>. [Accessed: 23-Aug-2018].

Appendix A: Symbols, Notation, Constants, Acronyms, and Definitions

This appendix defines notation and constants in this thesis and the simulation it describes. The notation used for symbols is first defined, specifically as this pertains to subscripts and superscripts, as well as for vectors and unit vectors. Afterwards, the symbol, value, units and description of constants used in this thesis are listed.

A.1: Notation

A.1.1: Subscripts and Superscripts

Symbols throughout this thesis have both subscripts and superscripts that provide some information about the symbol. Superscripts define the reference frame the variable is defined within, while subscripts will contain some description as shown in Figure 27.

\vec{r} *Reference Frame*
Description

Figure 27: Superscript and subscript notation standard

Some representative examples are shown in Equation 3.

$$\begin{array}{ccc} \vec{r}_{IB}^B & \vec{r}_{S6}^B & A_4 \\ \text{(a)} & \text{(b)} & \text{(c)} \end{array}$$

Equation 3: Subscript and superscript notation examples. (a) Position vector of B with respect to I in B-frame coordinates, (b) position vector of surface #6 in the B-frame, and (c) the Area of #4

In cases such as Equation 3 (b) where it's not clear where the starting point is, assume it is at the origin of the reference frame unless otherwise stated.

A.1.2: Vectors and Unit Vectors

Vectors and unit vectors used throughout this thesis will use the notation defined for a generic vector shown in Equation 4.

$$\begin{array}{cc} \vec{r} & \hat{r} \\ \text{(a)} & \text{(b)} \end{array}$$

Equation 4: Vector notation: (a) Vector and (b) unit vector

A.2: Constants

Table 21 lists the constants used throughout the thesis and simulation.

Table 21: Constants

Symbol	Units	Value	Description
c	$\frac{\text{m}}{\text{s}}$	2.99792458×10^8	Speed of Light in a Vacuum
r_e	m	6.3781366×10^6	Earth's Equatorial Radius
μ_e	$\frac{\text{m}^3}{\text{s}^2}$	$3.986004356 \times 10^{14}$	Earth's Gravitational Parameter
μ_L	$\frac{\text{m}^3}{\text{s}^2}$	$4.90280015 \times 10^{12}$	Lunar Gravitational Parameter
μ_S	$\frac{\text{m}^3}{\text{s}^2}$	$1.32712440041 \times 10^{20}$	Sol's Gravitational Parameter
ω_e	$\frac{\text{rad}}{\text{s}}$	7.292×10^{-5}	Earth's rotation rate

Appendix B: Validation Graphs

B.1: TLE #1

B.1.1: Two Body Gravity

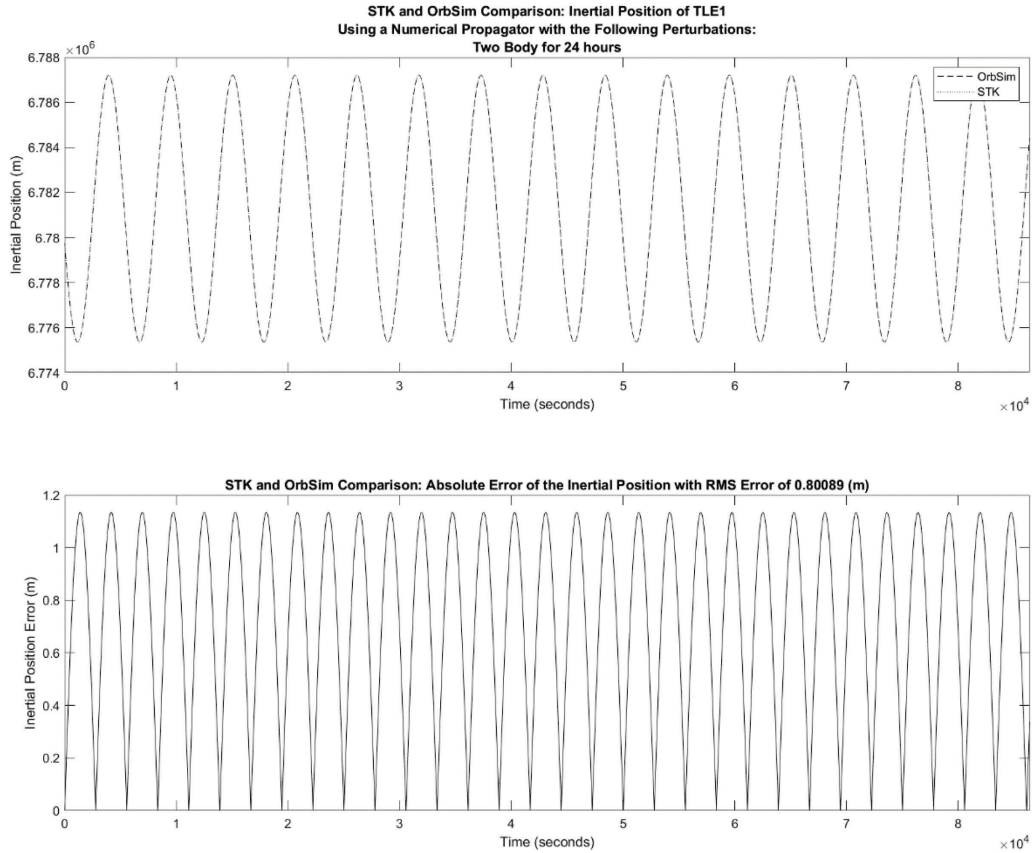


Figure 28: Inertial Position Comparison of the Satellite from TLE#1 with Two Body Gravity

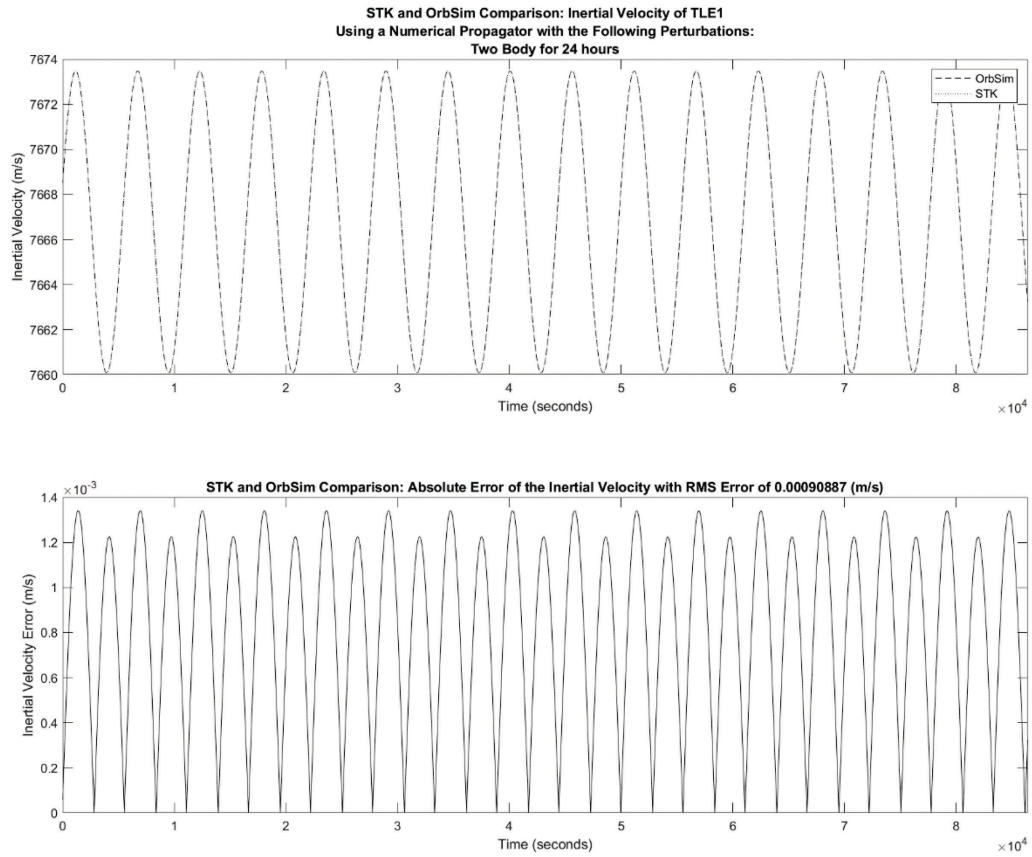


Figure 29: Inertial Velocity Comparison of the Satellite from TLE#1 with Two Body Gravity

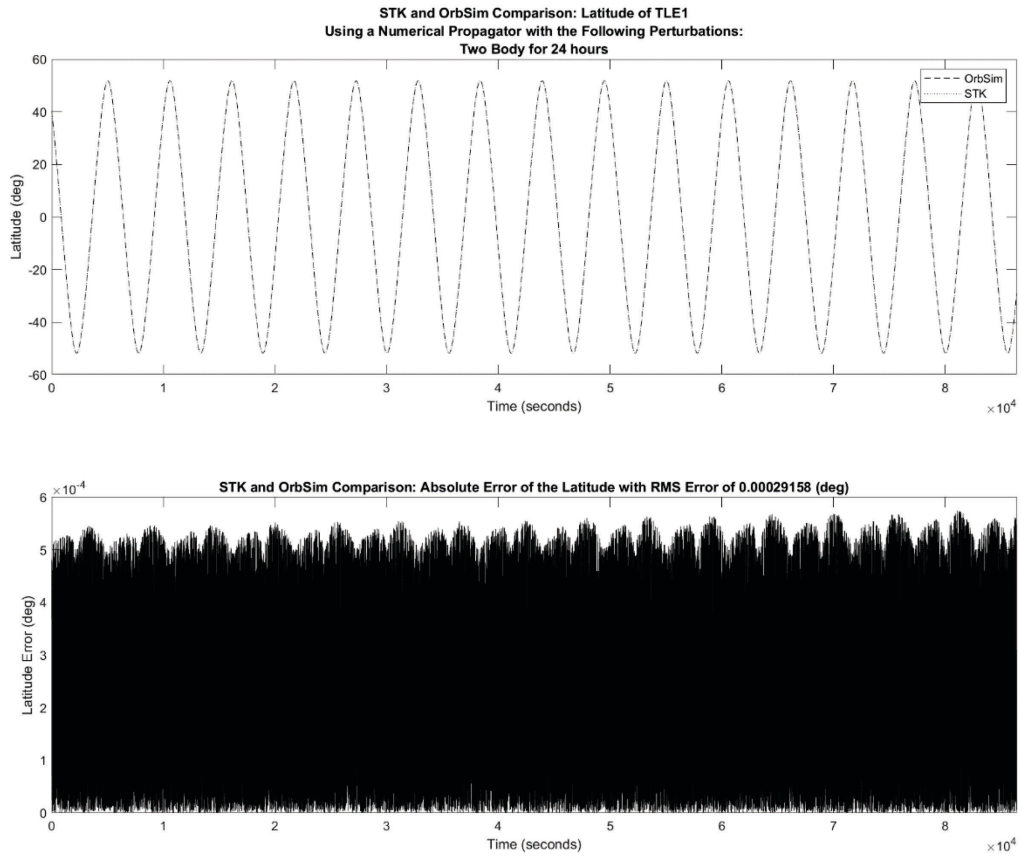


Figure 30: Latitude Comparison of the Satellite from TLE#1 with Two Body Gravity

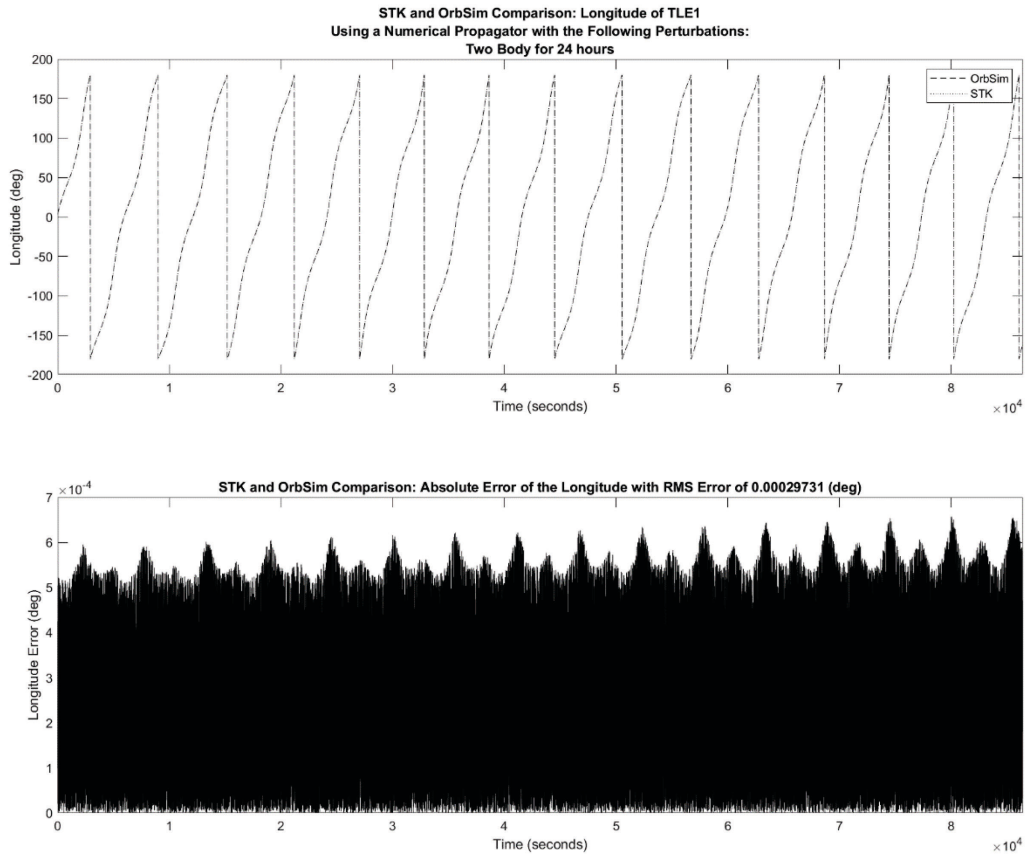


Figure 31: Longitude Comparison of the Satellite from TLE#1 with Two Body Gravity

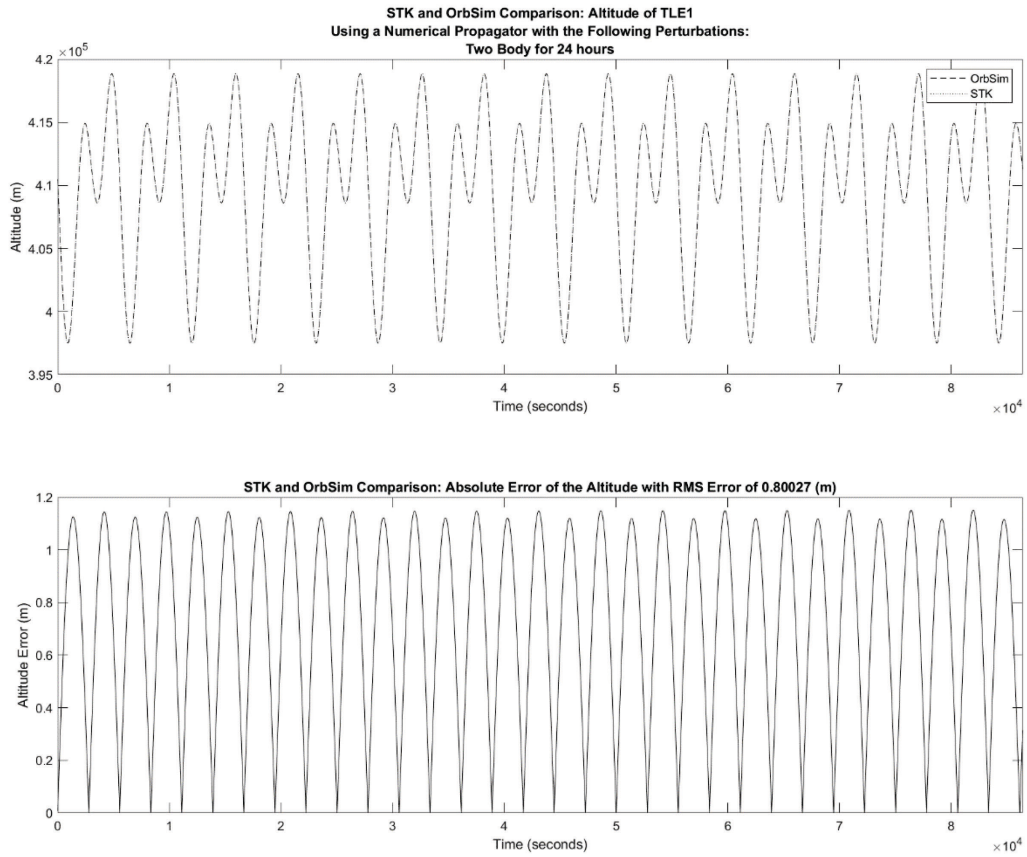


Figure 32: Altitude Comparison of the Satellite from TLE#1 with Two Body Gravity

B.1.2: Spherical Harmonic Gravity

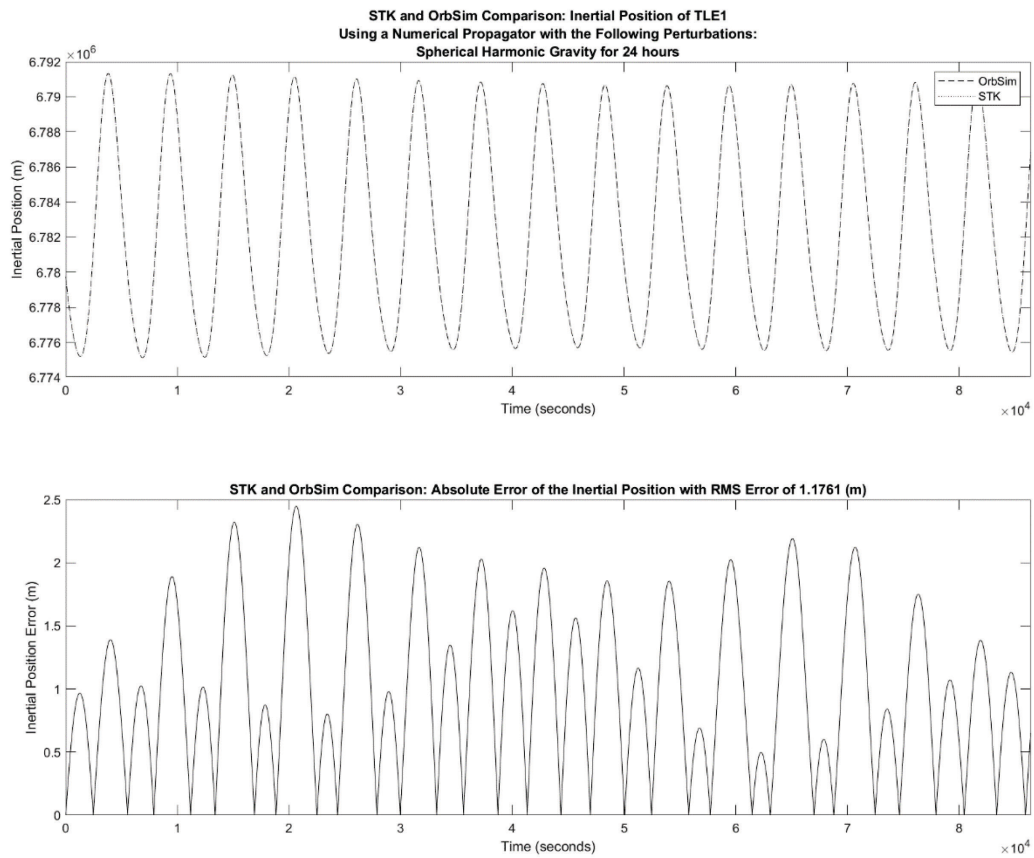


Figure 33: Inertial Position Comparison of the Satellite from TLE#1 with Spherical Harmonic Gravity

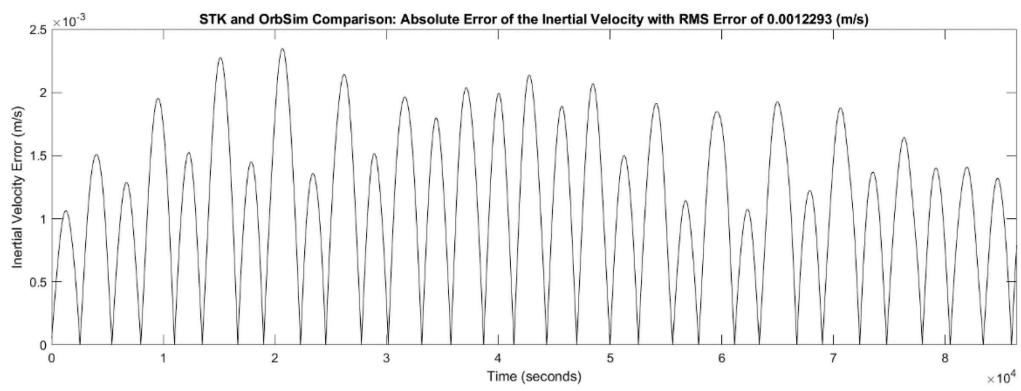
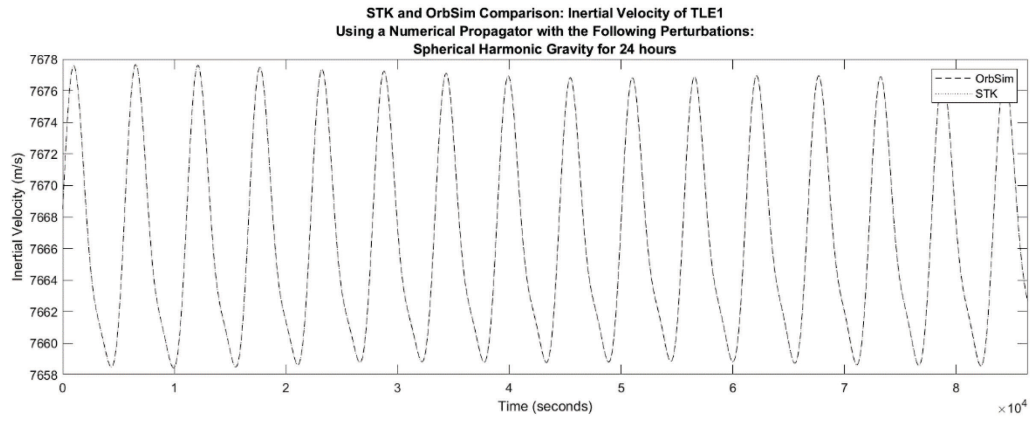


Figure 34: Inertial Velocity Comparison of the Satellite from TLE#1 with Spherical Harmonic Gravity

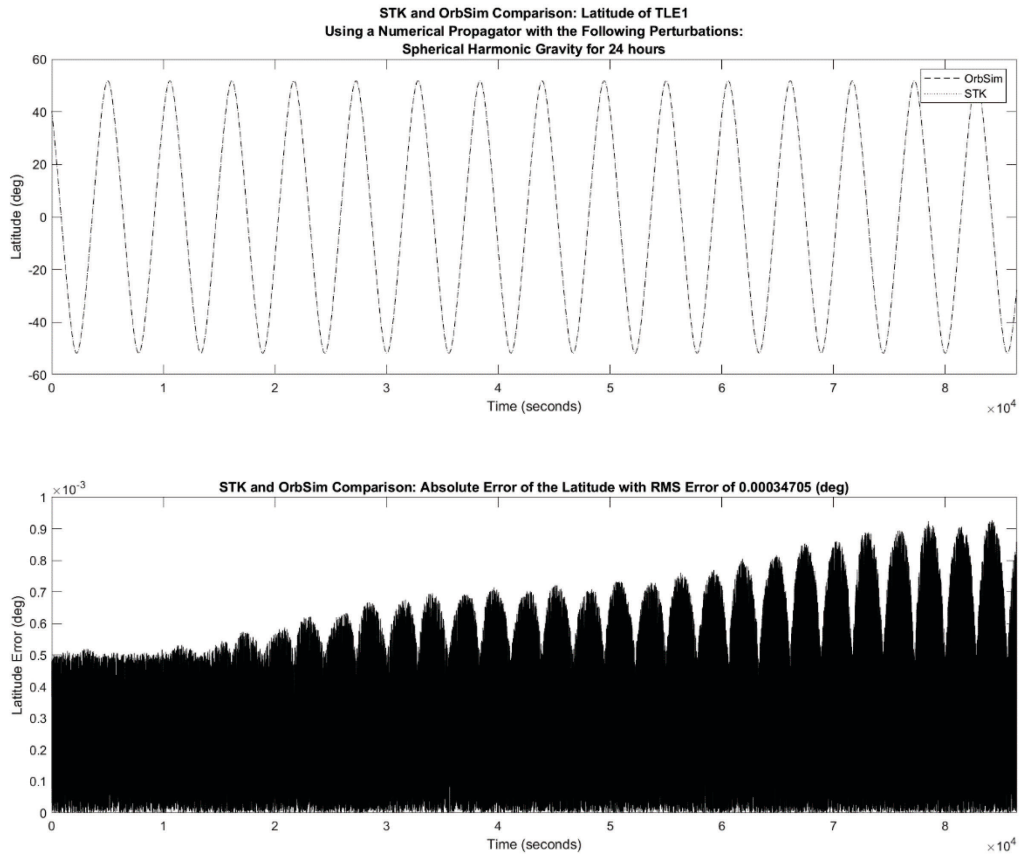


Figure 35: Latitude Comparison of the Satellite from TLE#1 with Spherical Harmonic Gravity

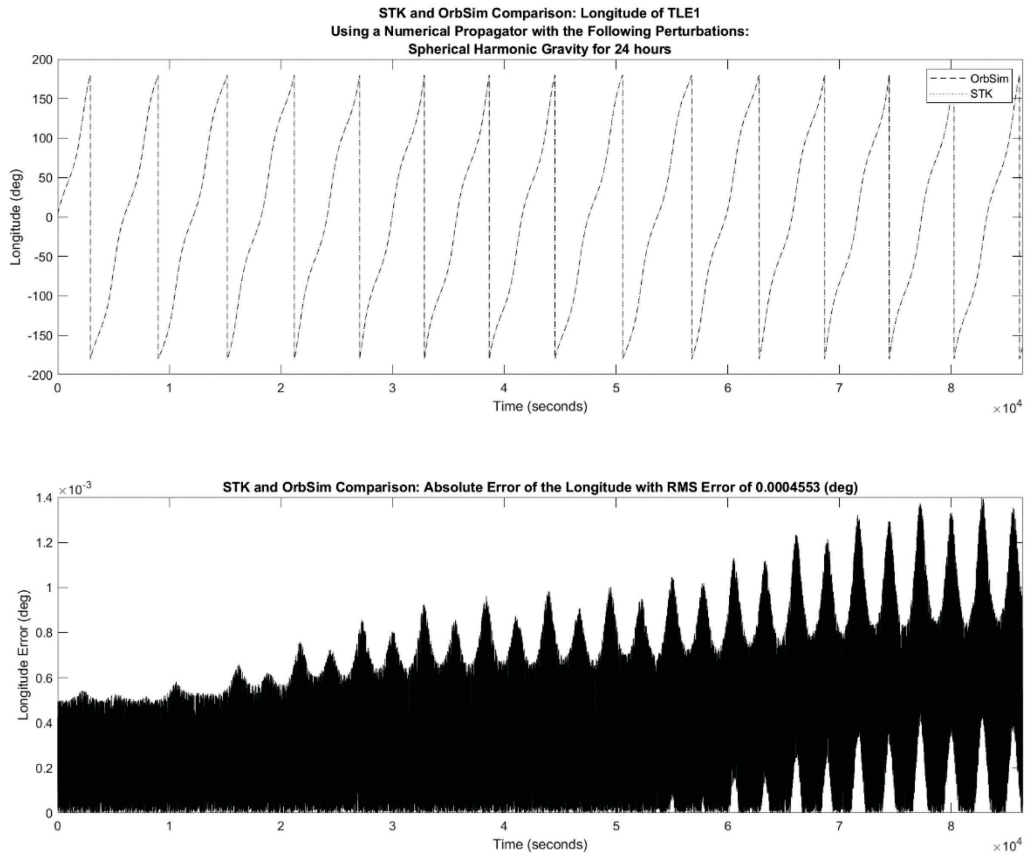


Figure 36: Longitude Comparison of the Satellite from TLE#1 with Spherical Harmonic Gravity

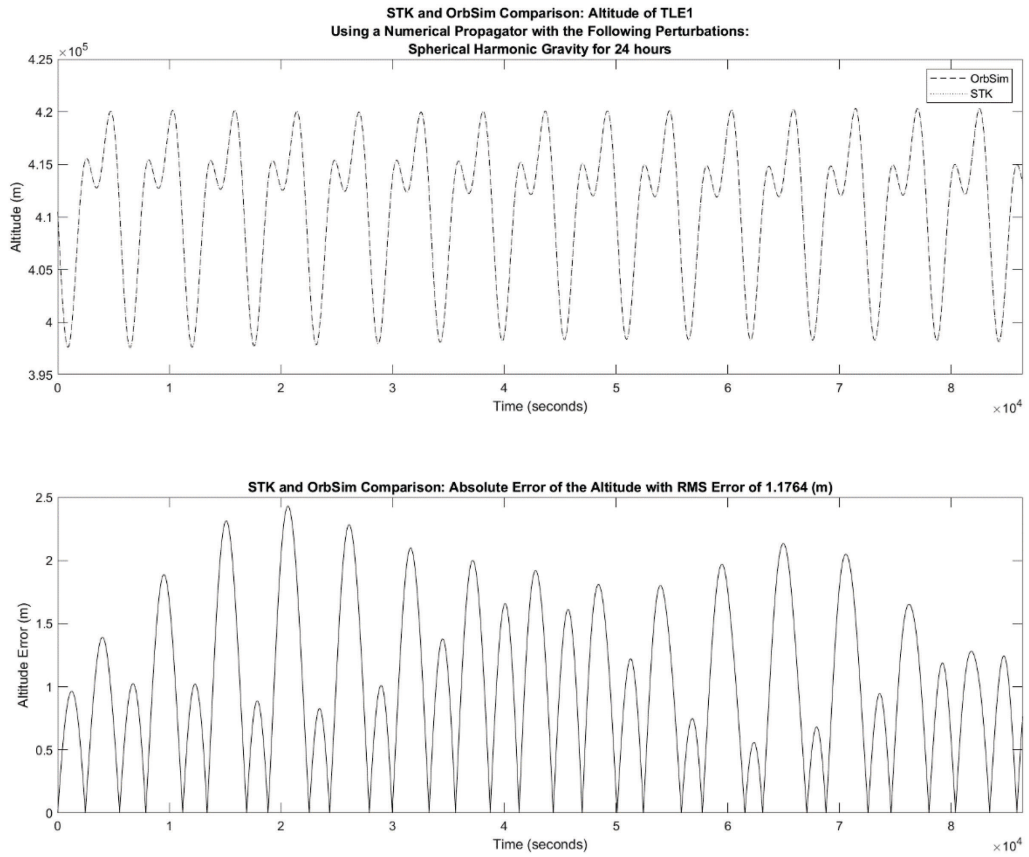


Figure 37: Altitude Comparison of the Satellite from TLE#1 with Spherical Harmonic Gravity

B.1.3: Spherical Harmonic Gravity & Solar gravity

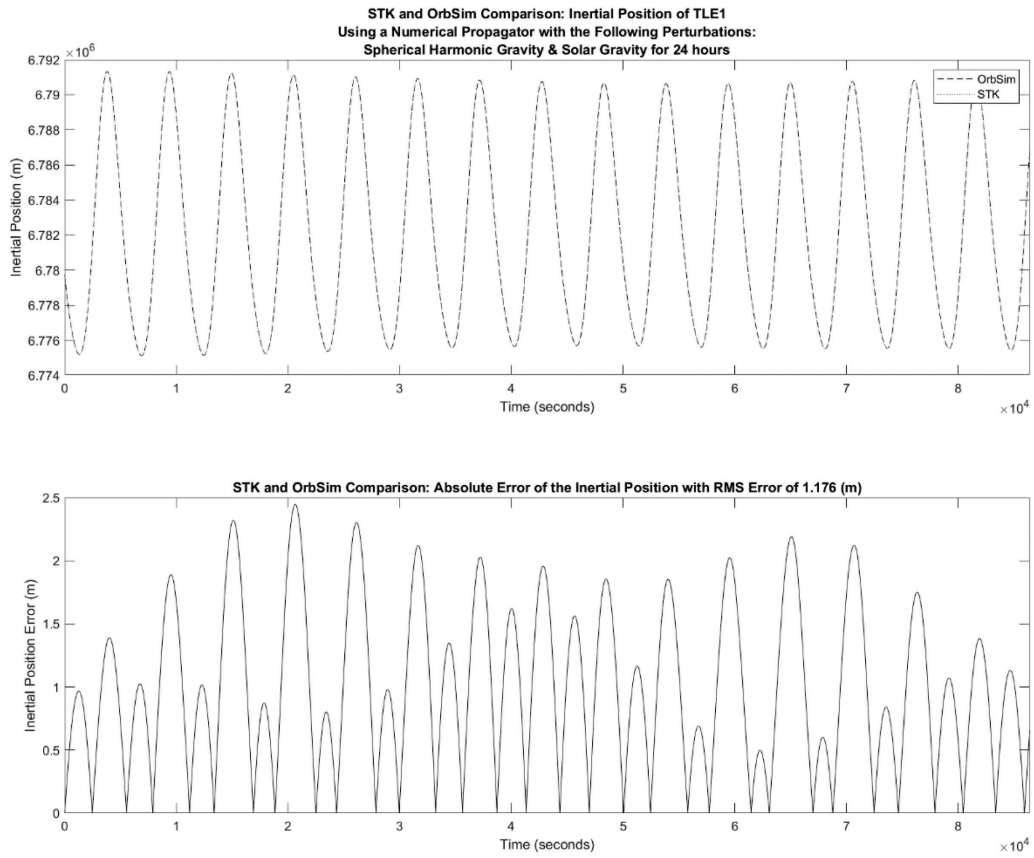


Figure 38: Inertial Position Comparison of the Satellite from TLE#1 with Spherical Harmonic Gravity and Solar Gravity

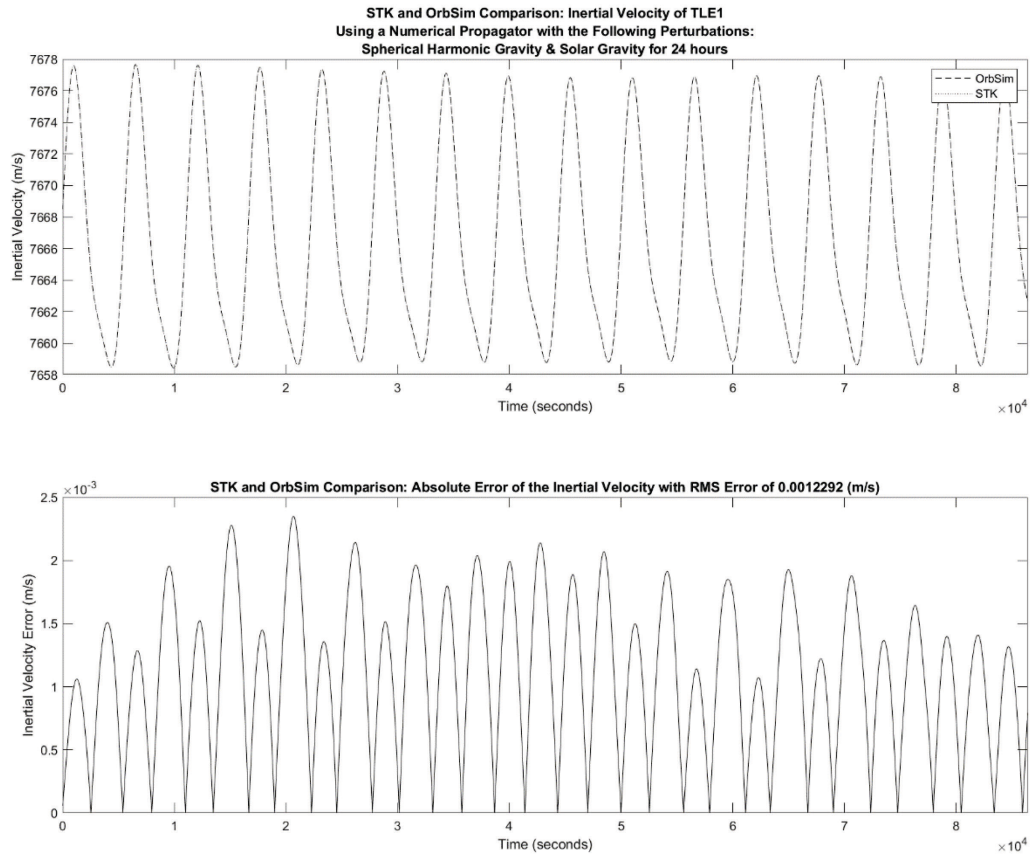


Figure 39: Inertial Velocity Comparison of the Satellite from TLE#1 with Spherical Harmonic Gravity and Solar Gravity

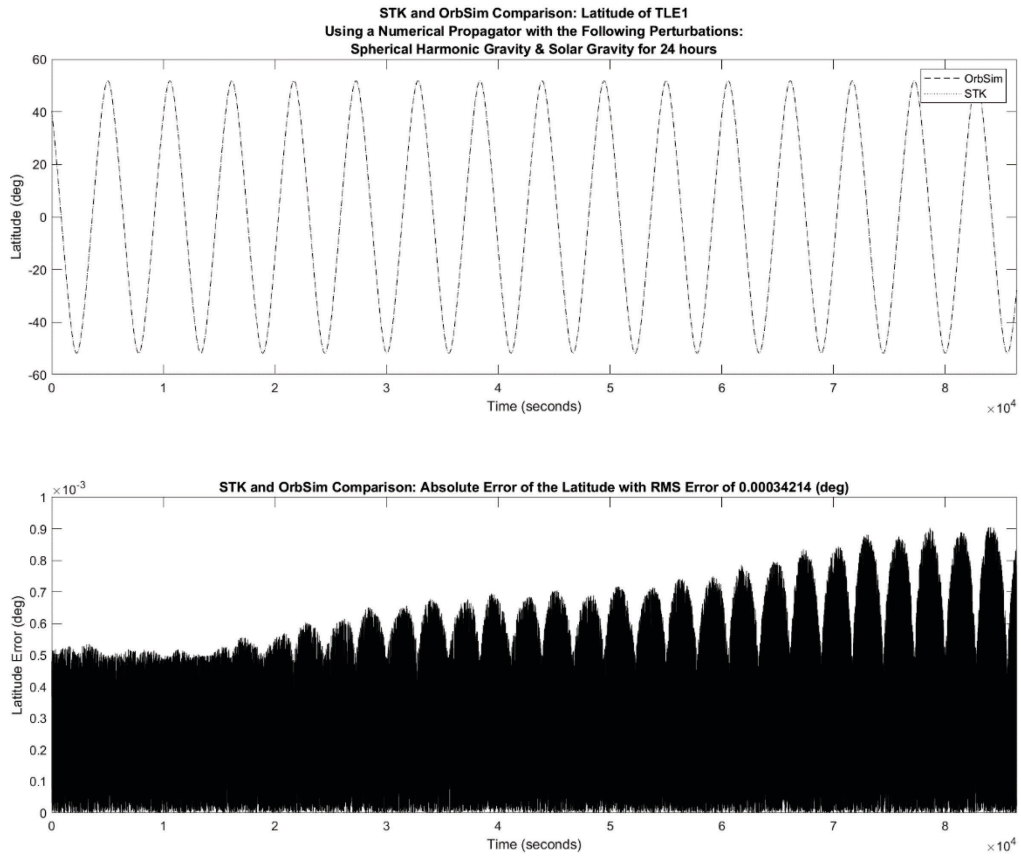


Figure 40: Latitude Comparison of the Satellite from TLE#1 with Spherical Harmonic Gravity and Solar Gravity

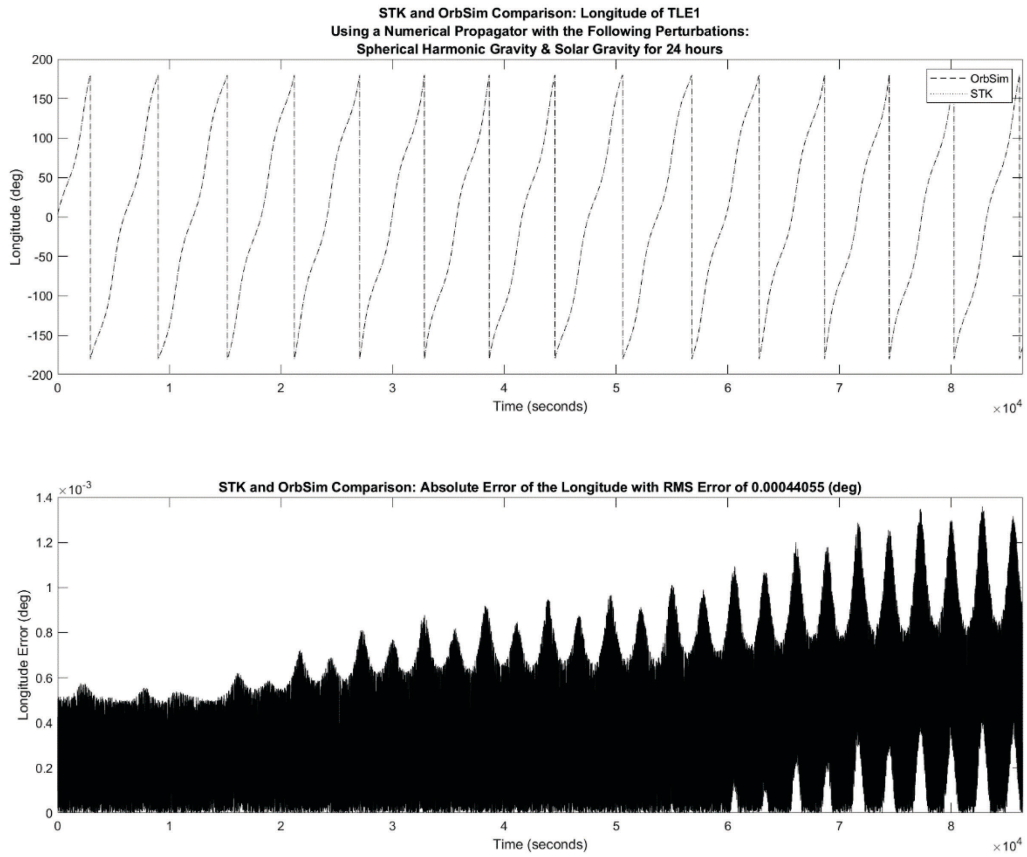


Figure 41: Longitude Comparison of the Satellite from TLE#1 with Spherical Harmonic Gravity and Solar Gravity

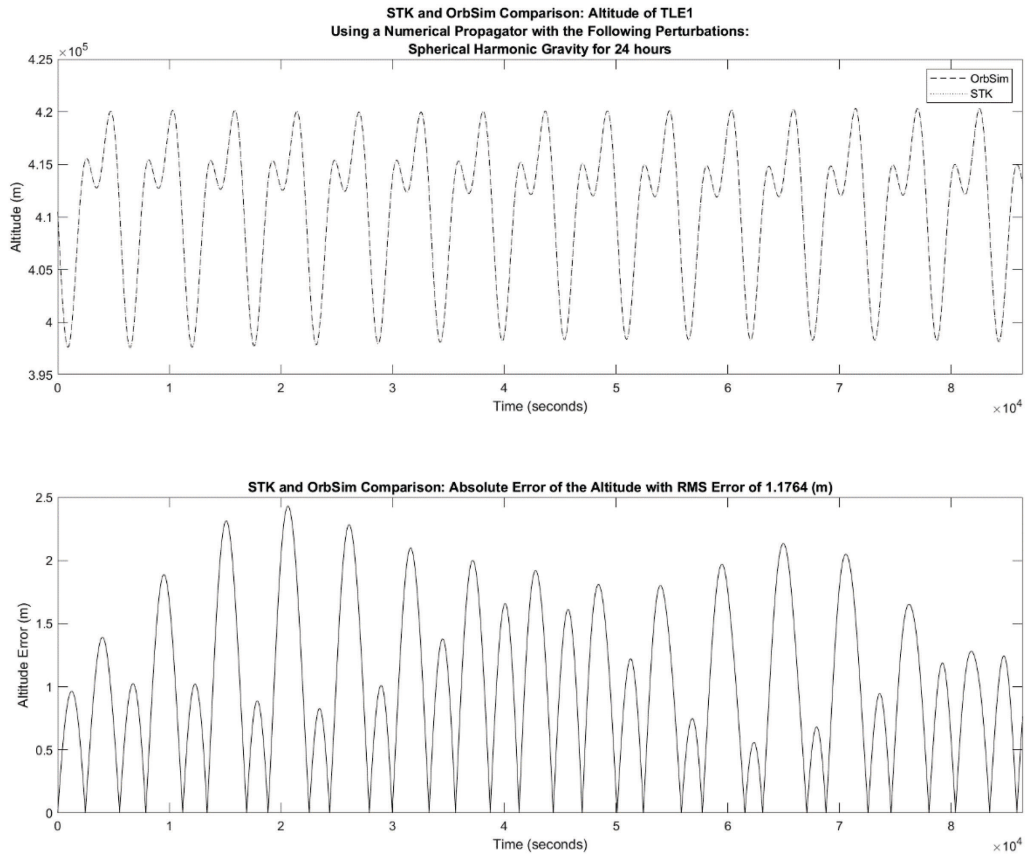


Figure 42: Altitude Comparison of the Satellite from TLE#1 with Spherical Harmonic Gravity and Solar Gravity

B.1.4: Spherical Harmonic Gravity & Lunar Gravity

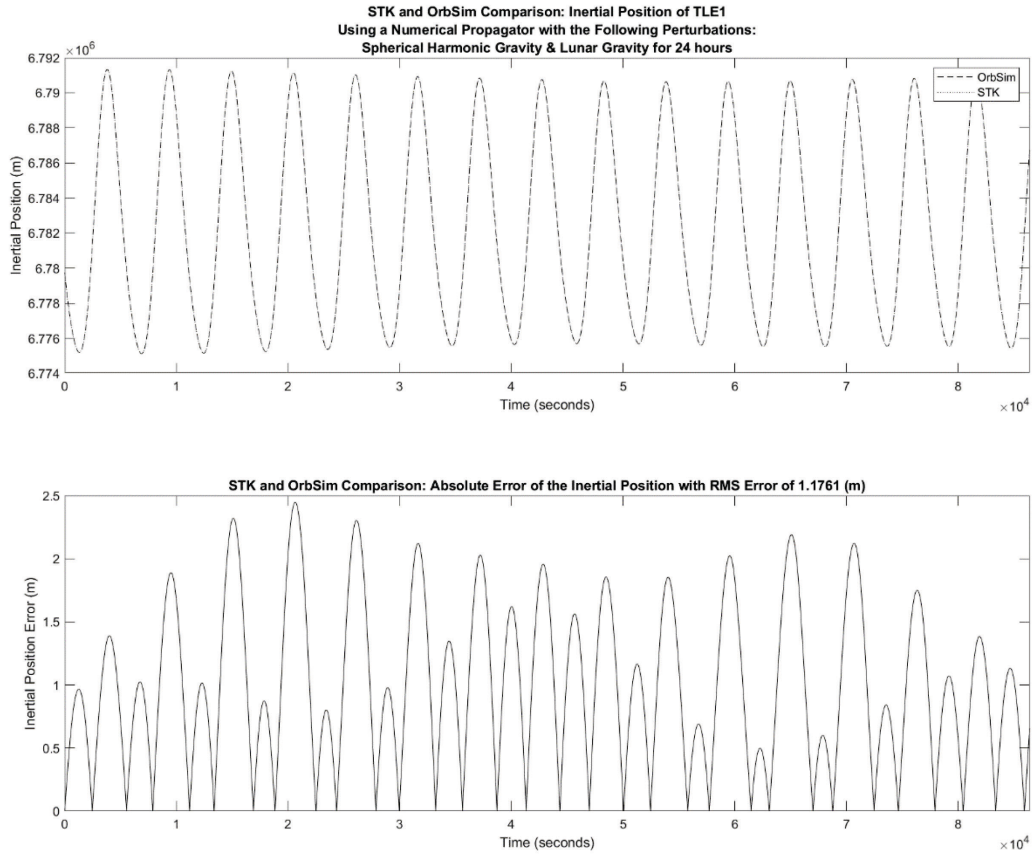


Figure 43: Inertial Position Comparison of the Satellite from TLE#1 with Spherical Harmonic Gravity and Lunar Gravity

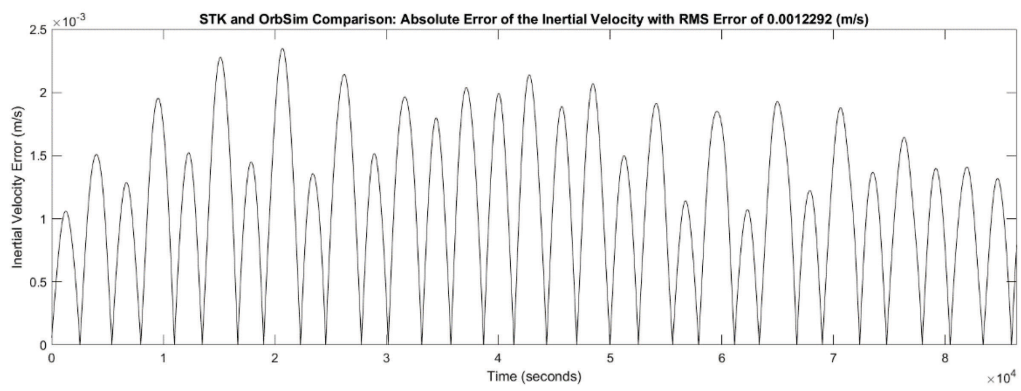
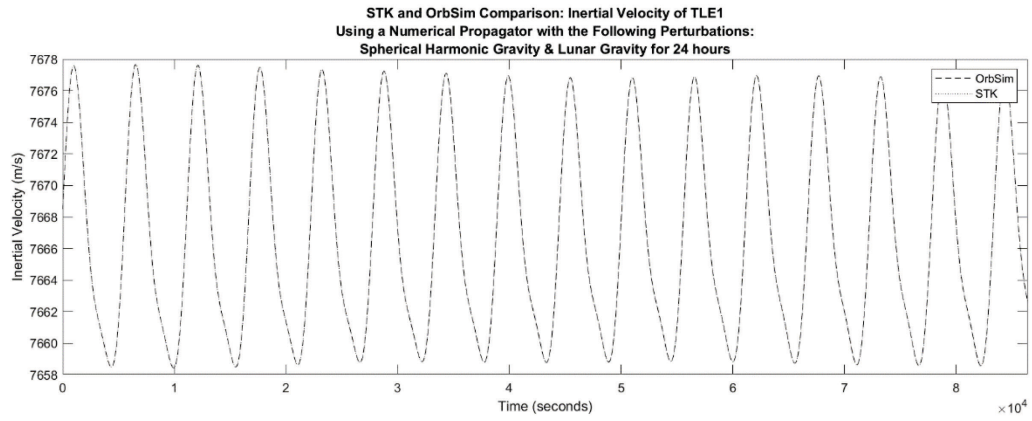


Figure 44: Inertial Velocity Comparison of the Satellite from TLE#1 with Spherical Harmonic Gravity and Lunar Gravity

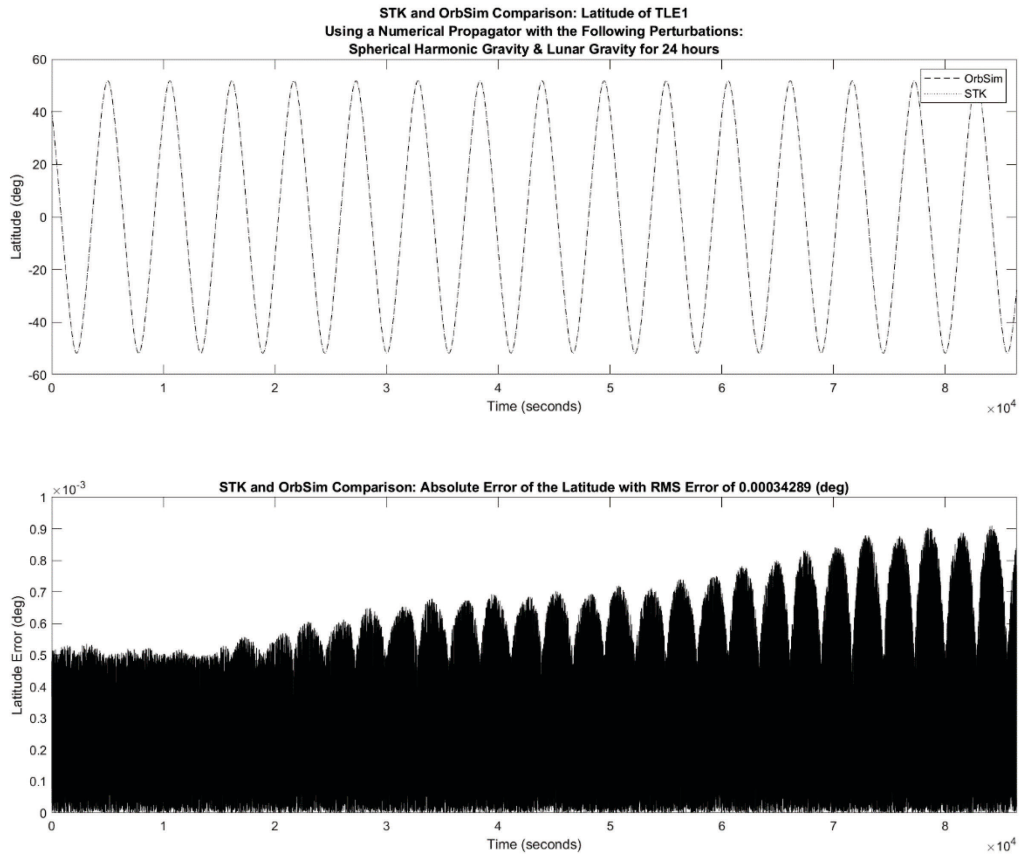


Figure 45: Inertial Latitude Comparison of the Satellite from TLE#1 with Spherical Harmonic Gravity and Lunar Gravity

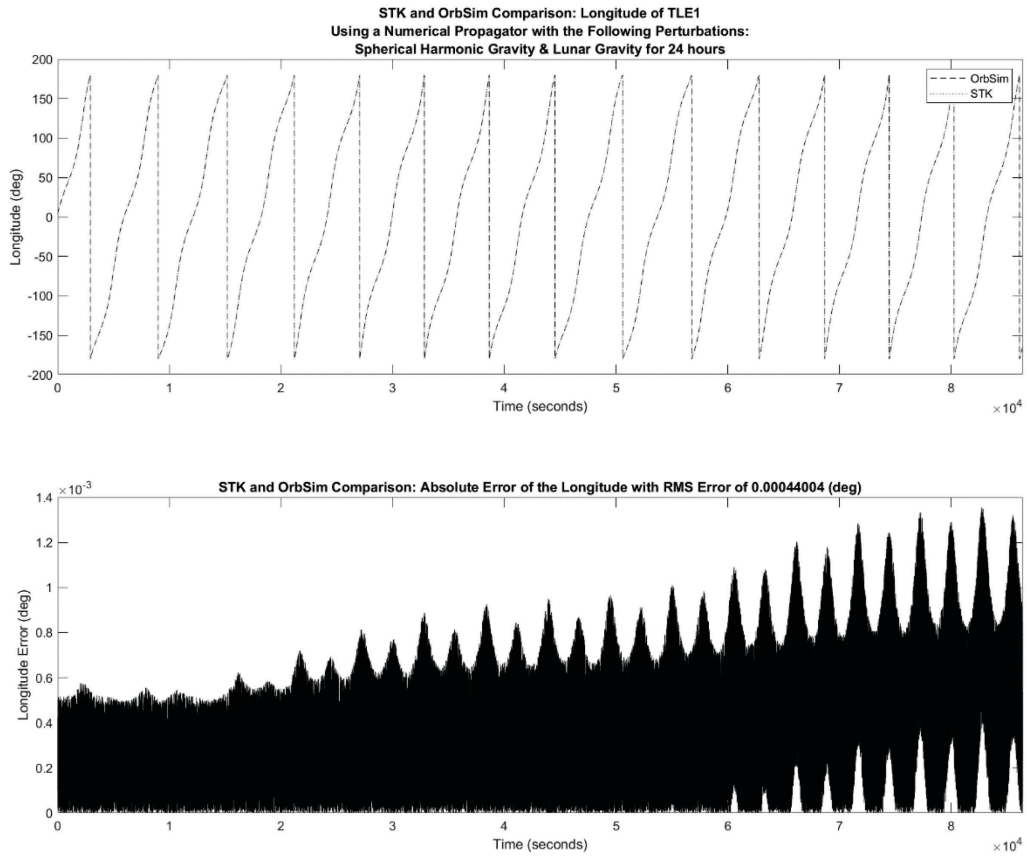


Figure 46: Longitude Comparison of the Satellite from TLE#1 with Spherical Harmonic Gravity and Lunar Gravity

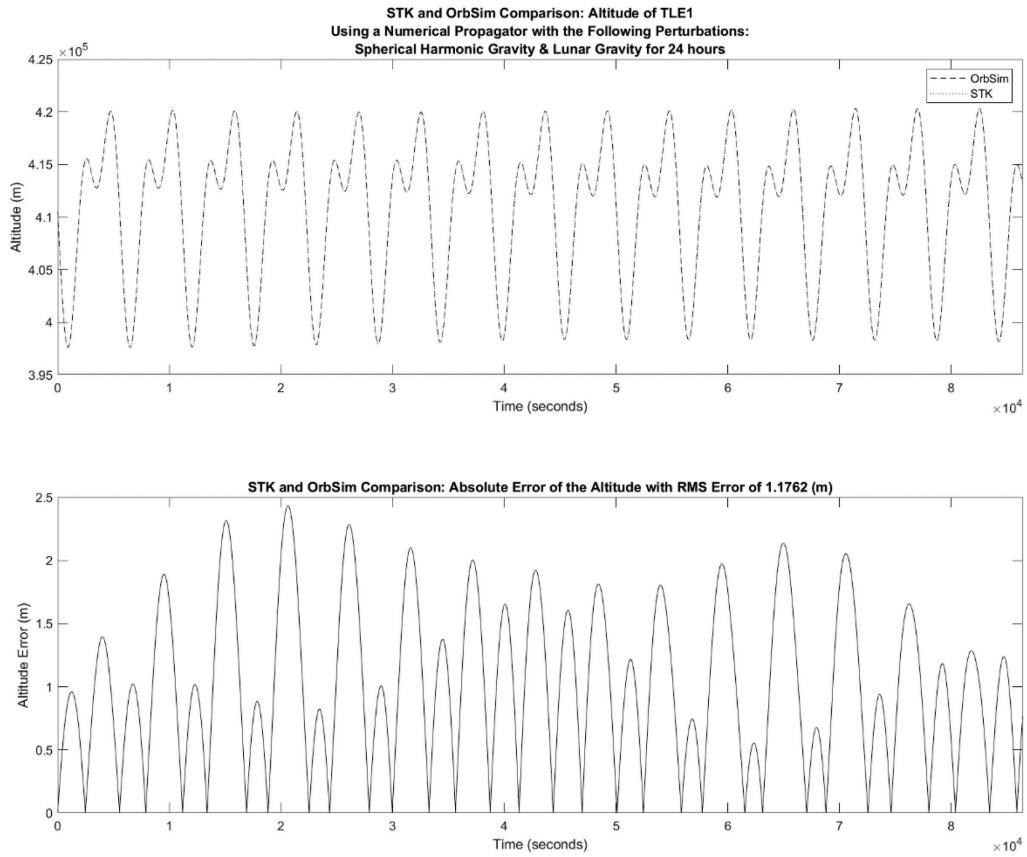


Figure 47: Altitude Comparison of the Satellite from TLE#1 with Spherical Harmonic Gravity and Lunar Gravity

B.1.5: Spherical Harmonic Gravity & Aerodynamic Drag

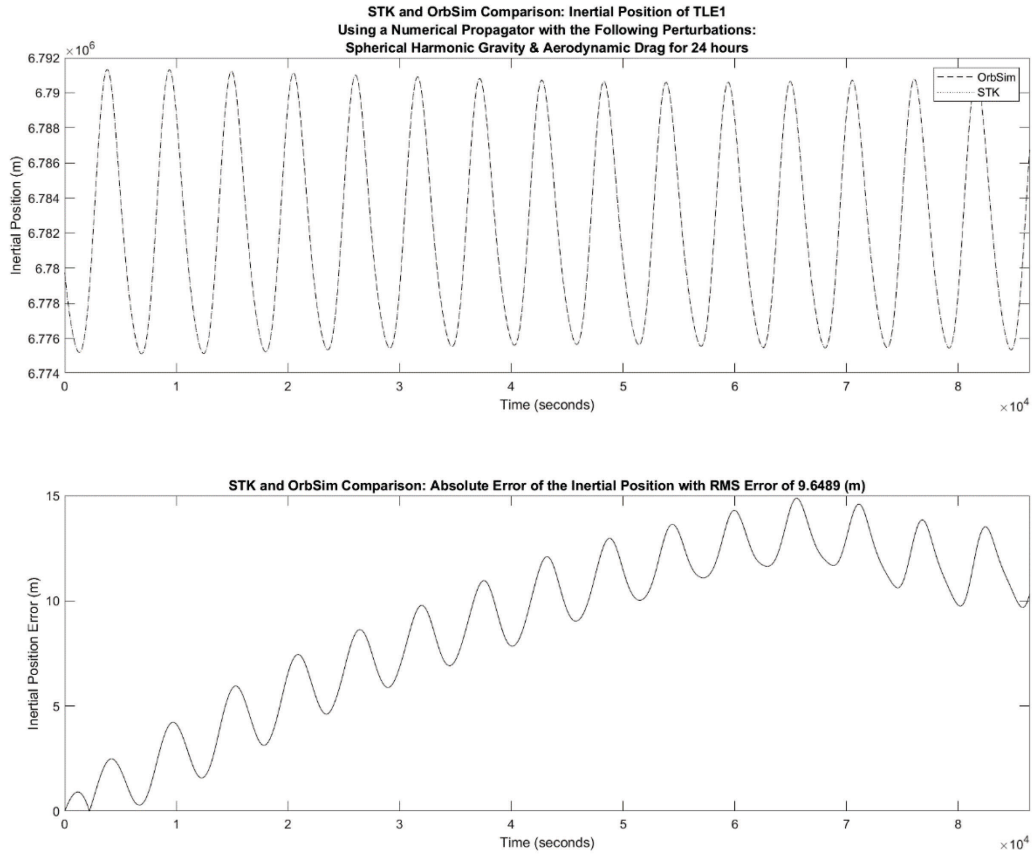


Figure 48: Inertial Position Comparison of the Satellite from TLE#1 with Spherical Harmonic Gravity and Aerodynamic Drag

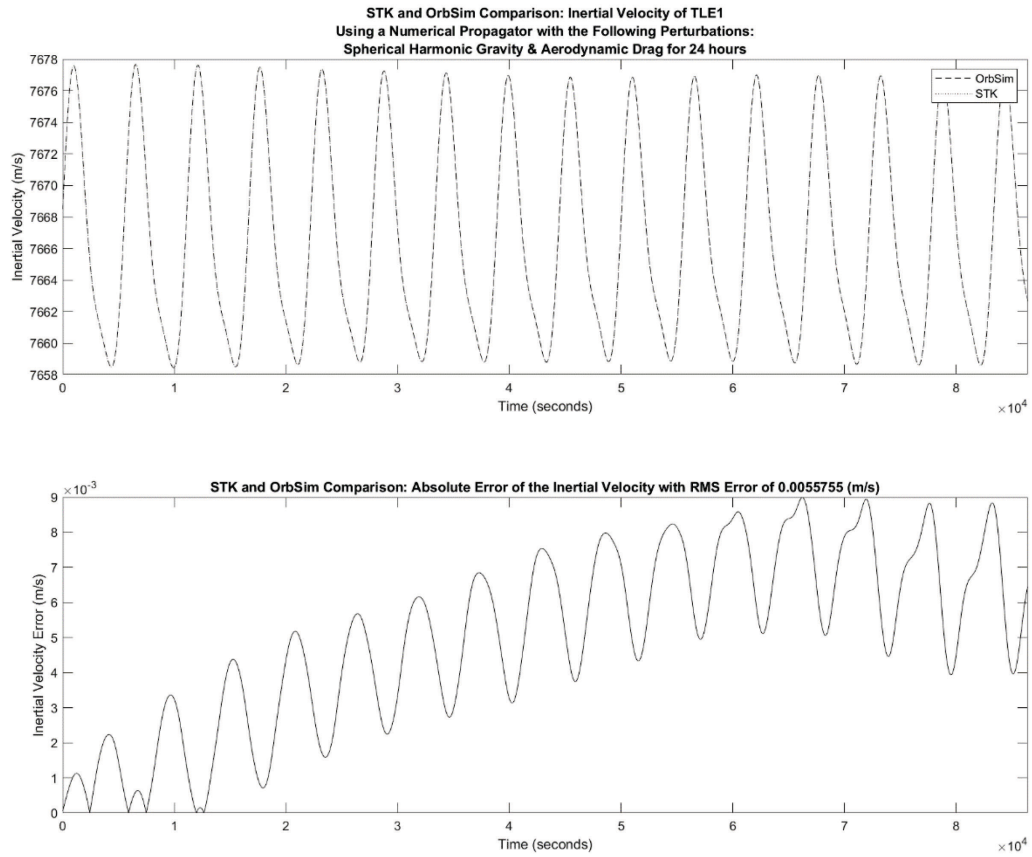


Figure 49: Inertial Velocity Comparison of the Satellite from TLE#1 with Spherical Harmonic Gravity and Aerodynamic Drag

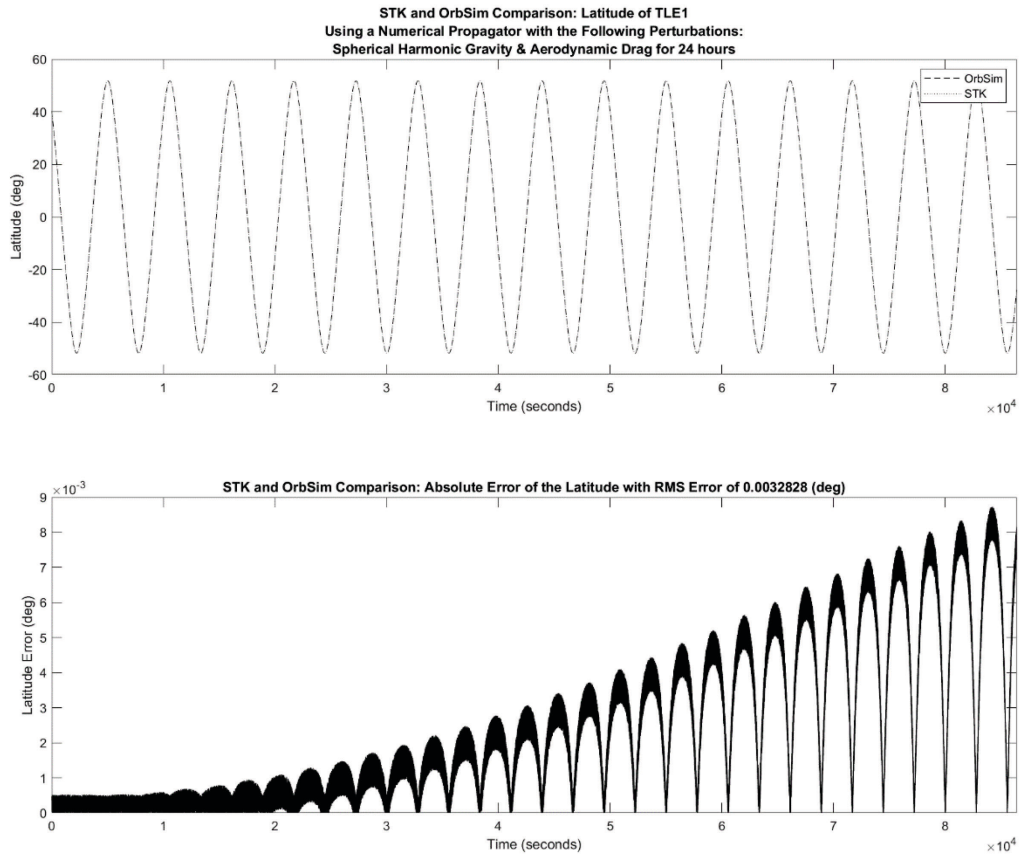


Figure 50: Latitude Comparison of the Satellite from TLE#1 with Spherical Harmonic Gravity and Aerodynamic Drag

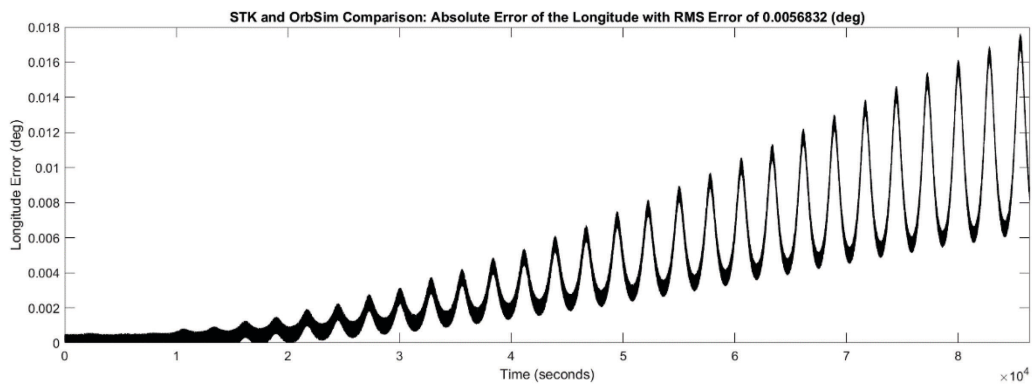
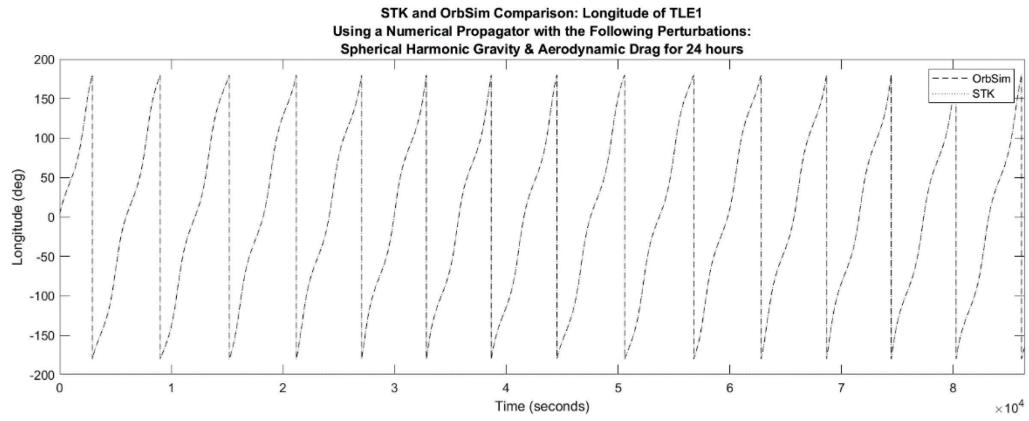


Figure 51: Longitude Comparison of the Satellite from TLE#1 with Spherical Harmonic Gravity and Aerodynamic Drag

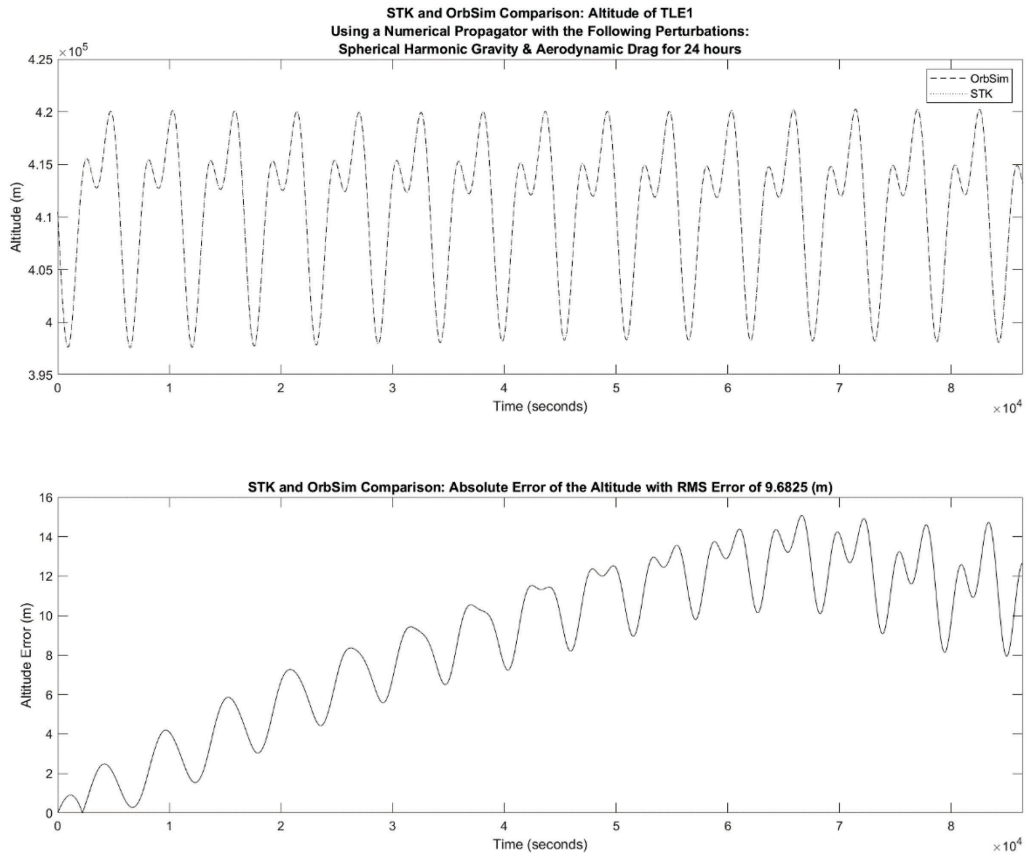


Figure 52: Altitude Comparison of the Satellite from TLE#1 with Spherical Harmonic Gravity and Aerodynamic Drag

B.1.6: Spherical Harmonic Gravity & Solar Pressure

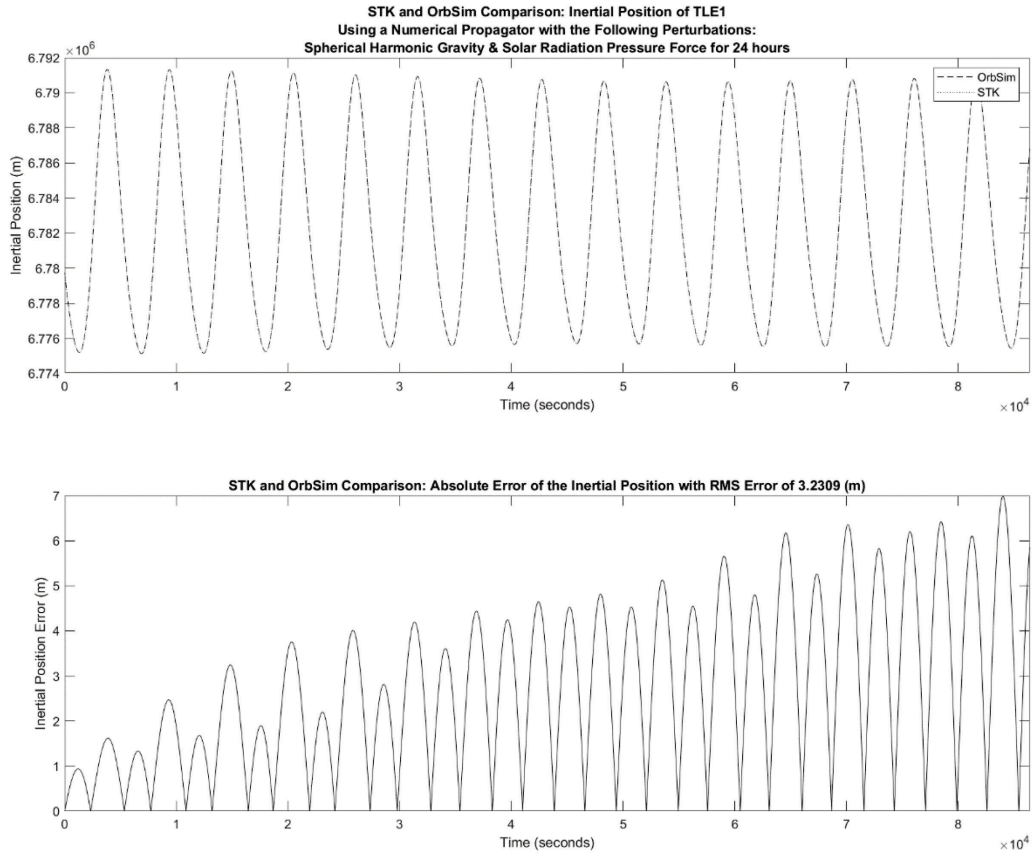


Figure 53: Inertial Position Comparison of the Satellite from TLE#1 with Spherical Harmonic Gravity and Solar Radiation Pressure

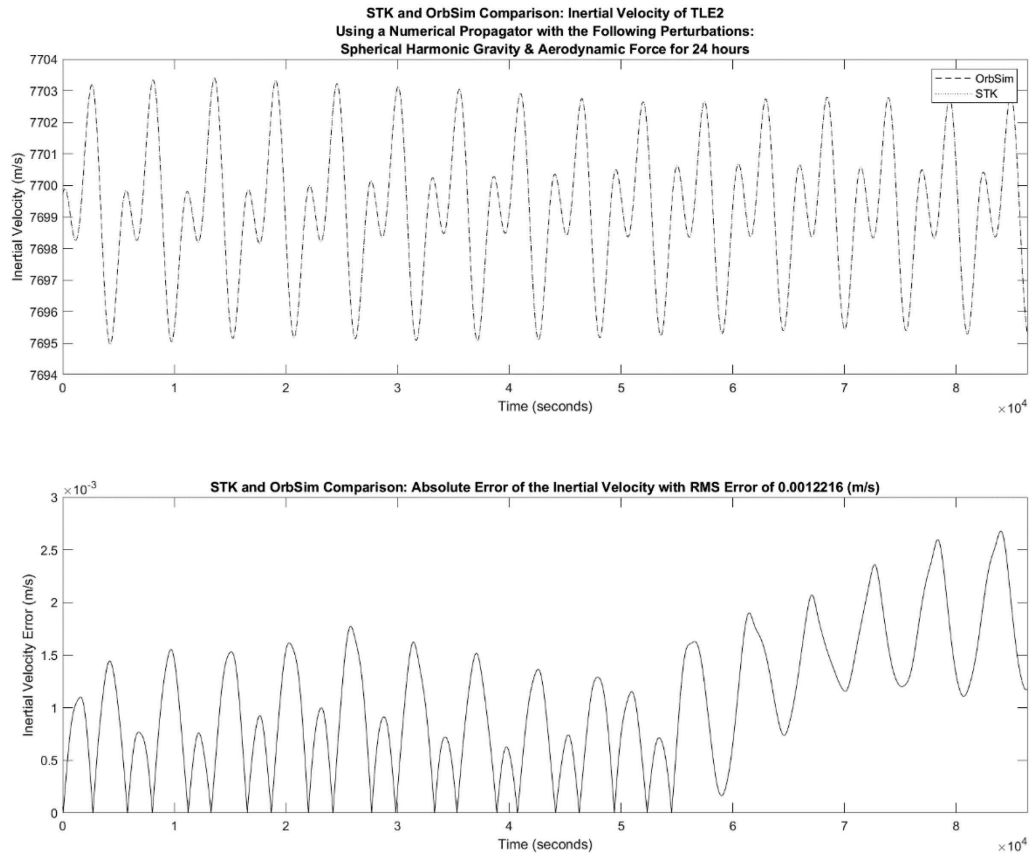


Figure 54: Inertial Velocity Comparison of the Satellite from TLE#1 with Spherical Harmonic Gravity and Solar Radiation Pressure

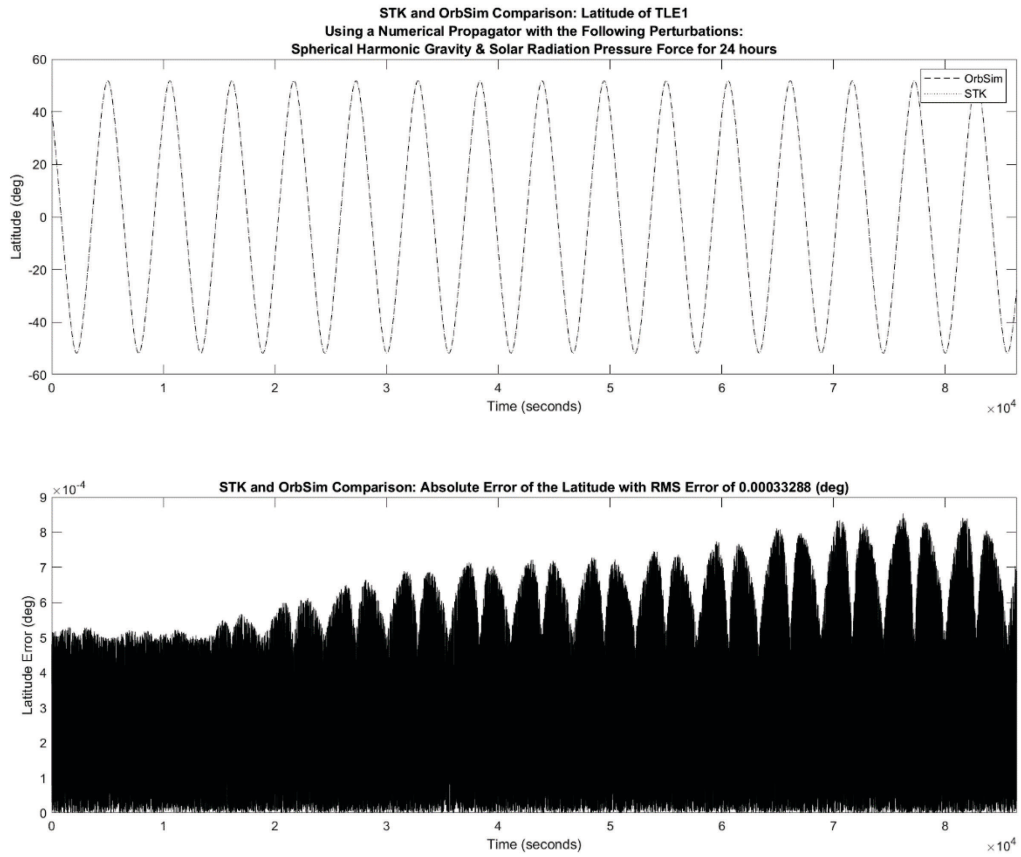


Figure 55: Latitude Comparison of the Satellite from TLE#1 with Spherical Harmonic Gravity and Solar Radiation Pressure

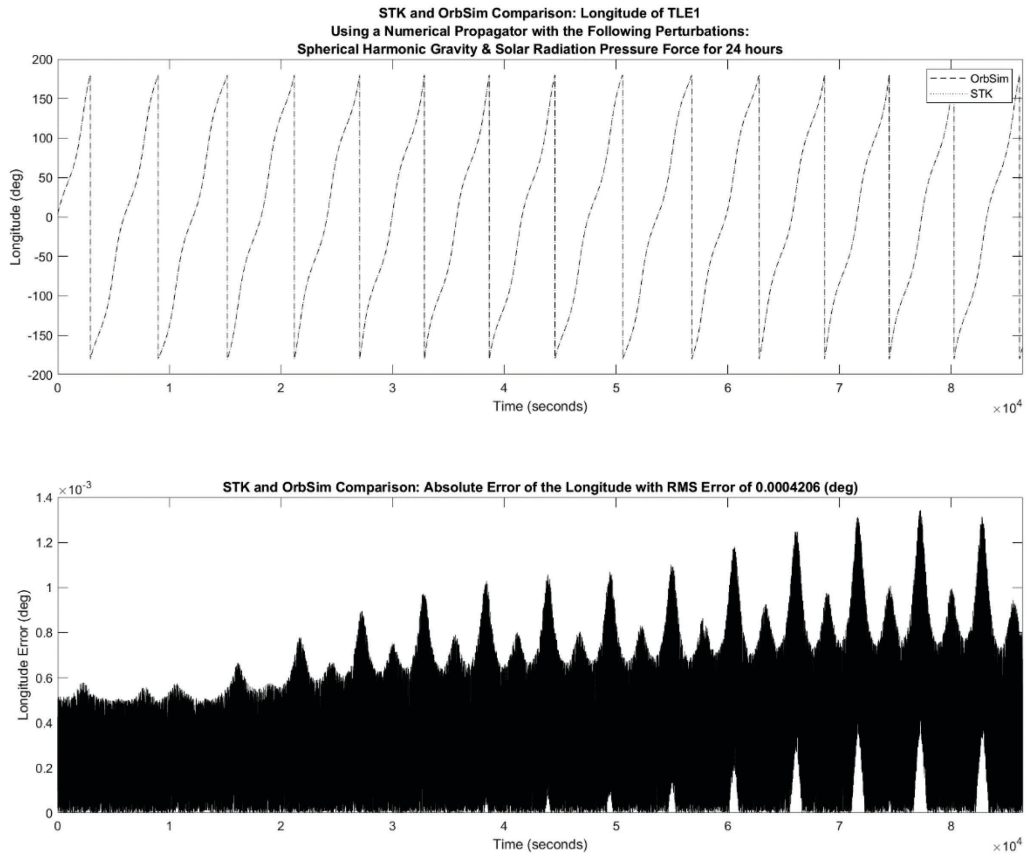


Figure 56: Longitude Comparison of the Satellite from TLE#1 with Spherical Harmonic Gravity and Solar Radiation Pressure

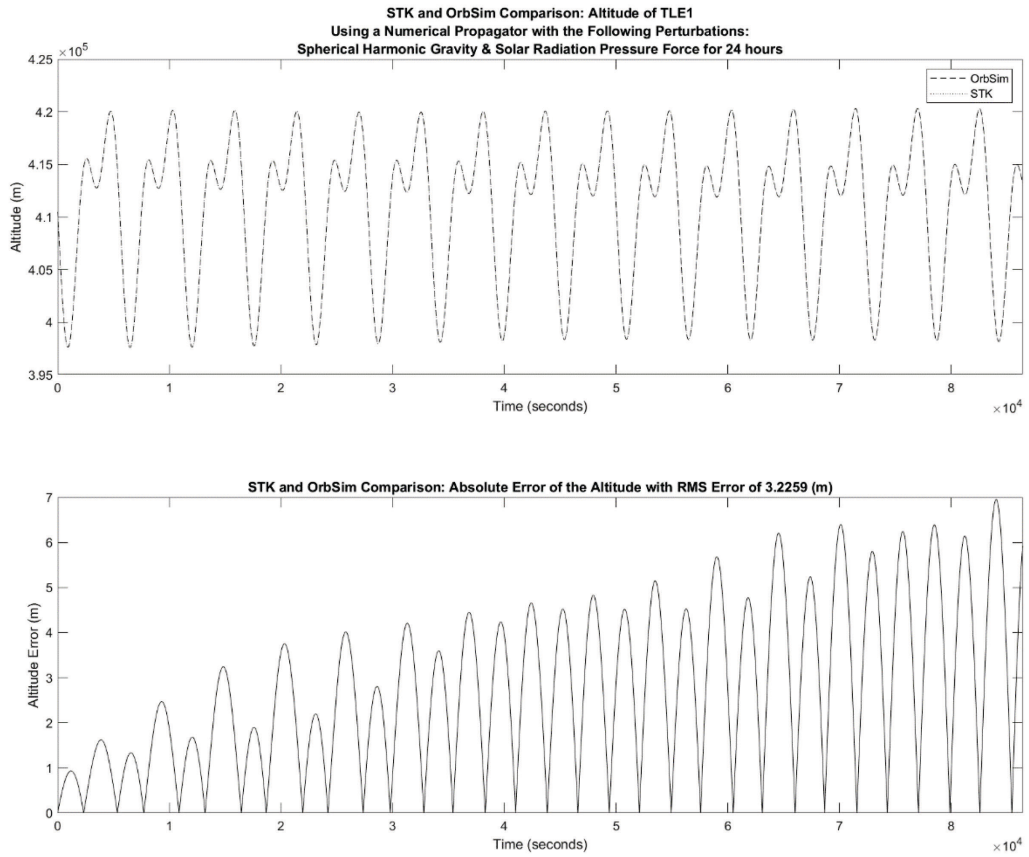


Figure 57: Altitude Comparison of the Satellite from TLE#1 with Spherical Harmonic Gravity and Solar Radiation Pressure

B.1.7: Spherical Harmonic Gravity, Solar Gravity, Lunar Gravity, Aerodynamic Drag and Solar Pressure

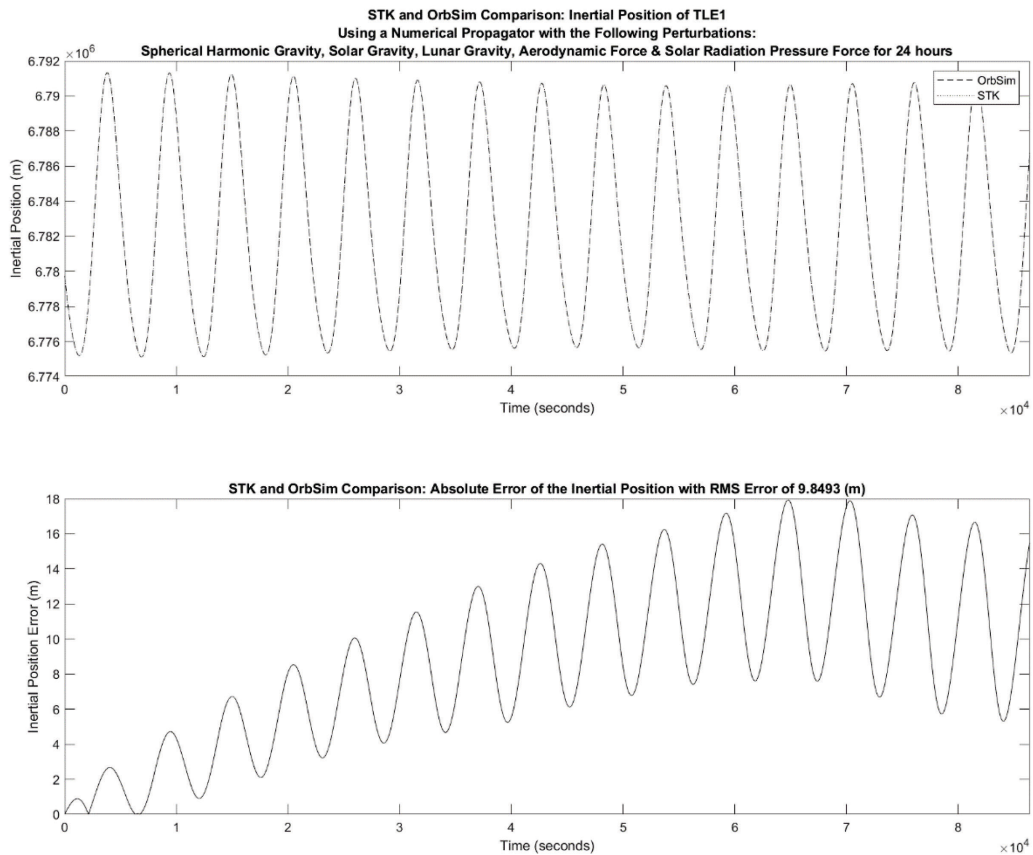


Figure 58: Inertial Position Comparison of the Satellite from TLE#1 with Spherical Harmonic Gravity, Solar Gravity, Lunar Gravity, Aerodynamic Force and Solar Radiation Pressure

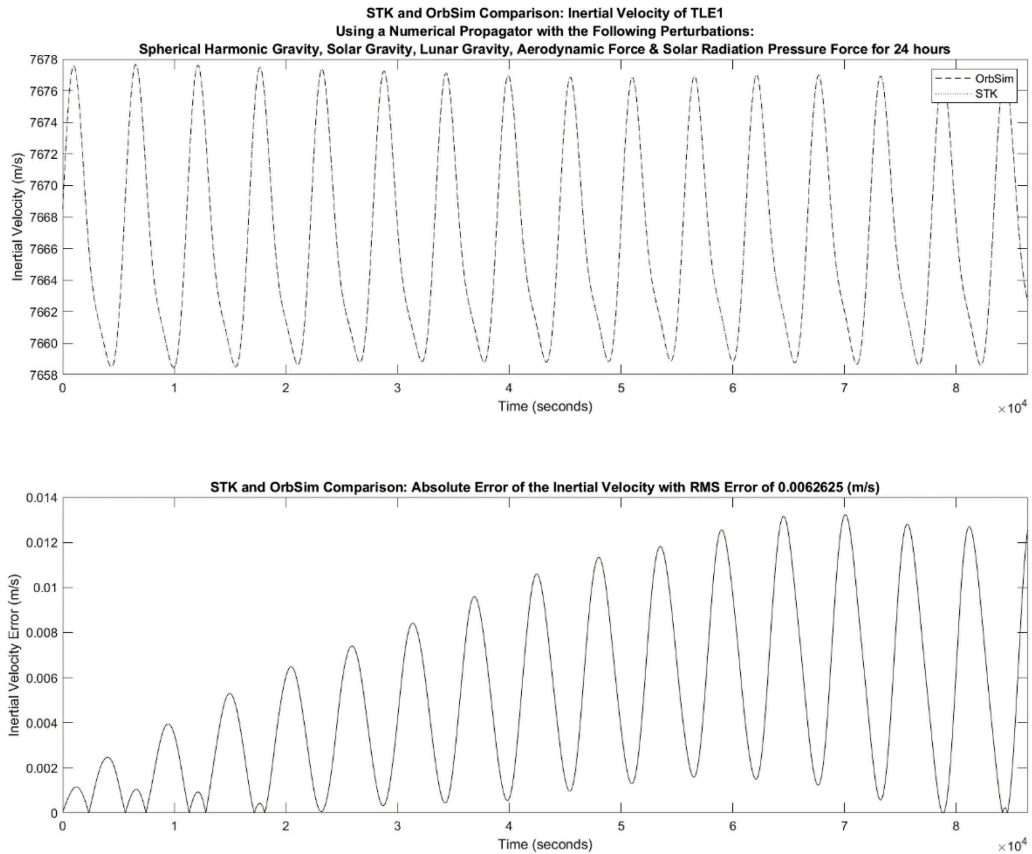


Figure 59: Inertial Velocity Comparison of the Satellite from TLE#1 with Spherical Harmonic Gravity, Solar Gravity, Lunar Gravity, Aerodynamic Force and Solar Radiation Pressure

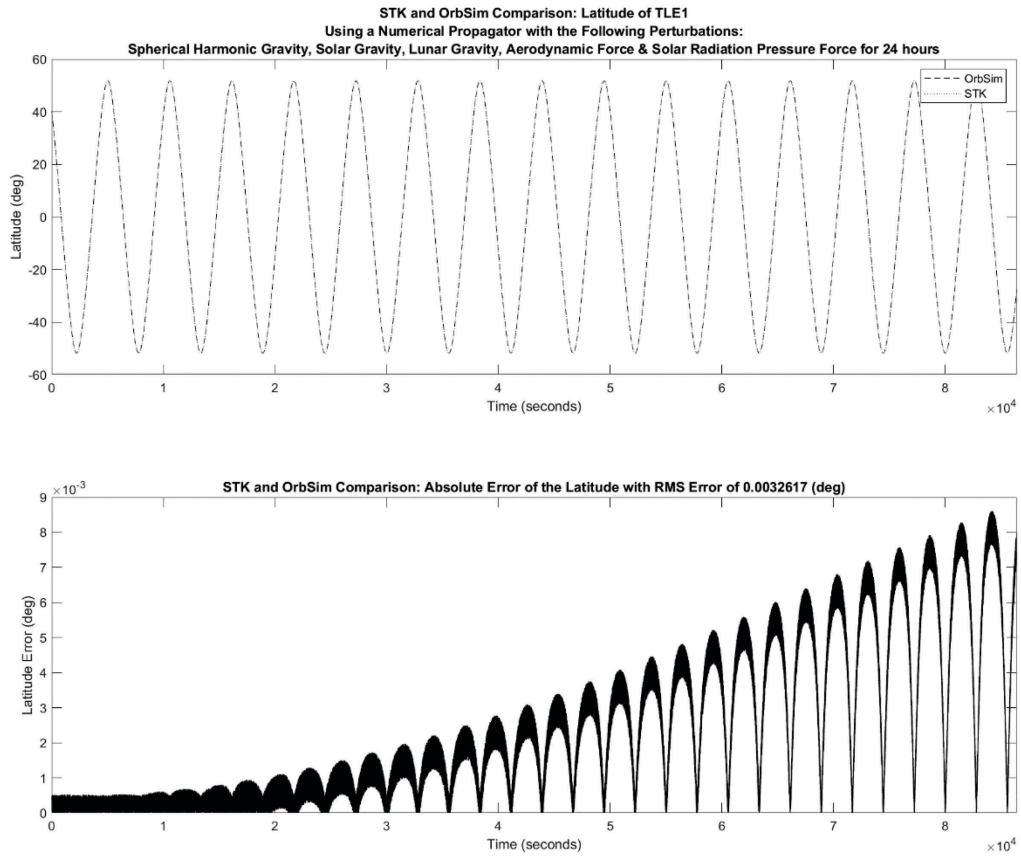


Figure 60: Latitude Comparison of the Satellite from TLE#1 with Spherical Harmonic Gravity, Solar Gravity, Lunar Gravity, Aerodynamic Force and Solar Radiation Pressure

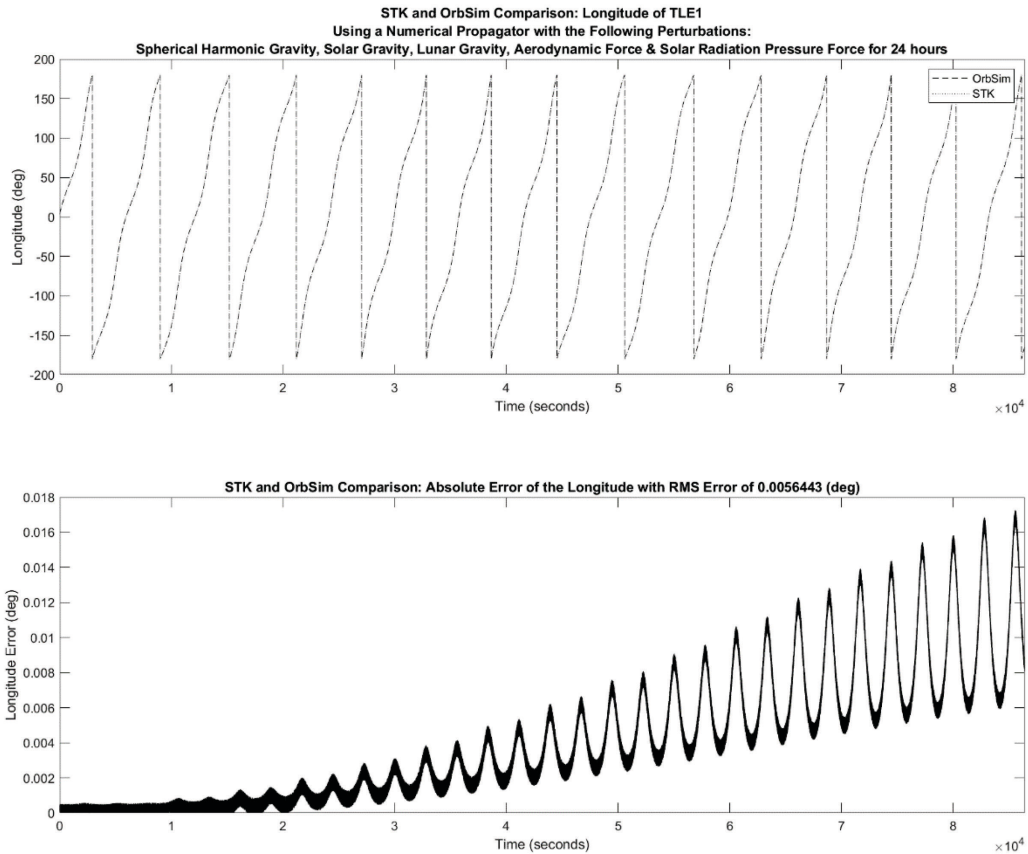


Figure 61: Longitude Comparison of the Satellite from TLE#1 with Spherical Harmonic Gravity, Solar Gravity, Lunar Gravity, Aerodynamic Force and Solar Radiation Pressure

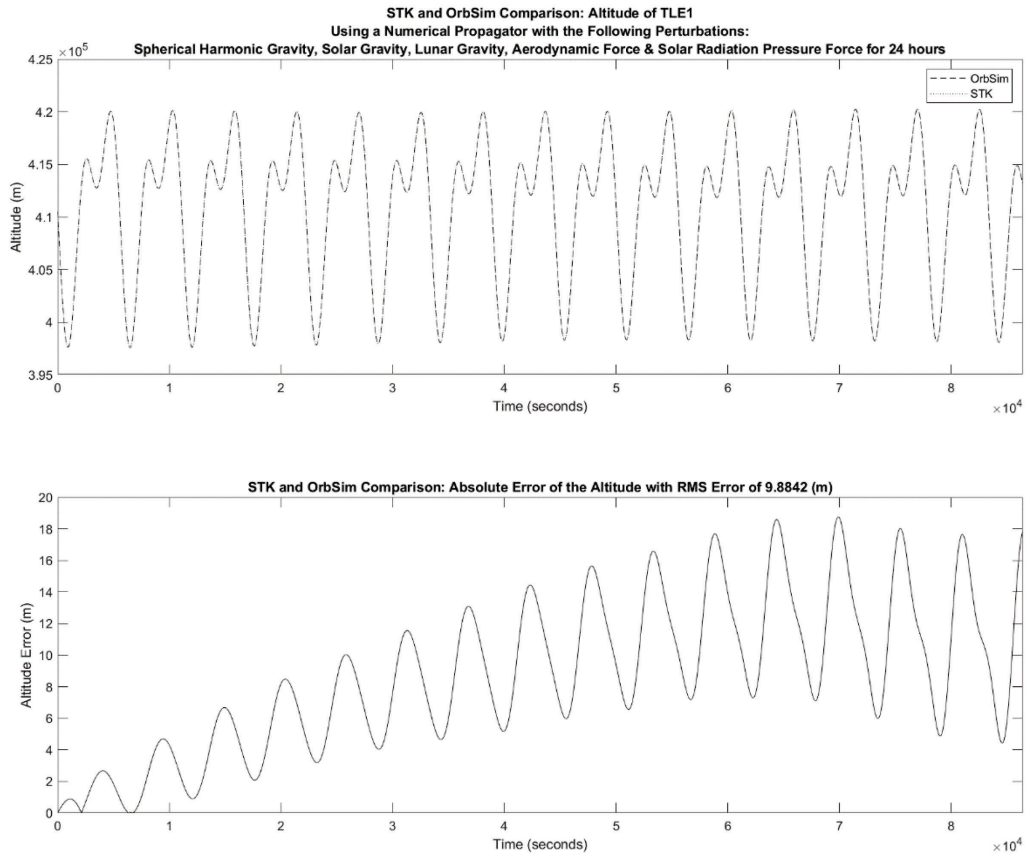


Figure 62: Altitude Comparison of the Satellite from TLE#2 with Spherical Harmonic Gravity, Solar Gravity, Lunar Gravity, Aerodynamic Force and Solar Radiation Pressure

B.2: TLE #2

B.2.1: Two Body Gravity

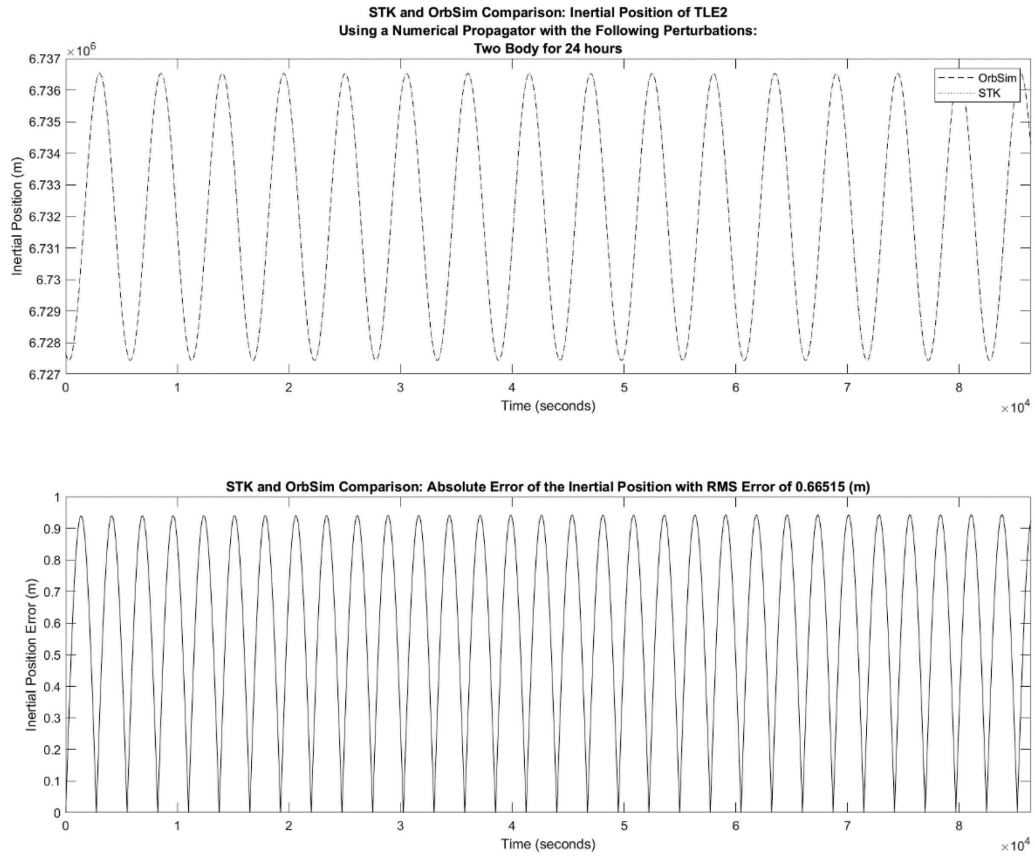


Figure 63: Inertial Position Comparison of the Satellite from TLE#2 with Two Body Gravity

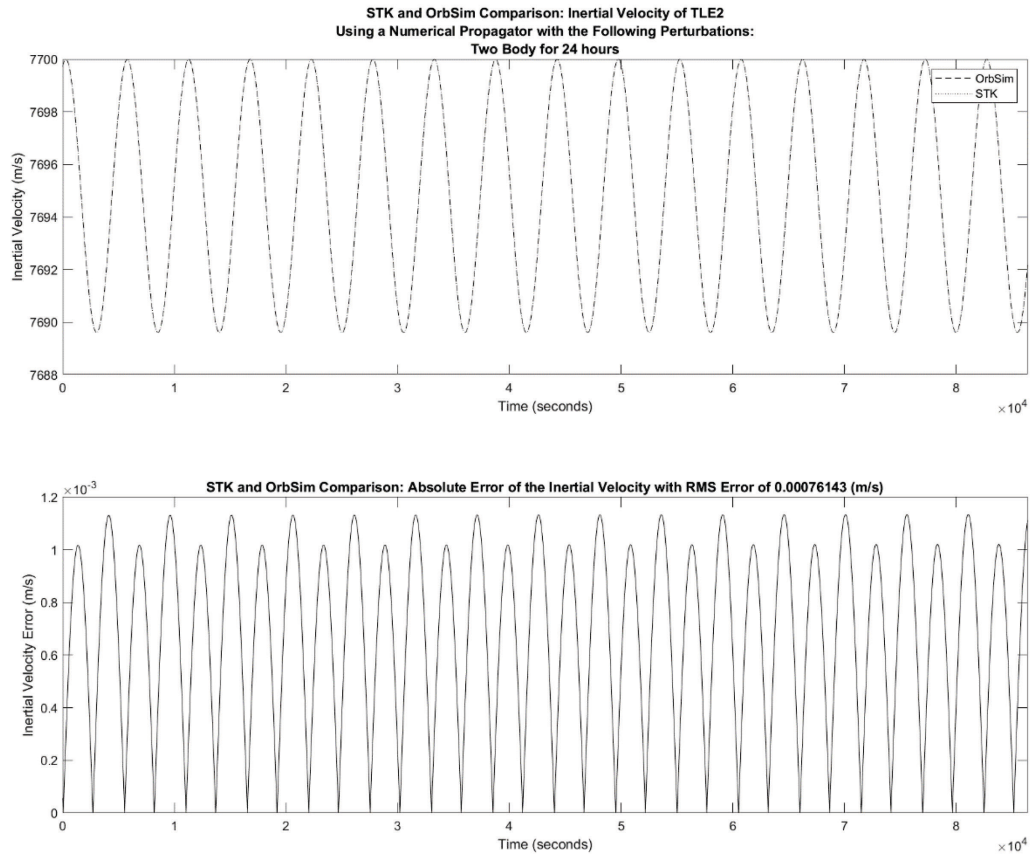


Figure 64: Inertial Velocity Comparison of the Satellite from TLE#2 with Two Body Gravity

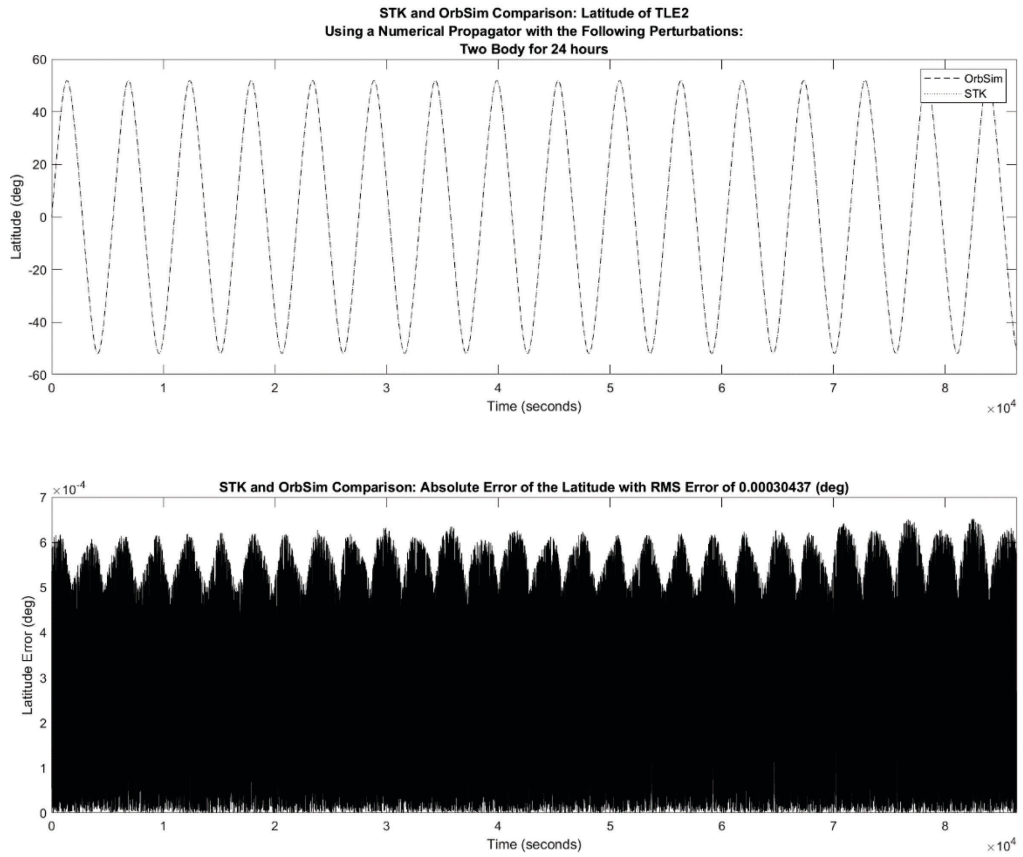


Figure 65: Latitude Comparison of the Satellite from TLE#2 with Two Body Gravity

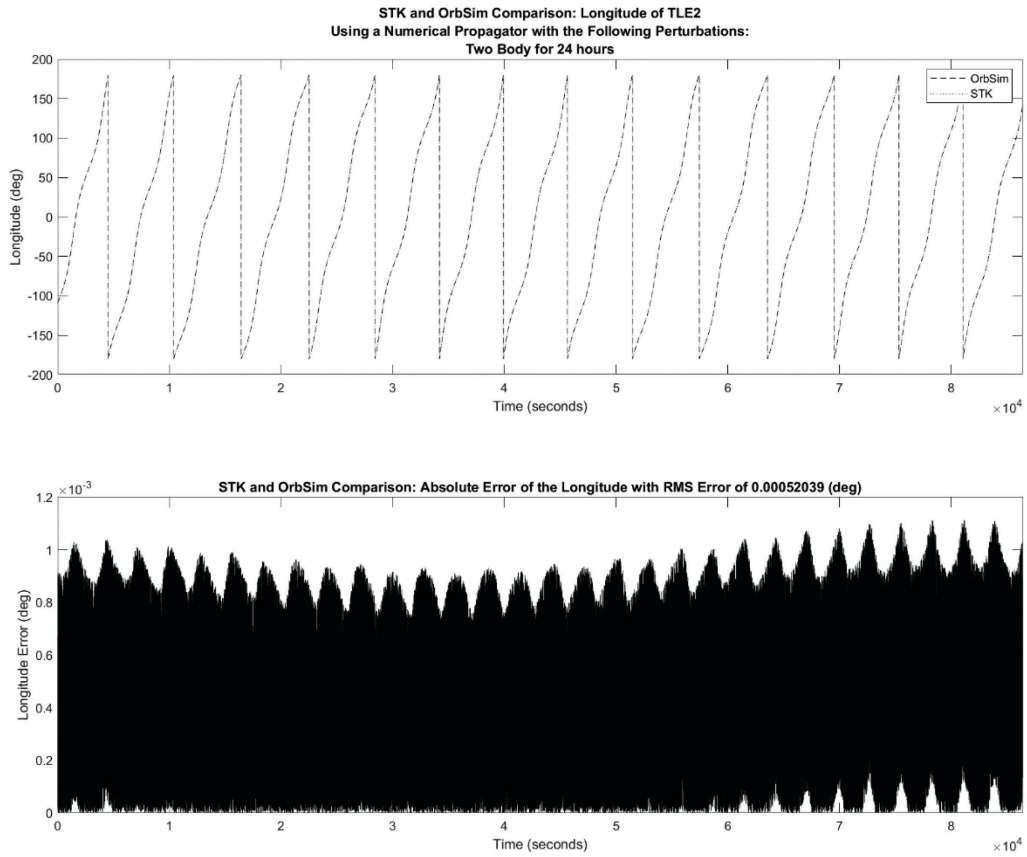


Figure 66: Longitude Comparison of the Satellite from TLE#2 with Two Body Gravity

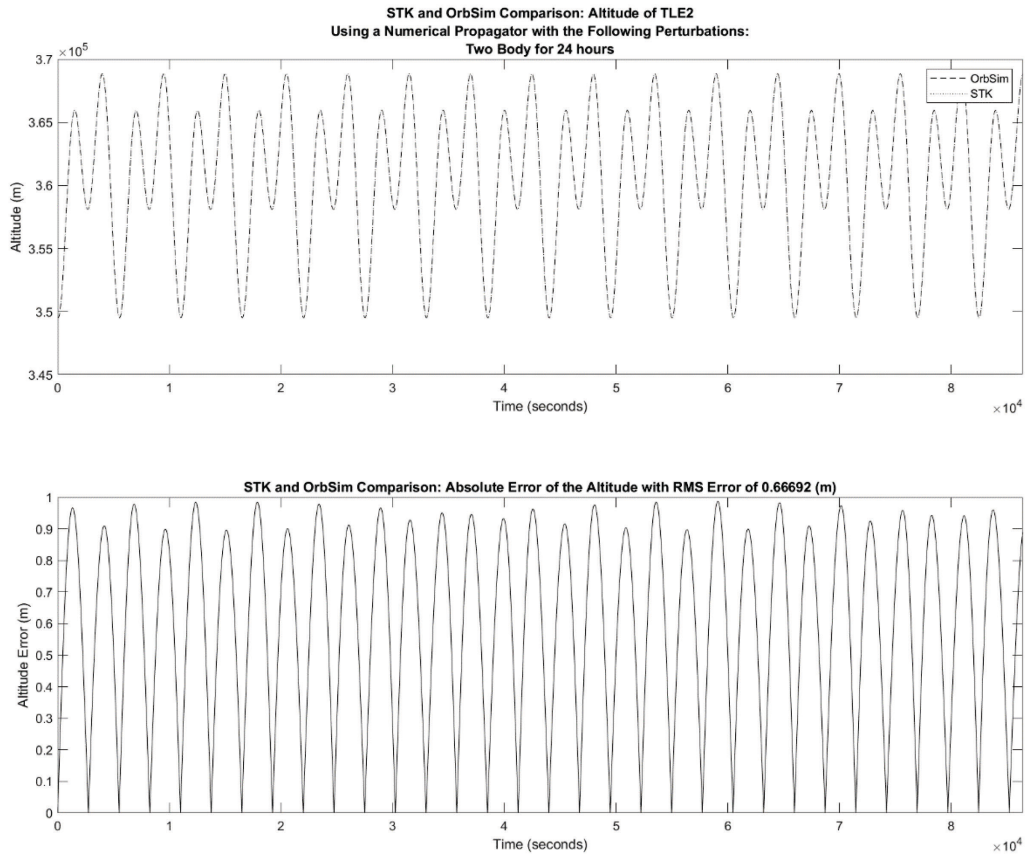


Figure 67: Altitude Comparison of the Satellite from TLE#2 with Two Body Gravity

B.2.2: Spherical Harmonic Gravity

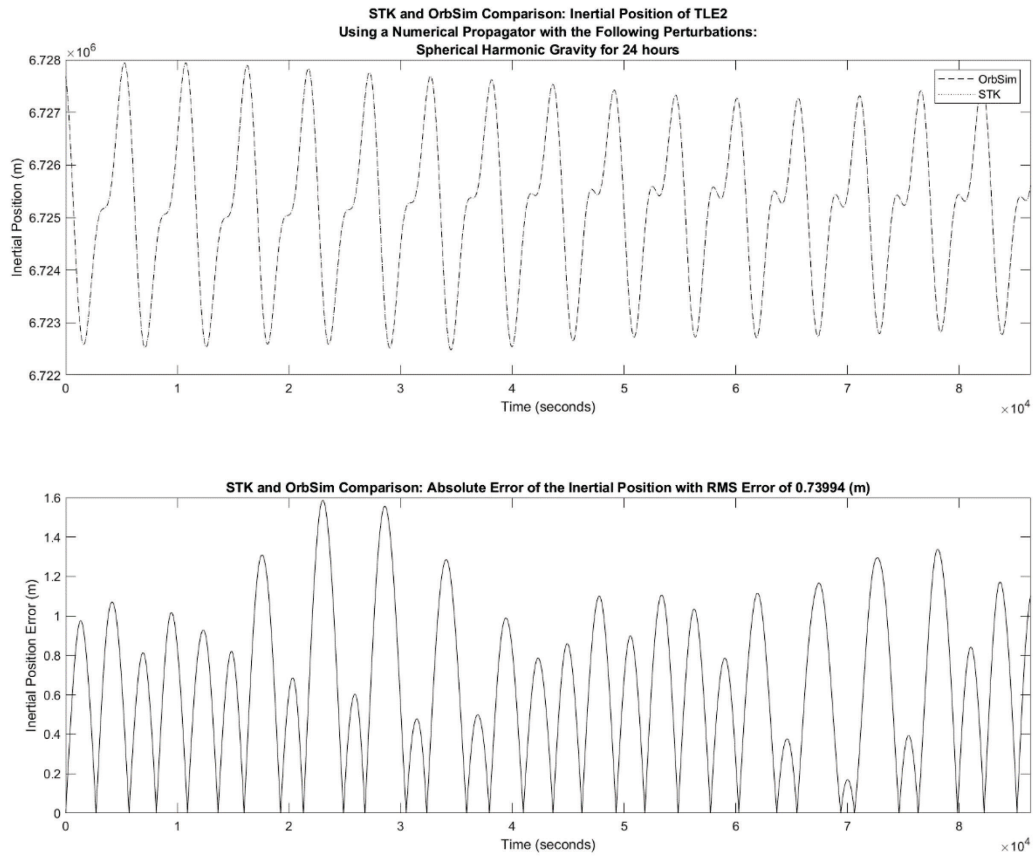


Figure 68: Inertial Position Comparison of the Satellite from TLE#2 with Spherical Harmonic Gravity

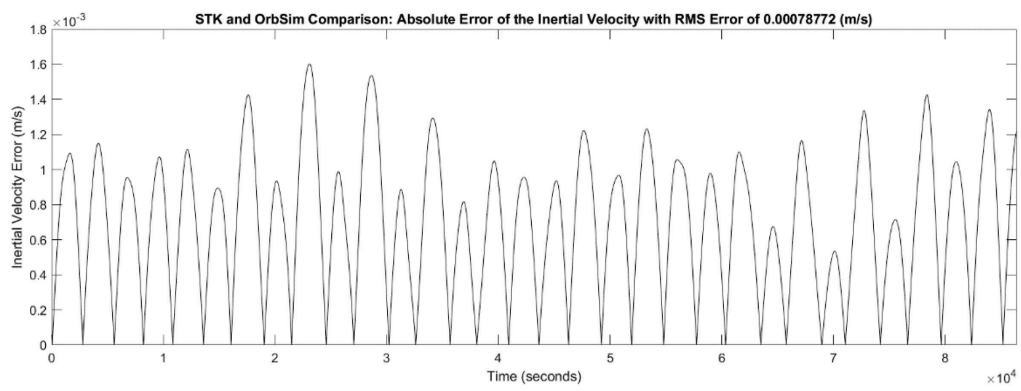
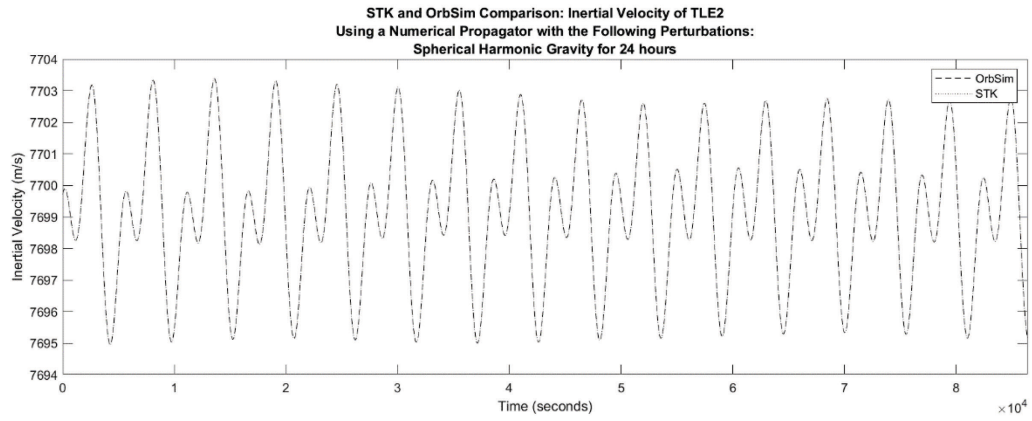


Figure 69: Inertial Velocity Comparison of the Satellite from TLE#2 with Spherical Harmonic Gravity

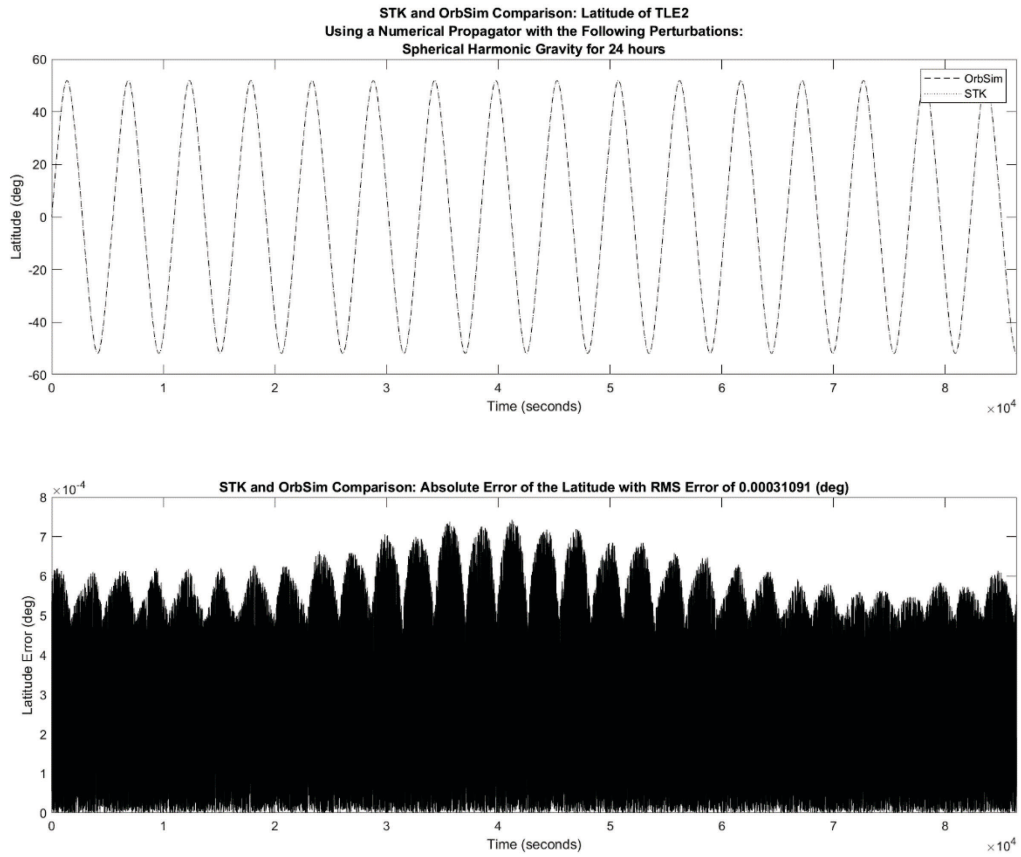


Figure 70: Latitude Comparison of the Satellite from TLE#2 with Spherical Harmonic Gravity

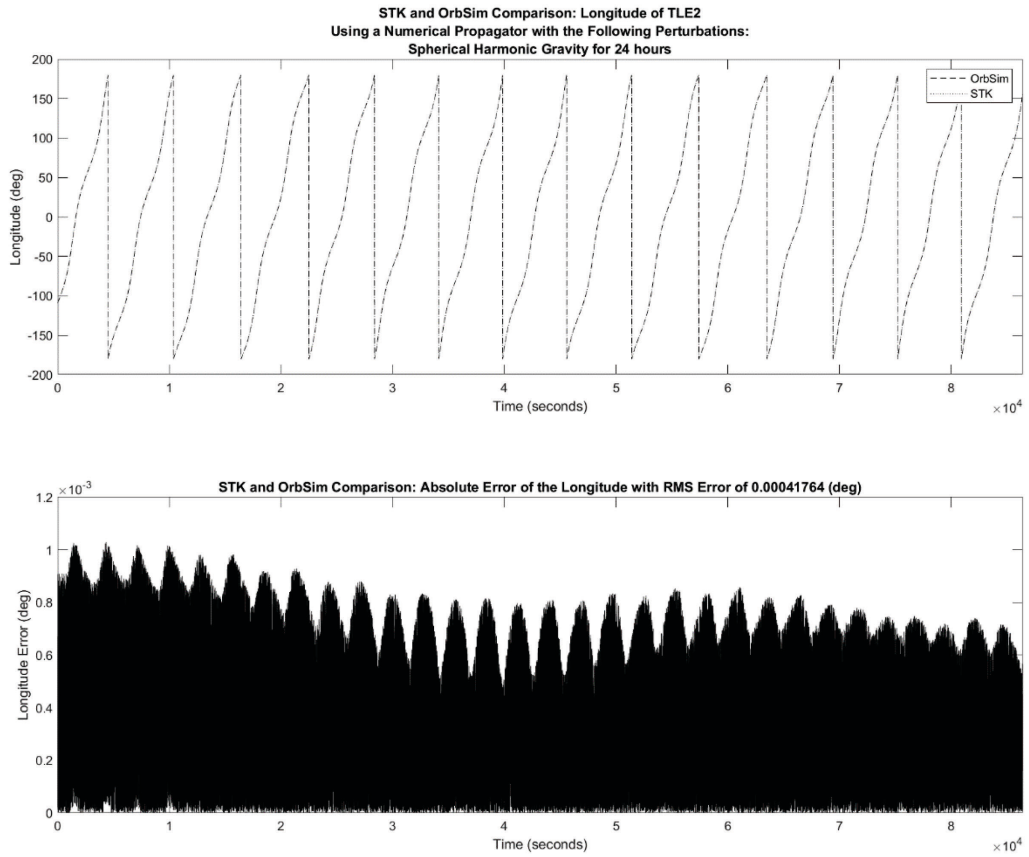


Figure 71: Longitude Comparison of the Satellite from TLE#2 with Spherical Harmonic Gravity

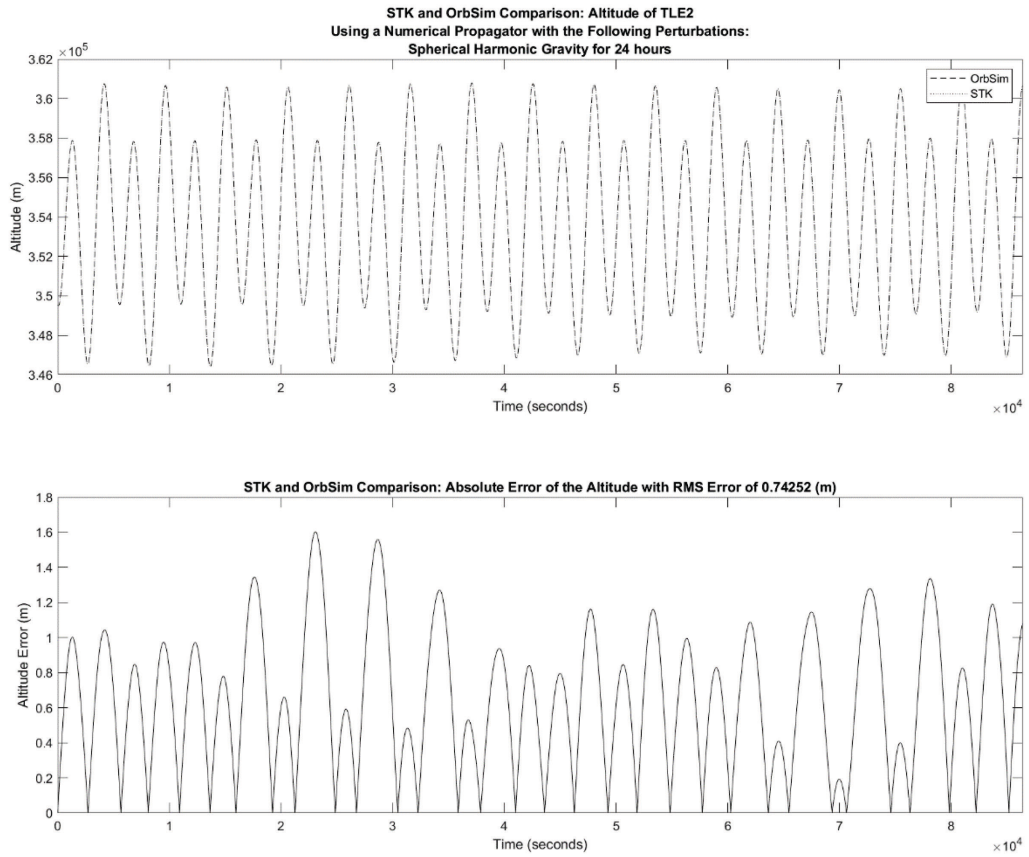


Figure 72: Altitude Comparison of the Satellite from TLE#2 with Spherical Harmonic Gravity

B.2.3: Spherical Harmonic Gravity & Solar gravity

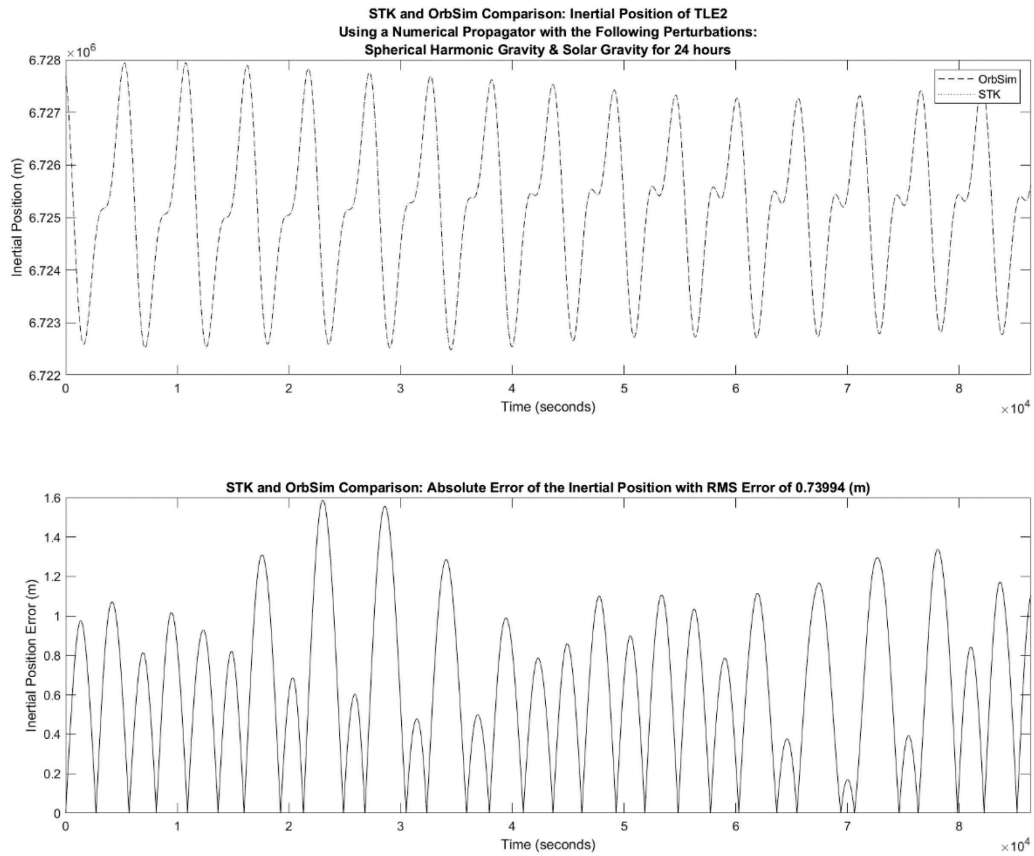


Figure 73: Inertial Position Comparison of the Satellite from TLE#2 with Spherical Harmonic Gravity and Solar Gravity

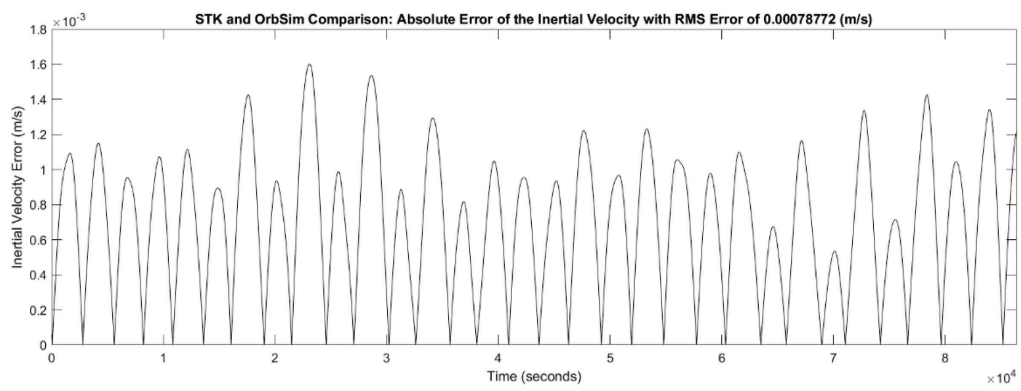
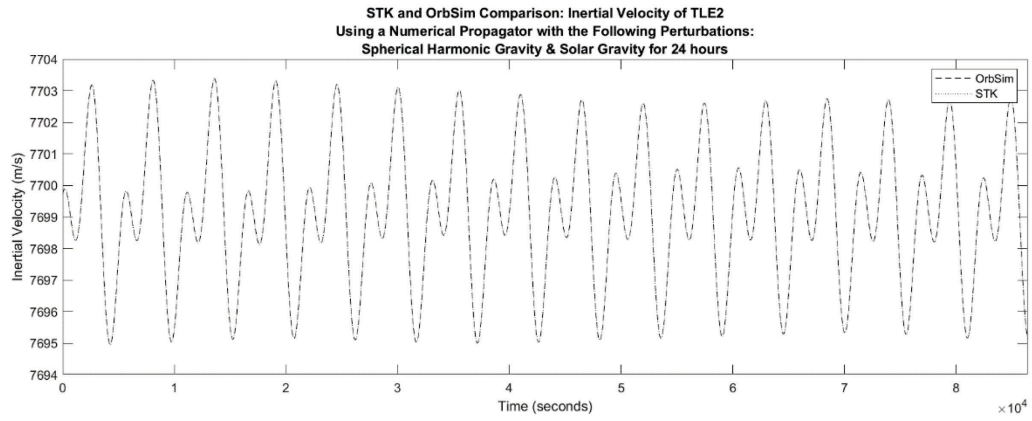


Figure 74: Inertial Velocity Comparison of the Satellite from TLE#2 with Spherical Harmonic Gravity and Solar Gravity

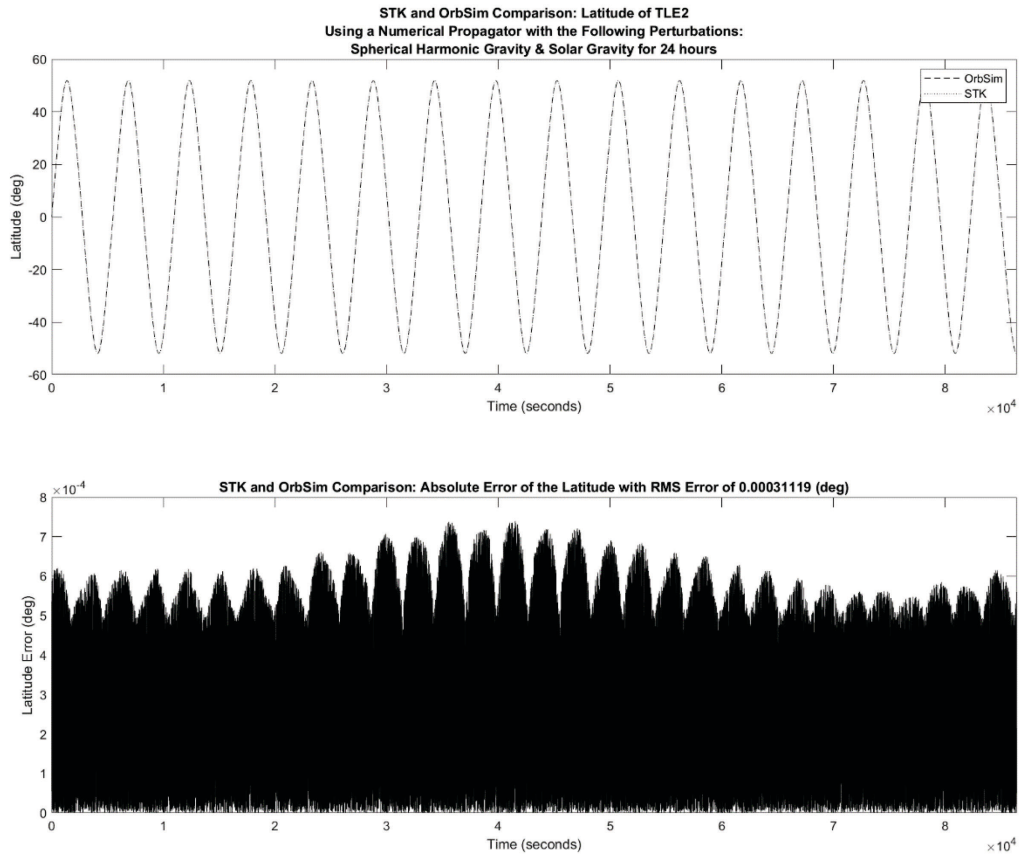


Figure 75: Latitude Comparison of the Satellite from TLE#2 with Spherical Harmonic Gravity and Solar Gravity

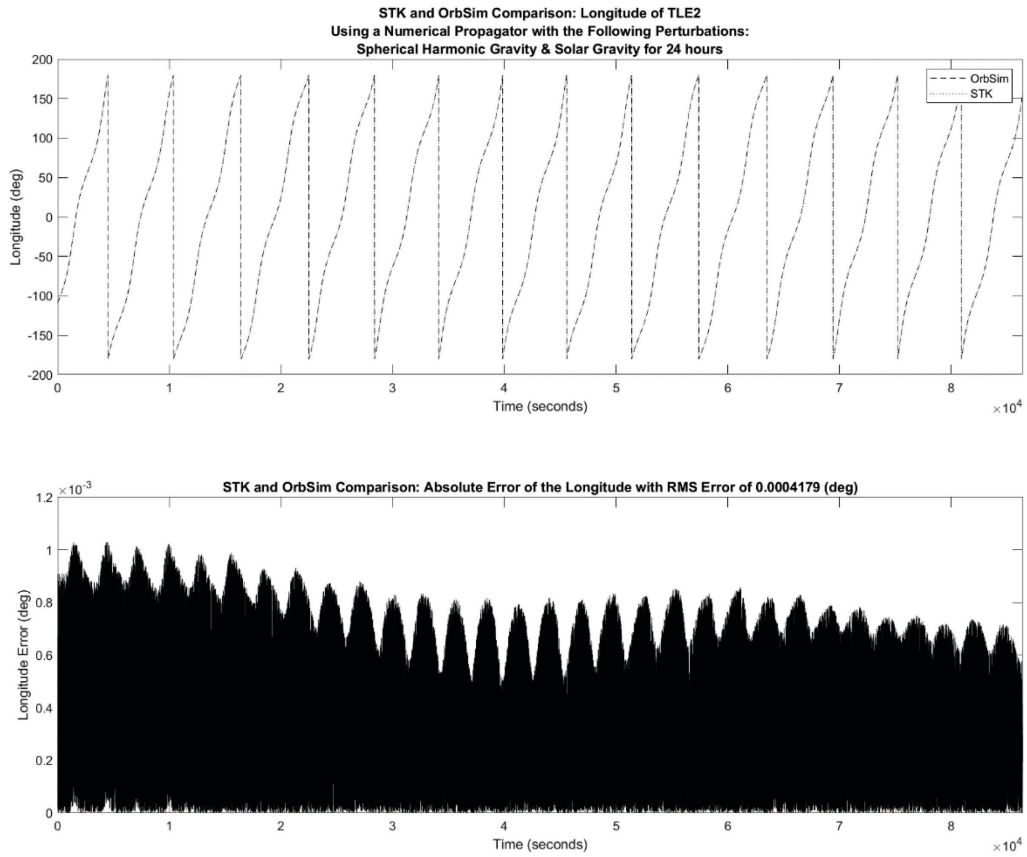


Figure 76: Longitude Comparison of the Satellite from TLE#2 with Spherical Harmonic Gravity and Solar Gravity

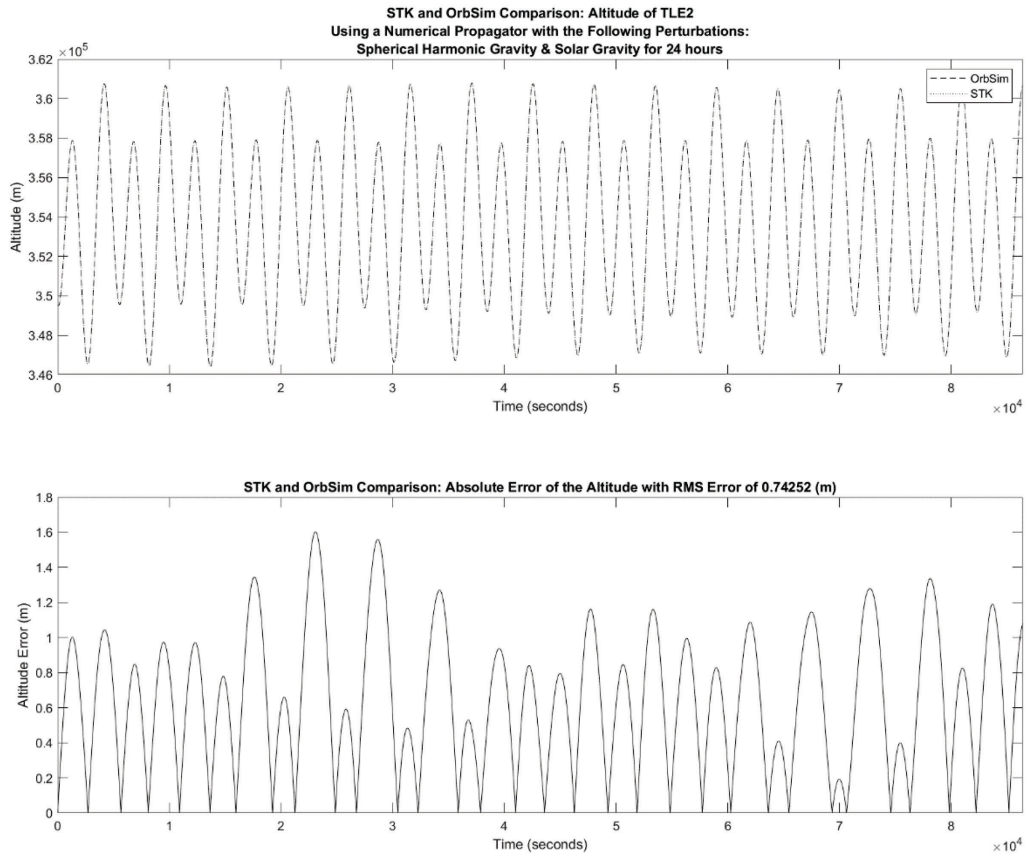


Figure 77: Altitude Comparison of the Satellite from TLE#2 with Spherical Harmonic Gravity and Solar Gravity

B.2.4: Spherical Harmonic Gravity & Lunar Gravity

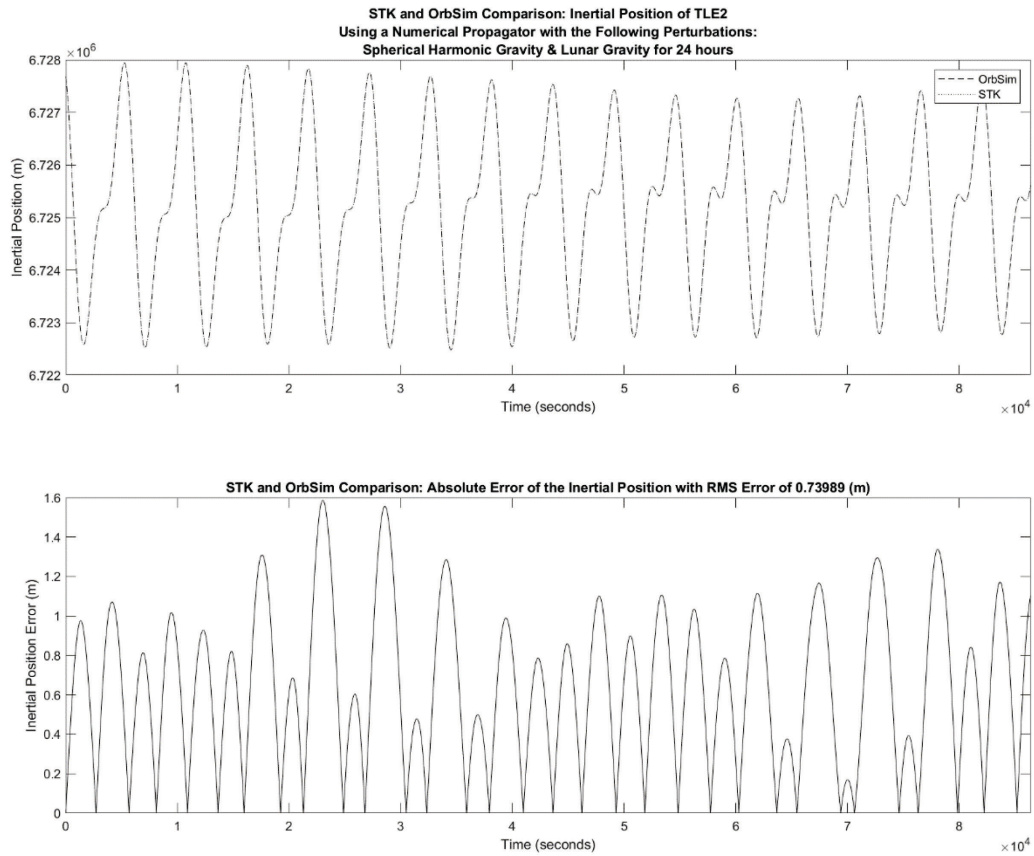


Figure 78: Inertial Position Comparison of the Satellite from TLE#2 with Spherical Harmonic Gravity and Lunar Gravity

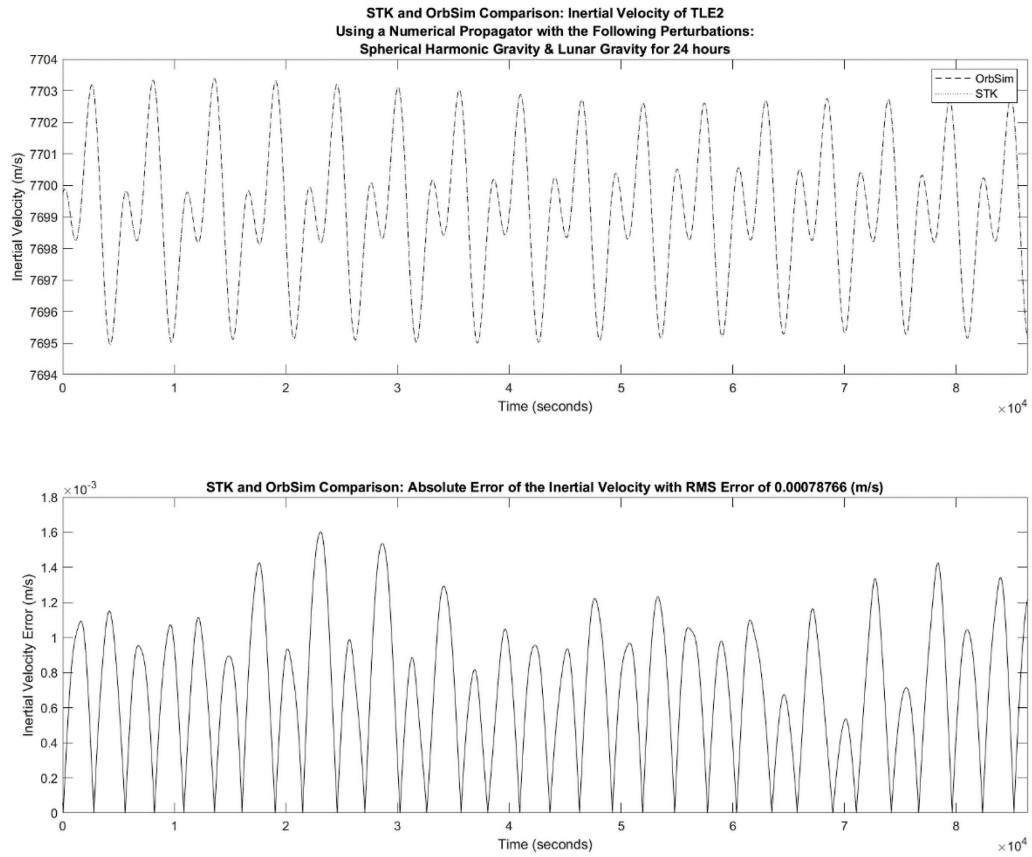


Figure 79: Inertial Velocity Comparison of the Satellite from TLE#2 with Spherical Harmonic Gravity and Lunar Gravity

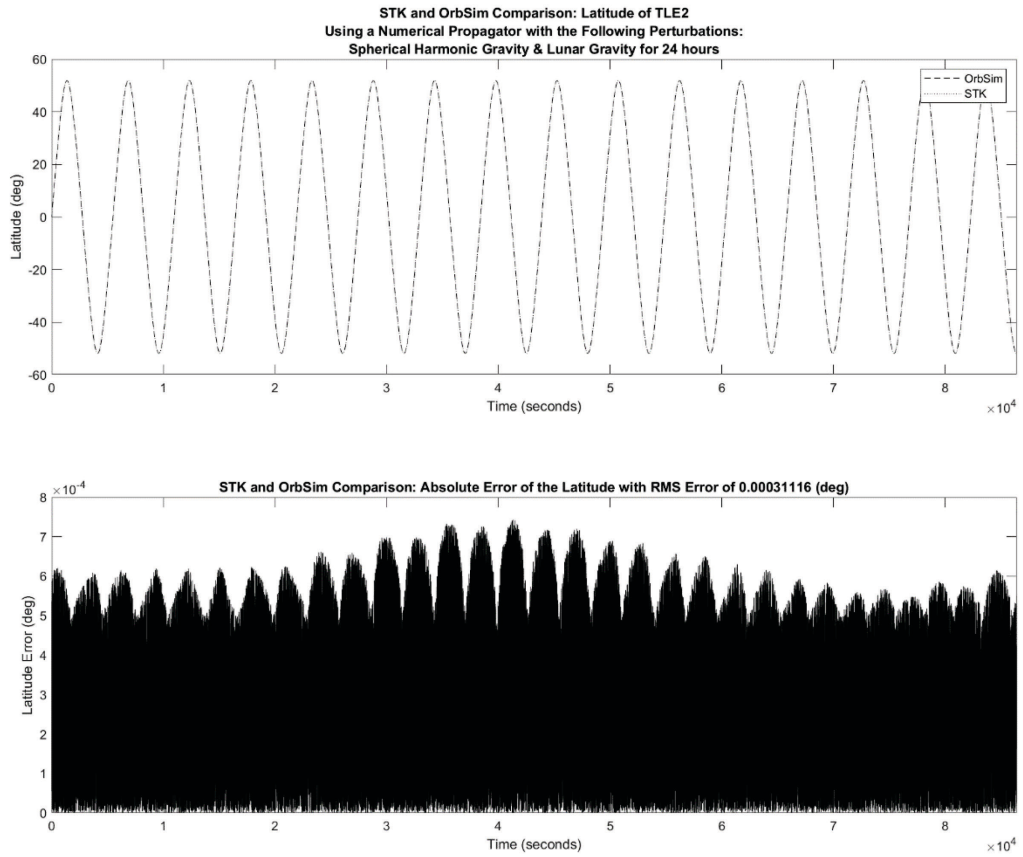


Figure 80: Latitude Comparison of the Satellite from TLE#2 with Spherical Harmonic Gravity and Lunar Gravity

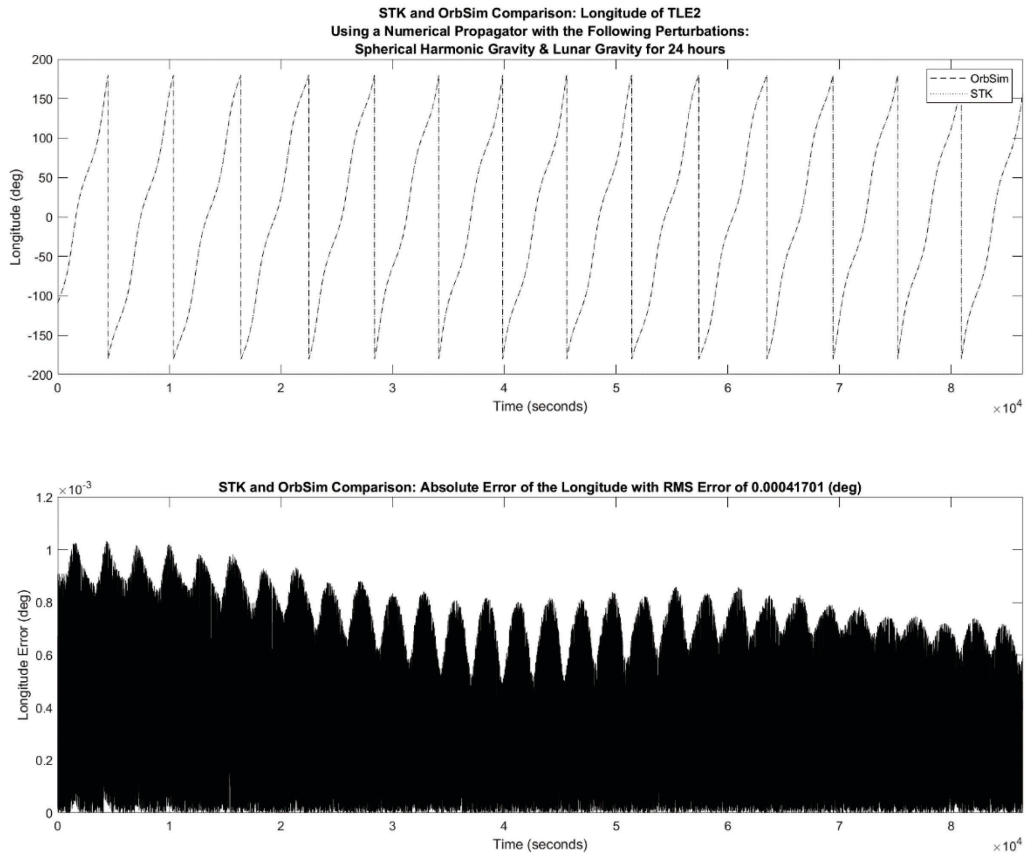


Figure 81: Longitude Comparison of the Satellite from TLE#2 with Spherical Harmonic Gravity and Lunar Gravity

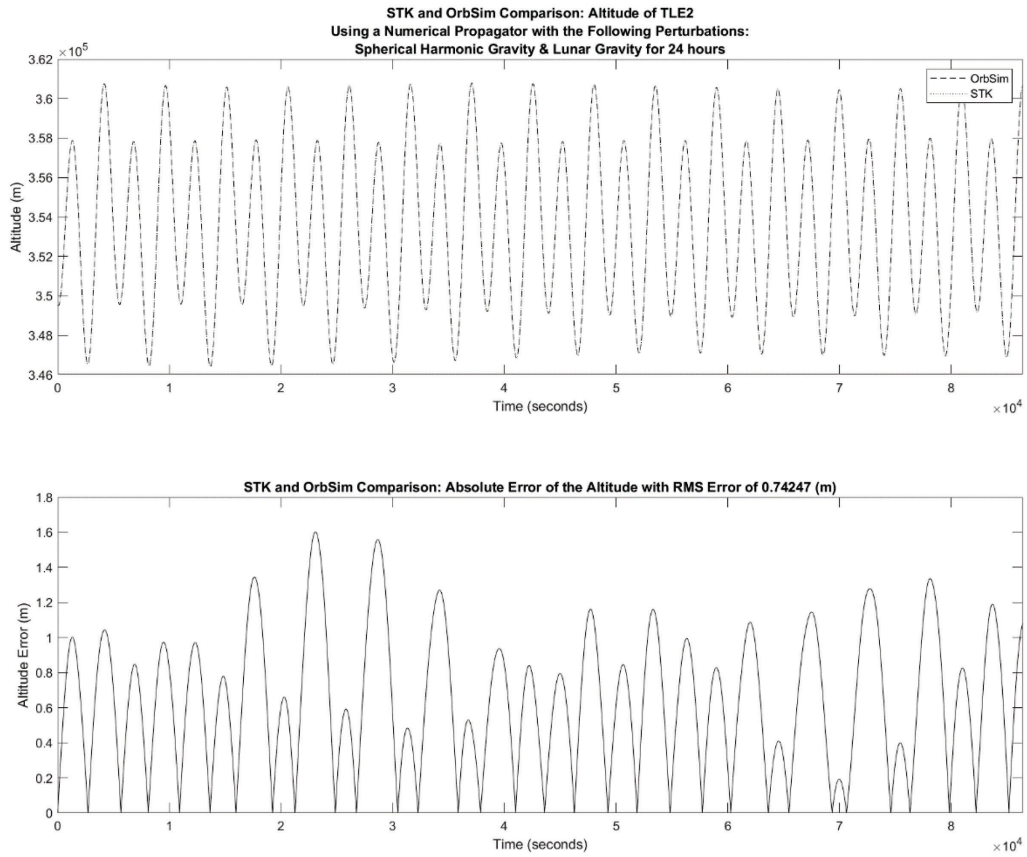


Figure 82: Altitude Comparison of the Satellite from TLE#2 with Spherical Harmonic Gravity and Lunar Gravity

B.2.5: Spherical Harmonic Gravity & Aerodynamic Drag

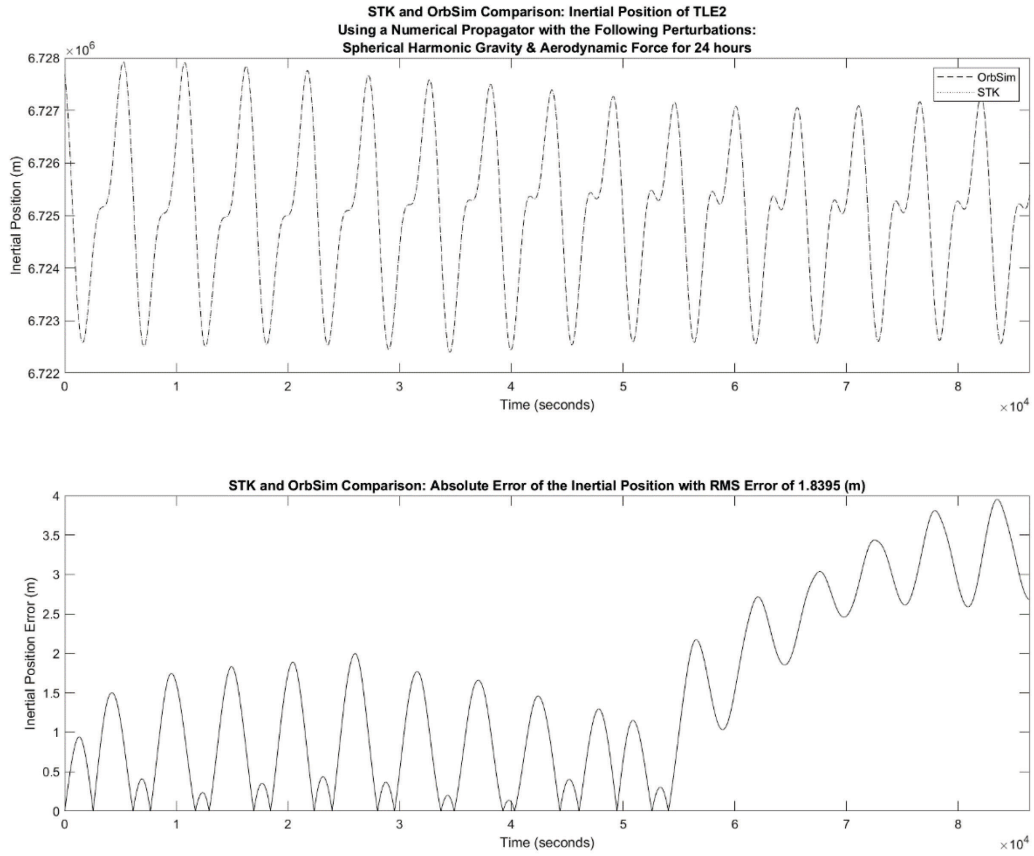


Figure 83: Inertial Position Comparison of the Satellite from TLE#2 with Spherical Harmonic Gravity and Aerodynamic Drag

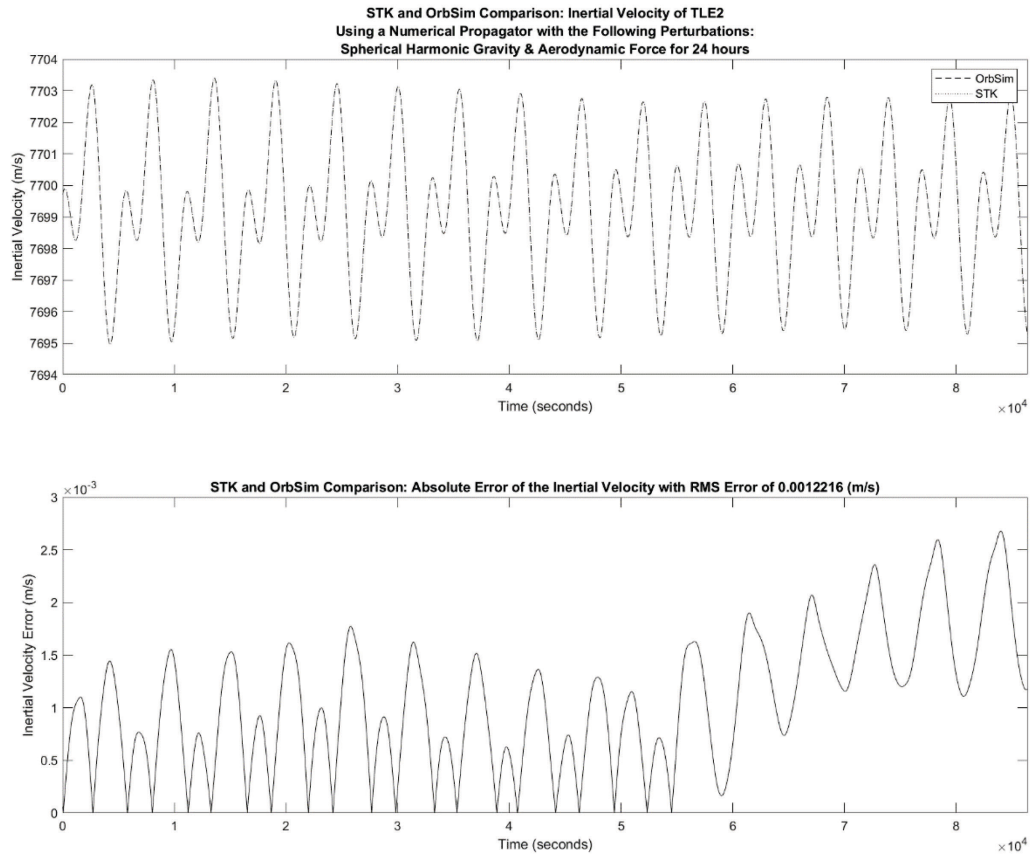


Figure 84: Inertial Velocity Comparison of the Satellite from TLE#2 with Spherical Harmonic Gravity and Aerodynamic Drag

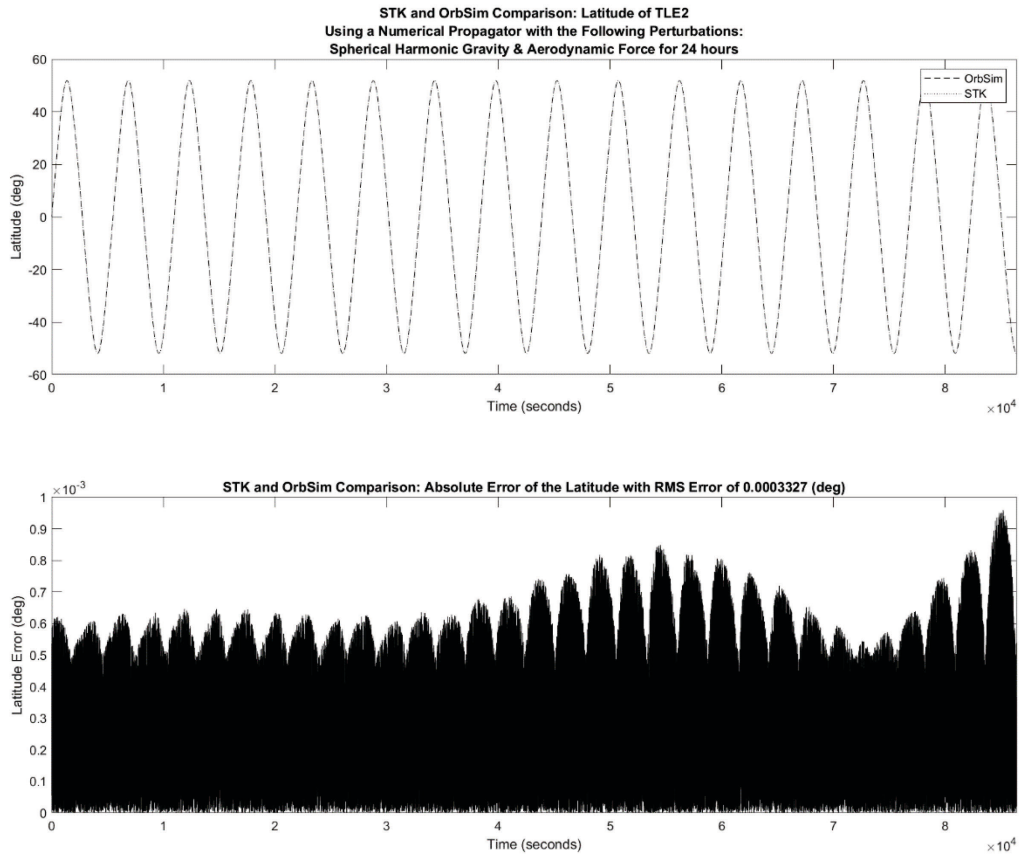


Figure 85: Latitude Comparison of the Satellite from TLE#2 with Spherical Harmonic Gravity and Aerodynamic Drag

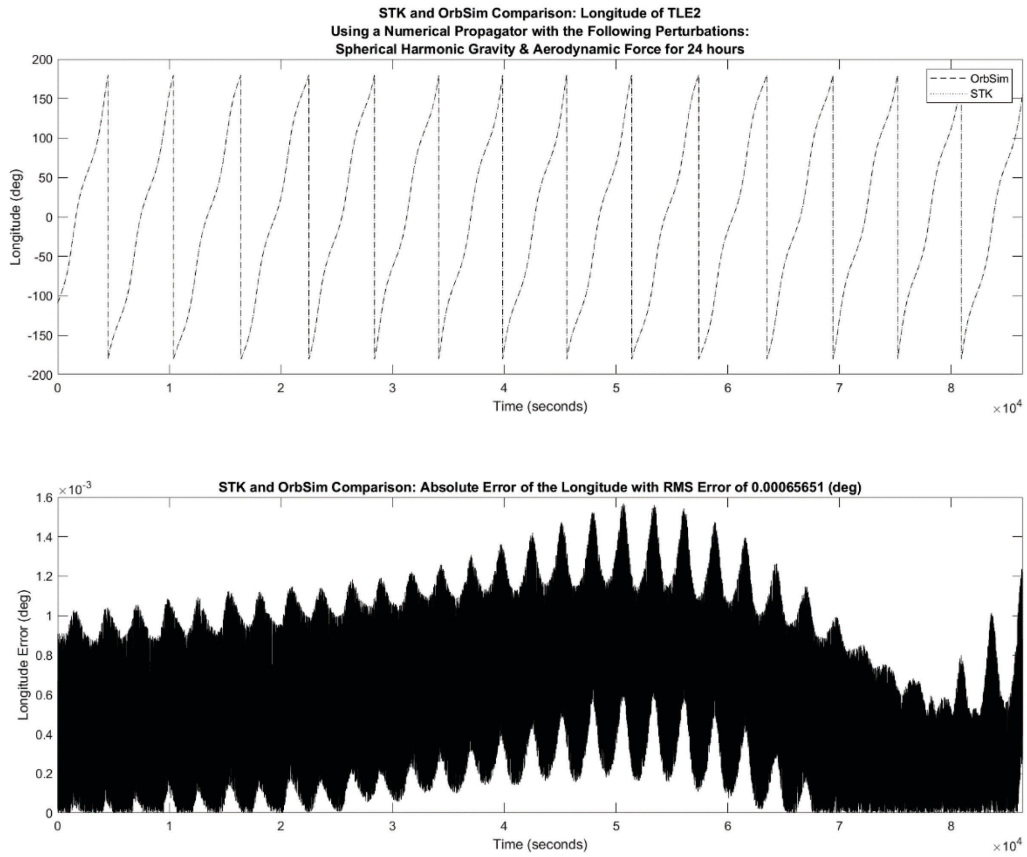


Figure 86: Longitude Comparison of the Satellite from TLE#2 with Spherical Harmonic Gravity and Aerodynamic Drag

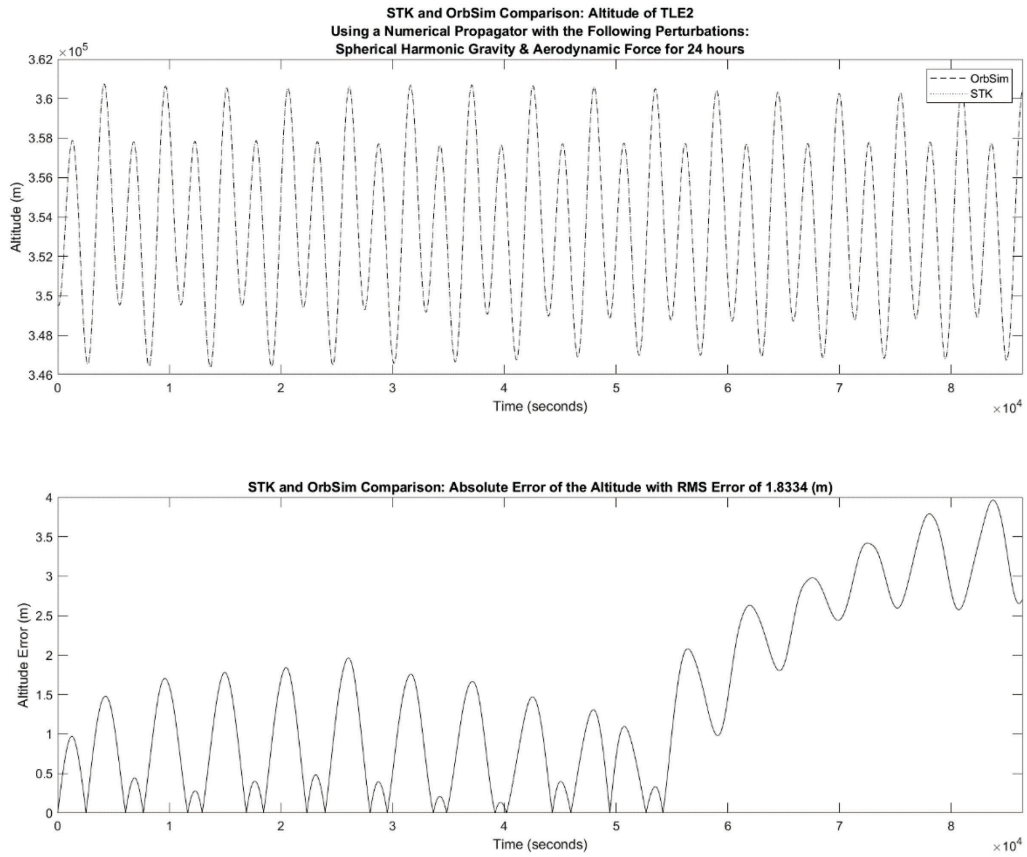


Figure 87: Altitude Comparison of the Satellite from TLE#2 with Spherical Harmonic Gravity and Aerodynamic Drag

B.2.6: Spherical Harmonic Gravity & Solar Pressure

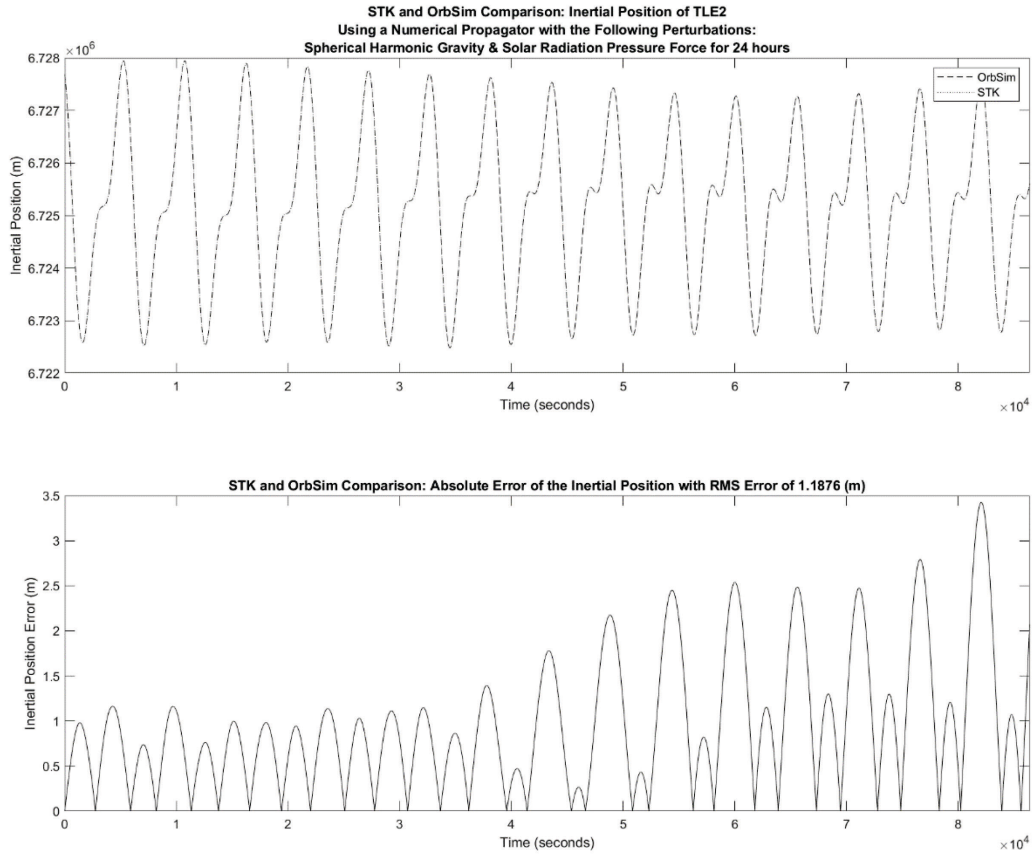


Figure 88: Inertial Position Comparison of the Satellite from TLE#2 with Spherical Harmonic Gravity and Solar Radiation Pressure

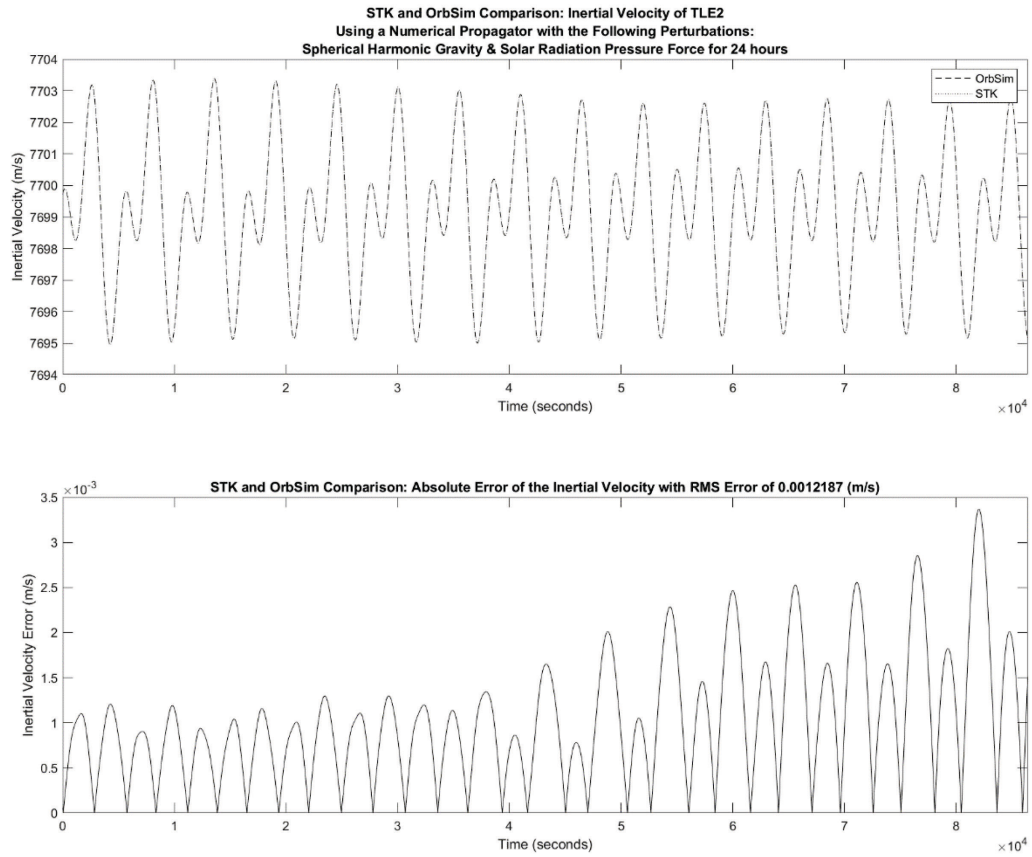


Figure 89: Inertial Velocity Comparison of the Satellite from TLE#2 with Spherical Harmonic Gravity and Solar Radiation Pressure

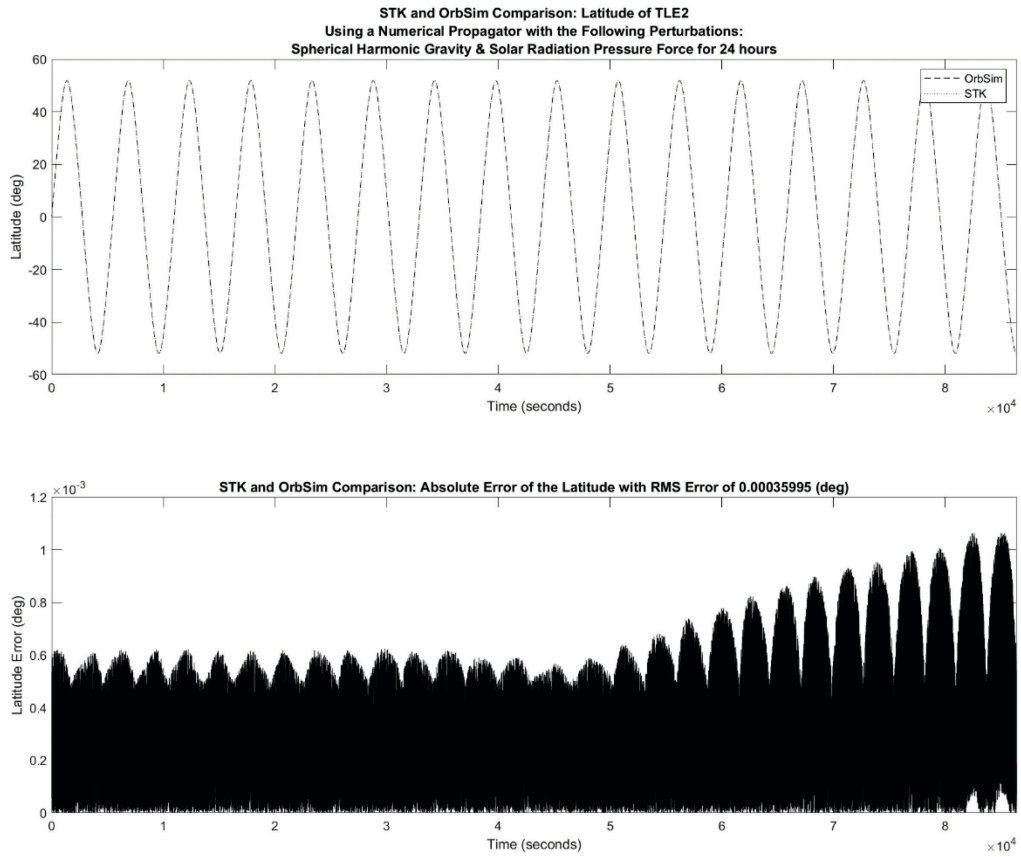


Figure 90: Latitude Comparison of the Satellite from TLE#2 with Spherical Harmonic Gravity and Solar Radiation Pressure

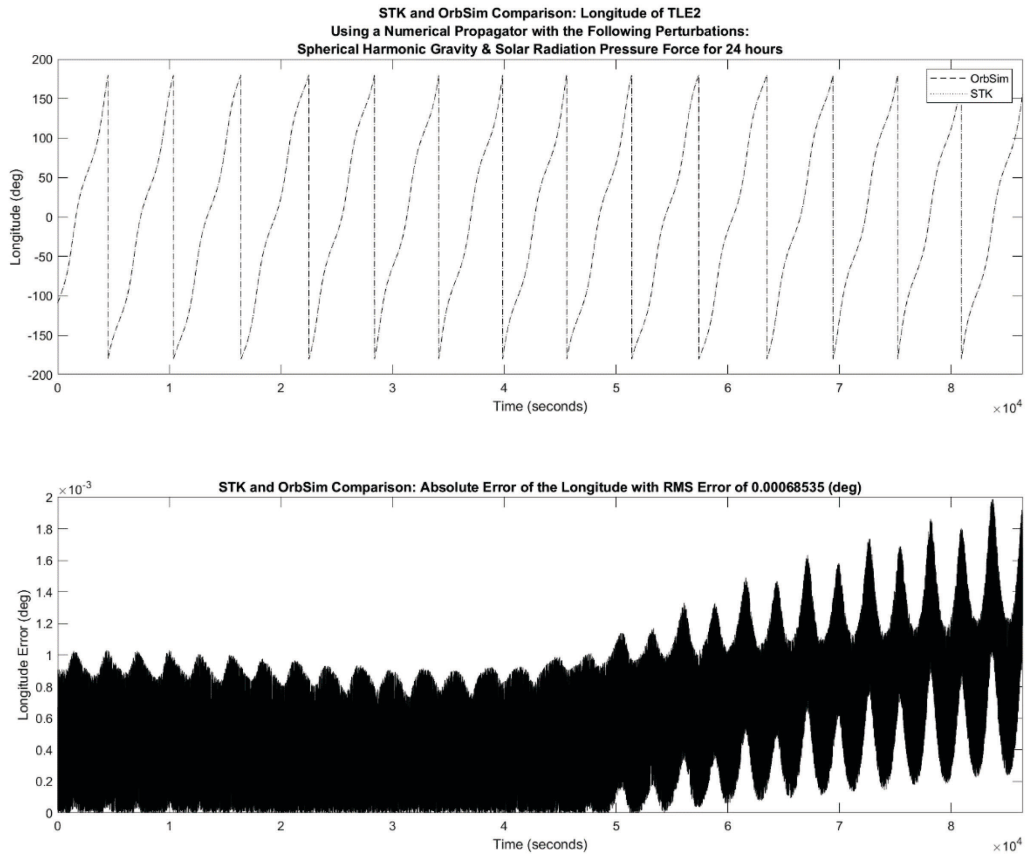


Figure 91: Longitude Comparison of the Satellite from TLE#2 with Spherical Harmonic Gravity and Solar Radiation Pressure

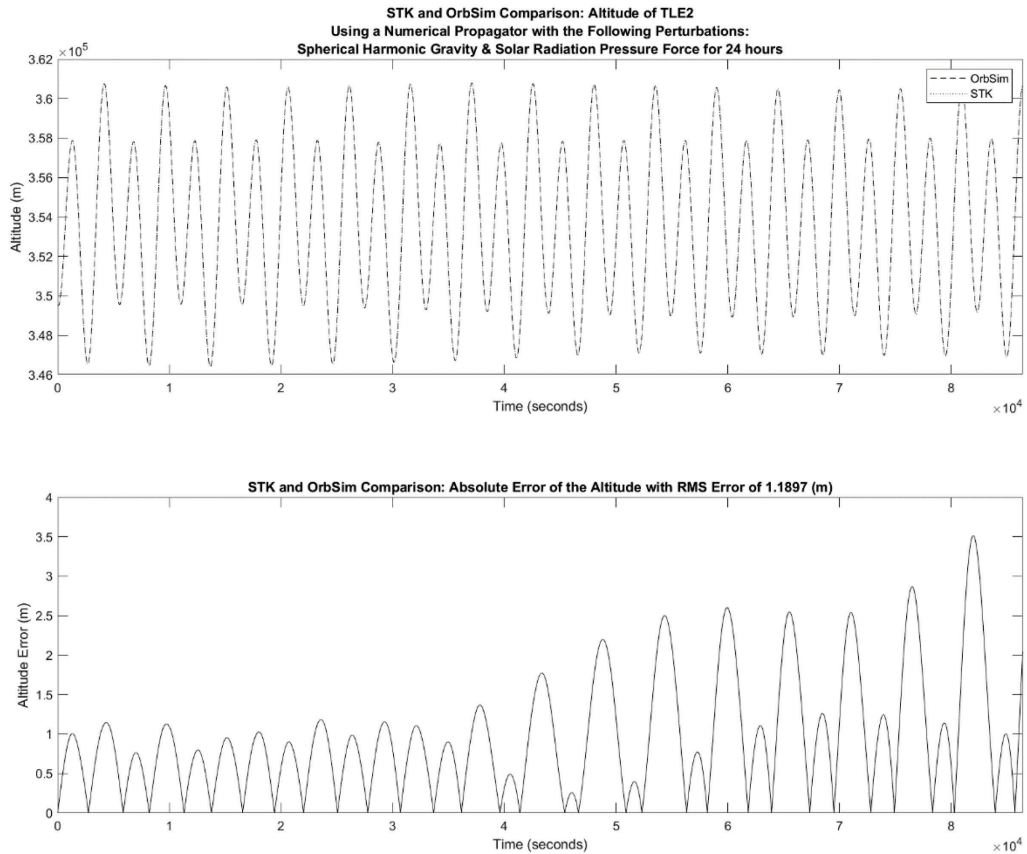


Figure 92: Altitude Comparison of the Satellite from TLE#2 with Spherical Harmonic Gravity and Solar Radiation Pressure

B.2.7: Spherical Harmonic Gravity, Solar Gravity, Lunar Gravity, Aerodynamic Drag and Solar Pressure

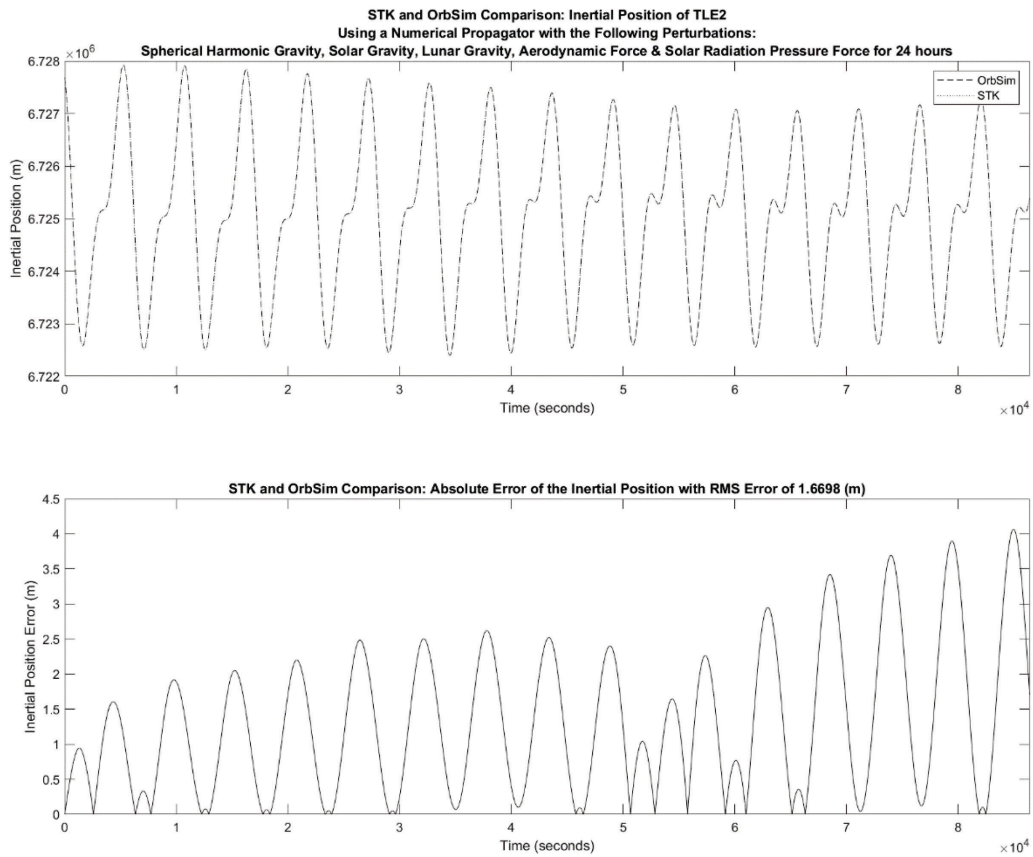


Figure 93: Inertial Position Comparison of the Satellite from TLE#2 with Spherical Harmonic Gravity, Solar Gravity, Lunar Gravity, Aerodynamic Force and Solar Radiation Pressure

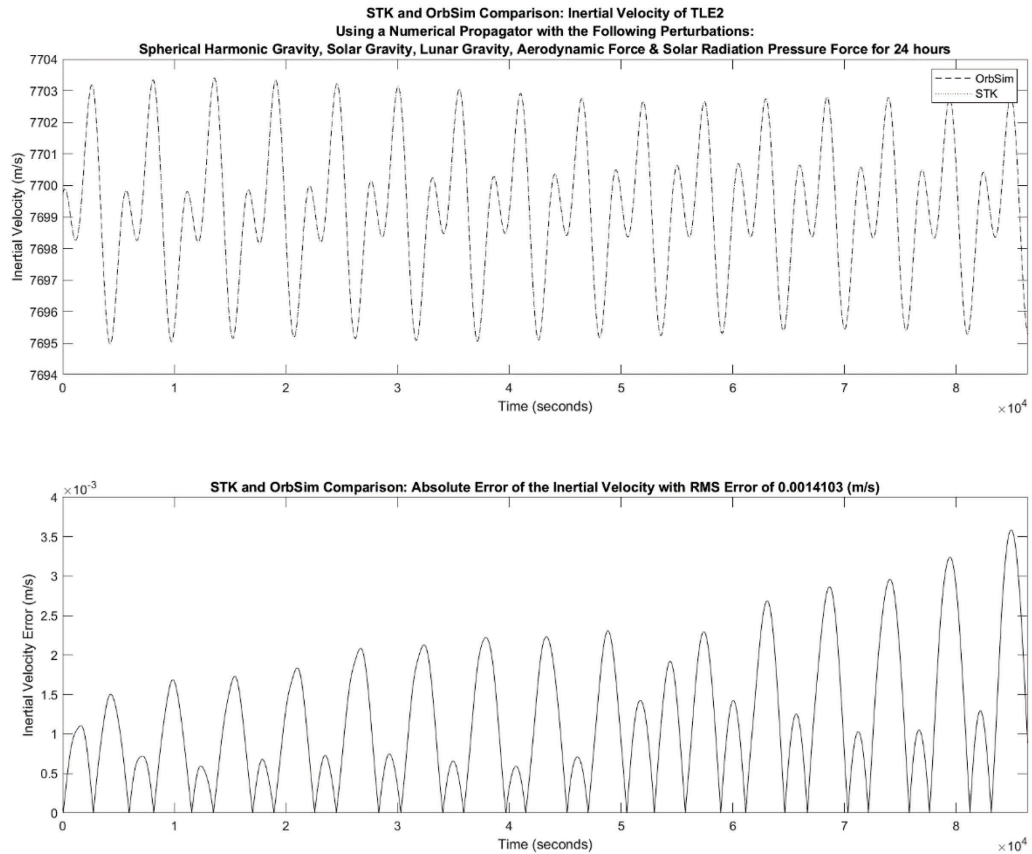


Figure 94: Inertial Velocity Comparison of the Satellite from TLE#2 with Spherical Harmonic Gravity, Solar Gravity, Lunar Gravity, Aerodynamic Force and Solar Radiation Pressure

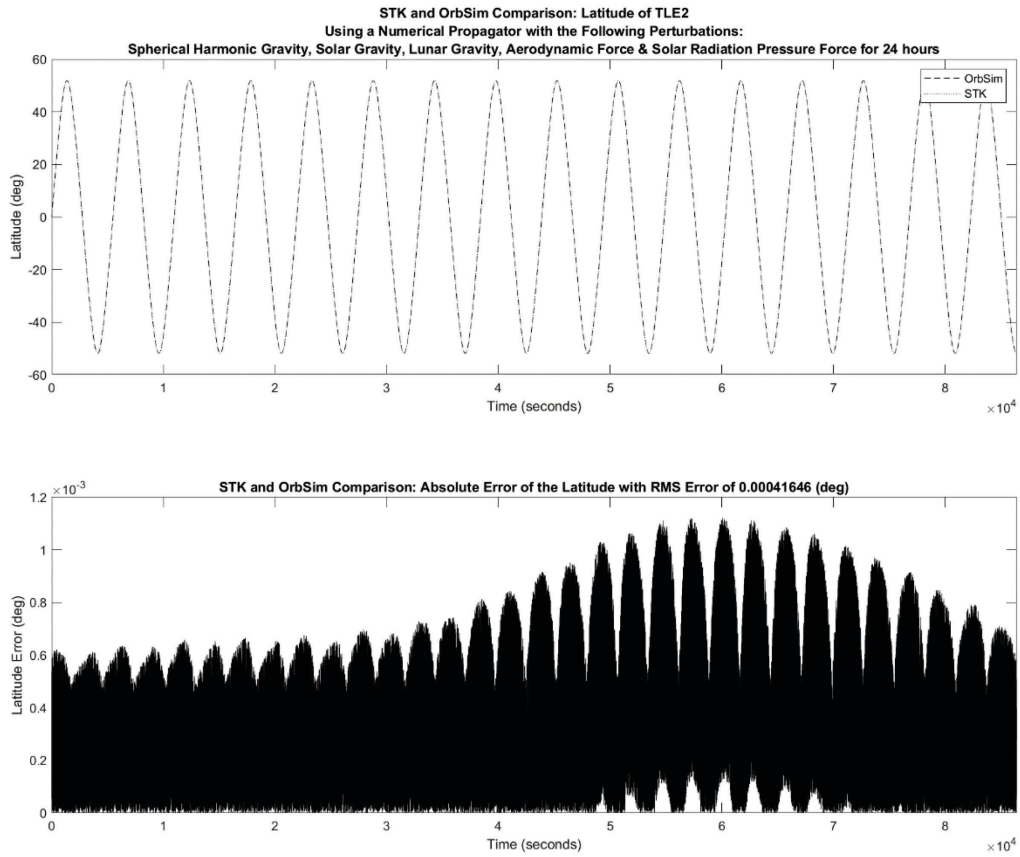


Figure 95: Latitude Comparison of the Satellite from TLE#2 with Spherical Harmonic Gravity, Solar Gravity, Lunar Gravity, Aerodynamic Force and Solar Radiation Pressure

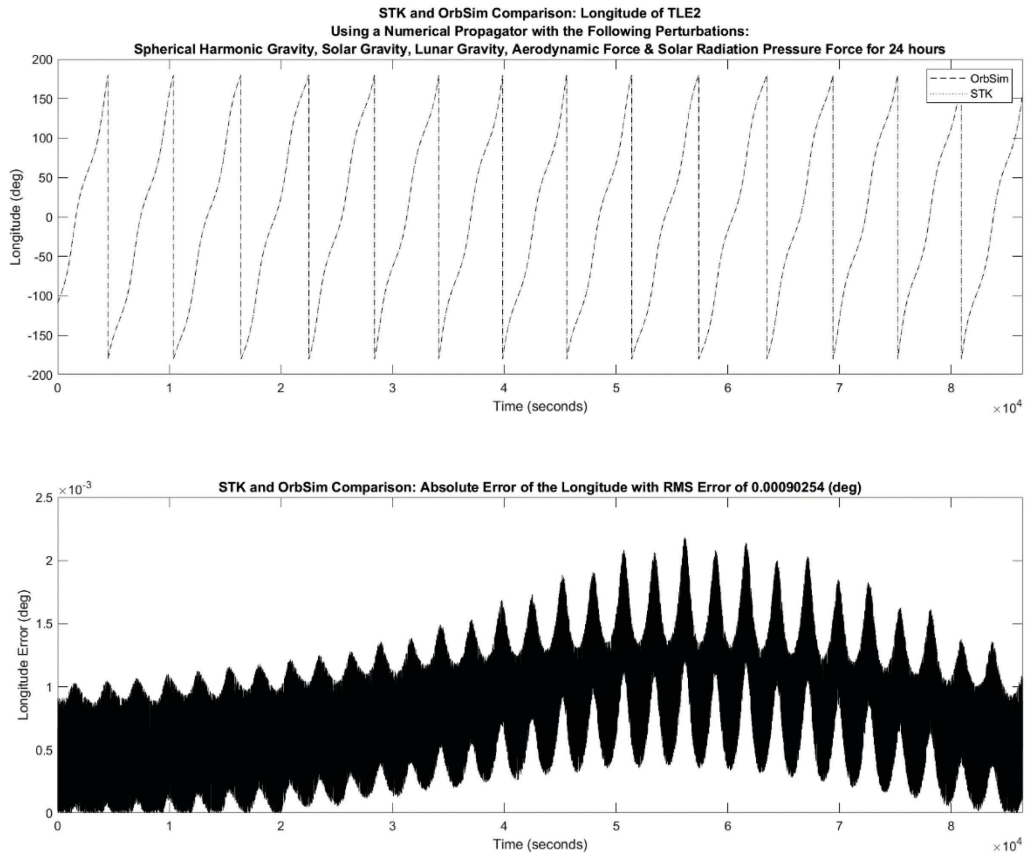


Figure 96: Longitude Comparison of the Satellite from TLE#2 with Spherical Harmonic Gravity, Solar Gravity, Lunar Gravity, Aerodynamic Force and Solar Radiation Pressure

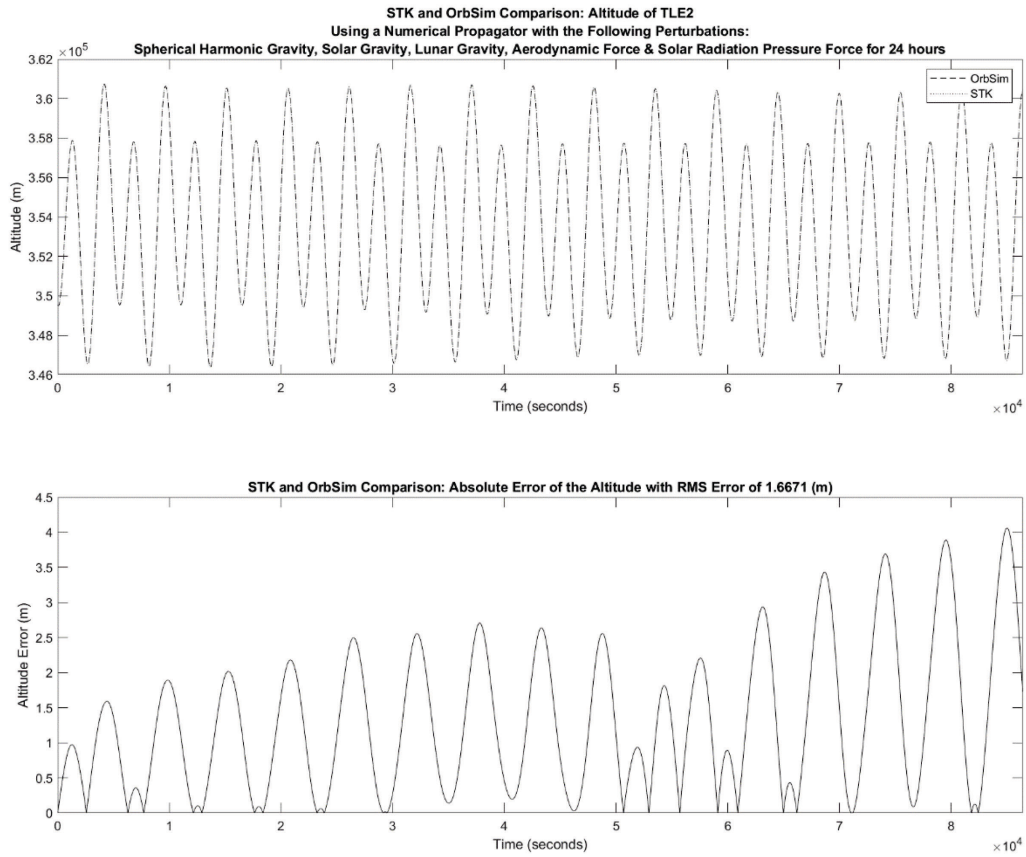


Figure 97: Altitude Comparison of the Satellite from TLE#2 with Spherical Harmonic Gravity, Solar Gravity, Lunar Gravity, Aerodynamic Force and Solar Radiation Pressure